UNIVERSITY OF CALIFORNIA

Santa Barbara

Novel Materials and Fabrication Techniques for Enhanced Current Spreading and Light Extraction in High Efficiency Light-emitting Diodes

A dissertation submitted in partial satisfaction of the

requirements for the degree Doctor of Philosophy

in Materials

by

Asad Jahangir Mughal

Committee in charge:

Professor Steven P. DenBaars, Chair

Professor Shuji Nakamura

Professor James S. Speck

Professor Kaustav Banerjee

December 2017

The dissertation of Asad Jahangir Mughal is approved:

_____

Kaustav Banerjee

_____

Shuji Nakamura

_____

James. S. Speck

_____

Steven P. DenBaars, Committee Chair

December 2017

Novel Materials and Fabrication Techniques for Enhanced Current Spreading and Light Extraction in High Efficiency Light Emitting Diodes

by

Asad Jahangir Mughal

To Mehreen,

for your boundless patience and understanding.

Acknowledgements

My time at UCSB has been filled with many ups and downs, but through it all, I had the privilege to interact with many people both on and off campus who have helped me develop as both a scientist and as an individual. Firstly, I would like to thank Prof. DenBaars for giving me the opportunity to work in his research group and providing me with the freedom to pursue my ideas in well-funded and world-class research facilities. I want to thank Prof. Nakamura for his advice and input through the years and thank Prof. Speck for his emphasis on scientific rigor. I would also like to thank Prof. Banerjee for serving on my committee. The Solid State Lighting Program provided the funding that enabled my research and gave me the honor of collaborating with KACST researcher scientists Drs. Abdulrahman AlBardri. Ahmed AlYamani.

In addition to the advisement by my dissertation committee, I would not have been able to produce the work presented in this thesis without the help and support I received from all the other graduate students, research staff, and administrative staff I have interacted with at UCSB. Two of the first people that I had the pleasure to work with were Sang Ho Oh and Anisa Myzaferi. They taught me the processes and procedures which I used for a significant portion of research such as ZnO growth and LED fabrication. Drs. Jake Richardson and Arthur Reading foreran the ZnO project and helped provide some insight into this material and process. David Hwang and Leah Kuritzky both helped me learn how to use the MOCVD reactors to run my later experiments. Stacia Keller and Mike Iza were essential resources in my efforts at MOCVD growth on free-standing GaN substrates. Joseph Nedy, Erin Kyle, and Dan Cohen provided me advice on how to carry out electrical measurements on my devices. The later portion of my dissertation would not have been possible without the earlier work done by Ben Yonkee and Erin Young. I could only continue their work with the invaluable support of Erin. Once I became a more senior member of the lab I had the privilege to pass on my knowledge to the junior members and interns the group. Benjamin Carberry, Jianfeng Wang, Joonho Back, Koosha Danashi, and Dr. Hongjian Li were among the students I helped with processing and characterization. They in return helped me become a better teacher and mentor.

The facilities for fabricating and characterizing devices and materials could not be possible without the support staff that keeps everything running and provides assistance/advice. The nanofabrication facilities would not function without its staff which includes Brian Thibeault, Don Freeborn, Tony Bosch, Mike Silva, Bill Mitchell, Ning Cao, Tom Reynolds, Aidan Hopkins, and Luis Zuzunaga. The materials characterization and processing facilities in CNSI run due to the efforts of support staff such as Lee Sawyer, Mark Cornish, Tom Mates, Youli Li.

My time at UCSB gave me the opportunity to interact with a wide array of people. Lab and office mates including Changmin Lee, Seunggeun Lee, Charles Forman, Abdullah AlHassan, Burhan Saifadien, Daniel Meyers, Mica Fireman, Andrew Espenlaub, Chris Pynn, and Humberto Foronda provided me a chance to learn and grow through our interactions both in and out of the lab. I was also able to meet fellow graduate students such as Bugra Kaytanli and Arash Pouroshemi with whom I could enjoy engaging conversations and good laughs.

I want to thank the Santa Barbara Judo Club for keeping me sane and active especially Sensei Steve Hoyt, Sensei Vu Nguyen, Andrew Le, Ramzi Deek, Adam Kajdos, Phillip Chan, and Kevin Nguyen. Through our interactions, I fell in love with a sport that teaches you lessons for both on and off the mat.

My time in UCSB gave me the opportunity to pursue topics outside of materials science. Through my classes in the TMP department, I had the honor to be taught by Profs. David Seibold, John Bowers, Gary Hansen, Dave Adornetto, and Robin Campbell. They showed me how to view my work from a different perspective and the process by which valuable ideas can be practically implemented.

I would not be where I am today without the love and support of my family. From an early age, my mother emphasized the importance of getting an education. My late father encouraged my pursuit of the sciences and engineering. My brother Kassim and sister Nadia were always there for me. My late brother Tariq was always proud of me. He left behind the best part of him in his children, my nieces Yasmeen and Alia and nephew Khalid. Finally, I want to thank my wife, Mehreen. This entire endeavor would not have been possible without your love and support.

Asad Mughal

Curriculum Vitae
August 2017

EDUCATION

University of California, Santa Barbara

- Doctor of Philosophy, Materials Science Sep 13 – (Aug 17)
- Ph.D. Advisor: Prof. Steven P. DenBaars
- Ph.D. Committee: Prof. Steven P. DenBaars, Prof. James S. Speck, Prof. Shuji Nakamura, and Prof. Kaustav Banerjee
- Dissertation Topic: Novel Materials and Fabrication Techniques for Enhanced Current Spreading and Light Extraction in High Efficiency Light Emitting Diodes
- Technology Management Program Graduate Program in Management Practice

King Abdullah University of Science and Technology

- Masters of Science, Materials Science & Engineering Aug 10 – May 12

  with Honors
- Masters Advisor: Prof. Sahraoui Chaieb
- Thesis Topic: Synthesis and Characterization of Nano-structured Silicon

Rutgers University

- Bachelor of Science, Materials Science & Engineering Sep 06 – May 10

  with Honors
- Senior Thesis Topic: Solvothermal Acmite Conversion Coatings on Mild Steels

WORK EXPERIENCE

- Graduate Student Researcher Apr 13 – (Aug 17)

  Solid State Lighting and Energy Electronics Center (SSLEEC)
  Materials Department, University of California, Santa Barbara
  Developed processes for the growth, processing, and characterization of next-generation LEDs

- Laboratory Researcher Jun 12 – Jul 13

  Riman Research Group
  Materials Department, Rutgers University
  Oversaw management of the labs, setup/serviced lab equipment, designed/executed experiments, analyzed data

- Undergraduate Research Assistant May 07 – May 10

  Riman Research Group
  Materials Department, Rutgers University
  Synthesized samples, analyzed data, prepared reports and presentations

- Inventory/ Sales Personnel Jun 12 – Jul 13

  Maxter Corporation
  Willingboro, NJ
  Executed sales orders, set up and managed inventory system

TECHNICAL SKILLS

- **Semiconductor Materials Growth** (III-V and II-VI)

  InGaN/GaN LED Metal Organic Chemical Vapor Deposition (MOCVD) and ZnO Hydrothermal Deposition

- **Materials and Device Characterization**

  SEM, TEM, AFM, HRXRD, FTIR, ICP-AES, Raman, Hall Effect, CTLM, photoluminescence, ellipsometry, optical characterization, electrical characterization, and LED analysis

- **Semiconductor Processing and Packaging** (class 100 cleanroom)

  photolithography, e-beam deposition, sputter deposition, ion beam deposition, RIE etching, and ICP etching, polishing/lapping, die singulation, wire bonding, and LED device packaging

- **Device Design**

  mask design (L-Edit), DBR HR/AR design (TFCalc), ray tracing simulations (LightTools), Bandgap simulations (SiLENSe)

TEACHING EXPERIENCE

- Mentor for NNIN Research Experiences for Jun 15 – Aug 15

  Undergraduates (REU) Program
  University of California, Santa Barbara
  Student: Benjamin Carberry, University of Florida

- Teaching Assistant Jan 16 – Mar 16

University of California, Santa Barbara
Course: ECE/MAT 162B – Introduction to Solid State Physics
Instructor: Professor Steven P DenBaars

PUBLICATIONS

- **A.J. Mughal**, E.C. Young1, A.I. AlHassan1, J. Bak2, J.S. Speck, S. Nakamura, and S.P. DenBaars, "Polarization enhanced InGaN/GaN based hybrid tunnel junction contacts to GaN p-n diodes and InGaN LEDs" (submitted to Appl. Phys. Express)
- A. Myzaferi, **A.J. Mughal**, D. A. Cohen, R.M. Farrell, S. Nakamura, J.S. Speck, and S.P. DenBaars, "Zinc Oxide Clad Limited Area Epitaxy Semipolar III-Nitride Laser Diodes," (submitted to Appl. Phys. Lett.)
- H. Li, M. Khoury, B. Bonef, A.I. Alhassan, **A.J. Mughal**, E. Alias, M. Samsudin, P. DeMierry3, S. Nakamura, J.S. Speck1 and S.P. DenBaars, "Semipolar (11-22) 550 nm yellow/green InGaN light-emitting diodes with In0.05Ga0.95N barriers on low defect density (11-22) GaN/sapphire template" (submitted to ACS Appl. Mater. Interfaces)
- M. Khoury, H. Li, L. Kuritzky, **A.J. Mughal**, P. DeMierry, S. Nakamura, J.S. Speck, and S. P. DenBaars, "444 nm InGaN Light Emitting Diodes on Low-defect Density Semipolar (1122) GaN Templates on Patterned Sapphire Substrates", (submitted to Appl. Phys. Lett.)
- H. Wu, K. Blinn, M. Sender, **A. Mughal**, Q. Li, B. Jadidian, and R. Riman, "Using in situ ATR-IR Spectroscopy to Monitor Carbonation of Wollastonite" (submitted to Anal. Chem.)
- D. Hwang, **A. Mughal**, C. D. Pynn, S. Nakamura, and S. P. DenBaars, "Sustained high external quantum efficiency in ultrasmall blue III–nitride micro-LEDs," Appl. Phys. Express 2017 doi:10.7567/apex.10.032101
- **A.J. Mughal**, B. Carberry, J.S. Speck, S. Nakamura, and S.P. DenBaars, "Optoelectronic Properties of Hydrothermal ZnO Thin Films Doped with Ga, Al, and In," Phys. Status Solidi A 2017 doi:10.1002/pssa.201600941
- **A.J. Mughal**, B. Carberry, J.S. Speck, S. Nakamura, and S.P. DenBaars, "Structural and Optical Properties of Group III Doped Hydrothermal ZnO Thin Films," J. Electron. Mat. 2016 doi:10.1007/s11664-016-5235-5
- **A. J. Mughal**, S. Oh, A. Myzaferi, S. Nakamura, J. S. Speck, S. P. DenBaars, "High-power LEDs using Ga-doped ZnO current-spreading layers," Electron. Lett. 2016, 52, 304.

- M. R. Tchalala, J. K. El-Demellawi, **A. J. Mughal**, and S. Chaieb, J. Phys. Conf. Ser. 758, 12018 (2016).
- **A. Mughal**, J. K. El Demellawi, S. Chaieb, "Band-gap engineering by molecular mechanical strain-induced giant tuning of the luminescence in colloidal amorphous porous silicon nanostructures," Phys. Chem. Chem. Phys. 2014, 16, 25273.
- T. Whalen, B. VanSaders, C. Vakifahmetoglu, **A. Mughal**, E. Zlotnikov, S.-B. Cho, R. E. Riman, "Solvothermal Synthesis of Acmite Conversion Coatings on Steel," J. Am. Ceram. Soc. 2013, 96, 3656.

CONFERENCE PRESENTATIONS

- **Asad J. Mughal**, Erin C. Young, Abdullah Alhassan, Joonho Back, James S. Speck, Shuji Nakamura, and Steven P. DenBaars, "Optimization of Hybrid GaN Tunnel Junction Contacts to III-Nitrides," 12th International Conference on Nitride Semiconductors, July 24 to 28, 2017, Strasbourg, France
- **Asad J. Mughal**, Sang Ho Oh, James S. Speck, Shuji Nakamura, and Steven P. DenBaars, "Hydrothermal ZnO Transparent Electrodes for III-Nitride Based LEDs," 2nd Solid State Lighting and Energy Electronics Center Review, Nov. 5, 2016, Santa Barbara, CA, USA
- **Asad J. Mughal**, Benjamin Carberry, James S. Speck, Shuji Nakamura, and Steven P. DenBaars, "Optoelectronic Properties of Group III Doped Hydrothermal ZnO," 58th Electronic Materials Conference, Jun. 22 – 24, 2016, Newark, DE, USA.

PATENTS

- **Asad J. Mughal**, Stacy J. Kowsz, Robert M. Farrell, Benjamin Yonkee, Erin C. Young, Christopher D. Pynn, Tal Margalith, James S. Speck, Shuji Nakamura and Steven P. DenBaars, "III-Nitride Light Emitting Diodes with Tunnel Junctions Wafer Bonded to a Conductive Oxide and having Optically Pumped Layers" (provisional application).
- Erin C. Young, Steven P. DenBaars, James S. Speck, and **Asad J. Mughal**, "Light Emitting Diode with a Tunnel Junction Contact Wafer Bonded to a Conductive Oxide" (provisional application).
- **Asad Mughal**, Sang Ho Oh, and Steven DenBaars, "Multistep Deposition of ZnO on GaN" (US Appln 15/266,990).
- **A. Mughal** and Sahraoui Chaieb, "Colloidal Photoluminescent Amorphous Porous Silicon, Methods of Making Colloidal Photoluminescent

Amorphous Porous Silicon, and Methods of Using Colloidal Photoluminescent Amorphous Porous Silicon" (US 14/396,791).

ACADEMIC HONORS & AWARDS

- Technology Management Program New Venture Competition Finalist — May. 16
- Winning Solver, **Innocentive**

High Precision Shadow Mask for Physical and/or Chemical Vapor Deposition — Sep. 14

Determination of Cu(I) and Cu(II) in Concentrated Chloride Solutions — Sep. 13

Methods for Detecting and/or Removing Air from Moving Fluids — Dec. 12

- KAUST Discovery Fellowship — Aug. 10
- Charles W. Finkl Scholarship — Dec. 09
- KAUST Discovery Scholarship — Jan. 08

HOBBIES AND INTERESTS

- Judo, Brazilian Jujitsu, SCUBA, hiking, and travelling

Abstract

Novel Materials and Fabrication Techniques for Enhanced Current Spreading and Light Extraction in High Efficiency Light Emitting Diodes

by

Asad Jahangir Mughal

Although solid-state lighting based on III-nitride light-emitting diodes (LEDs) is on track to become the dominant technology for lighting our world, we have yet to reach the efficacy limit in these devices. Many challenges remain to be solved to achieve this goal. In this thesis, we discuss novel materials and fabrication techniques which can be used to enhance the efficiency of LEDs through improving lateral current spreading through p-type GaN and increasing light extraction.

Presented in the first part of this thesis is the growth and characterization of hydrothermal ZnO thin films. The effect of growth conditions on the morphology and optoelectronic properties of the films will be discussed. In particular, we studied the effects that group III dopants (Al, Ga, and In) have when introduced into the hydrothermal ZnO thin films. The Ga doped film showed the lowest resistivity, with a resistivity of 1.94 mΩ cm for films doped with 0.4 at.% Ga. Undoped ZnO films showed the lowest optical absorption coefficient of 441 cm^{-1}

at 450 nm. This study represents the first time all three dopants have been systematically compared to one another.

The second part of the thesis focuses on an alternative approach to forming transparent contacts to p-GaN. This involved the regrowth of highly doped n-type GaN using ammonia molecular beam epitaxy (NH_3 MBE) to form epitaxial tunnel junction contact. We discuss several aspects of the growth and performance of regrown TJ contacts on p-n diode structures as well as InGaN/GaN LEDs. Improved turn-on voltages and reduced series resistances have been realized by depositing highly doped Si-doped n-type GaN using MBE on polarization enhanced p-type InGaN contact layers grown using MOCVD. We compared the effects of different Si doping concentrations, and the addition of p-type InGaN on the forward voltages of p-n diodes and LEDs. It was found that increasing Si concentrations from $1.9x10^{20}$ to $4.6x10^{20}$ cm^{-3} and including a highly doped p-type InGaN at the junction both contribute to the narrowing of the depletion width, lowering series resistance from $4.2x10^{-3}$ to $3.4x10^{-3}$ Ω cm^2 and decreasing turn-on voltages of the diodes.

The third, and last part, of this thesis, will focus device results utilizing the alternative current spreading contacts discussed in the previous chapters. LED devices fabricated using doped ZnO films will be analyzed as well as LEDs utilizing MBE n-GaN TJ contacts on blue InGaN flip-chip triangular LEDs grown on both free-standing GaN and patterned sapphire substrates. The performance of

LEDs with Ga-doped ZnO (Ga:ZnO) and Sn-doped In2O3 (ITO) current-spreading layers (CSLs) has been evaluated at high injection current densities. LEDs with electron beam-hydrothermally deposited Ga:ZnO transparent CSLs showed improved performance compared to electron beam deposited ITO at all current densities. External quantum efficiency and wall plug efficiency were both higher for blue emitting LEDs with ZnO. Luminous efficacy increased greatly for the ZnO-based CSL with a peak value of 113 lm/W compared to 82 lm/W for the ITO-based CSL, a 37% improvement. Issues with metal organic chemical vapor deposition (MOCVD), device processing, and device performance are discussed as well.

Content

Chapter 1. Introduction

1.1. Background on Light Emitting Diodes

The discovery and practical implementation of the direct conversion of electrons into photons within a semiconducting material have helped drastically increase the efficacy of illuminating devices. The light-emitting diode (LED) has the potential of benefiting practically every single person on Earth. The health, safety, and living conditions of the world's population will undoubtedly be positively impacted by the continued development and spread of affordable and practical lighting solutions. We have come a long way from the first observations of solid state light emission from a point contact on a silicon carbide crystal by H.J. Round in 1907 [1]. Given the unique property of this alloy system (AlN, GaN, InN) having bandgap energies that span between deep ultraviolet to near-infrared wavelengths, they can be used to create lasers diodes (LD) and LEDs that can emit through the entire visible and UV spectrum [2]. Due to their unique ability to emit light across such a broad spectrum, group III nitrides have been the subject of intense investigation for nearly 40 years [3]. With the discovery of thermally activated Mg-doped p-type GaN in the early 90s, [4] the field of III-N optoelectronics was truly able to flourish. Today, phosphor converted white light from blue (~445 nm) emitting GaN/InGaN based LEDs are on track to eventually

replace inefficient incandescent, fluorescent, and halogen based light sources. However, there are still several challenges left in this field to further the efficiency of these devices. The ones that are considered in this dissertation are that of the current spreading electrodes and device design.

With the demonstration of the first GaN-based blue (LEDs [5] and LDs [6] by Nakamura et al., group III nitride based optoelectronics have rapidly been developed and commercialized for industries such as lighting and power electronics. The technology has advanced to the point where current commercially available LED white light bulbs have luminous efficacies exceeding 200 lm/W [7]. Although considerable progress has been made, there still exist significant challenges in the field. For one, LEDs for white lighting typically operate at low current densities (< 50 A/cm^2) to attain maximum external quantum efficiencies (EQE), wall plug efficiencies (WPE), and luminous efficacies. This is because internal quantum efficiency "droops" under increasing injection currents, which is caused by phenomena such as the generation of auger electrons [8] and ohmic heating [9]. Also, voltage drops at the contacts to the n and p side of the device lead to increased operating voltages, lowering WPE. These factors lead to low light output per devices necessitating the need for several LEDs per packaged lighting product, increasing costs. As LEDs continue to replace once conventional light sources, the need for them to reach higher efficiencies and luminous fluxes continue to grow [10]. To achieve this, new materials, compositions, and designs are

required to overcome current performance limitations. Finding ways to improve the performance of LEDs and LDs is essential for the continuing development of group III nitride-based optoelectronics.

Basic Structure of a LED

Essentially, InGaN/GaN LEDs comprise of about nine layers of materials stacked on top on one another. The first of these are the substrates, which can be either the same materials, GaN, or a different material with a crystal lattice that can accommodate the growth of GaN, such as Al_2O_3 of SiC [11]. GaN has a hexagonal wurtzite crystal structure; it exhibits polarization induced effects along its asymmetric c-axis. (0001) c-plane Al_2O_3 is the most common substrate used. As shown in the schematic in **Figure 1.1**, the first epitaxial layer consists of an electron-rich n-type semiconductor such as Si-doped GaN. Next, multiple alternating thin stacks (few unit cells thick) of GaN and InGaN are grown to form a superlattice. This layer is used to help reduce the built-in potential in the active region as well as improve current spreading and crystal quality. After this layer, a buffer layer of lightly Si-doped GaN is grown before the start of the active region. The active region is typically composed of InGaN/GaN, which are on the order of 1-20 nm in thickness. Due to the difference in bandgaps, the interface between

these layers, heterojunctions forms allowing electrons and holes to be spatially confined in quantum wells.

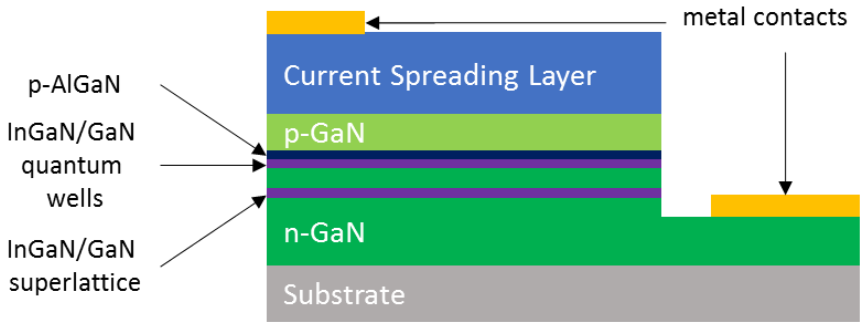

Figure 1.1 Simple Schematic of the epitaxial layers in a standard InGaN/GaN LED

As displayed in **Figure 1.2**a, current is injected into the device under some forward bias carriers to recombine and generate light consisting of wavelengths smaller than the bandgap of the smaller bandgap material (i.e., InGaN) through the process of spontaneous emission. This region in the device is also known as the active layer. Above this is the source of holes, typically p-type GaN doped with Mg [10]. A p-AlGaN layer is grown just after the quantum wells to block electrons which have enough energy to overshoot the quantum wells. Since p-GaN is highly resistive, a transparent conductor, typically Sn-doped In_2O_3 (ITO), is used to spread current across it while allowing light to be emitted from the top surface. Metal contacts are deposited on both the current spreading layer and the n-GaN. Access to the n-doped layer is made through etching into the device.

As stated earlier, conventional InGaN/GaN LEDs are grown with the crystal oriented along the c-axis. However, the c-axis in III-N materials is asymmetric which results in built-in polarization and produces large internal electric fields that result in decreased efficiencies due to the quantum-confined Stark effect. As seen in **Figure 1.2**b, polarization related internal electric fields cause spatial separation between electrons and holes which results in a reduction of recombination efficiency [12]. One solution to this issue is to grow the III-N materials in a semi-polar or non-polar crystal orientation. Non-polar m-plane and semipolar orientations are harder to grow on but are promising planes for increasing internal quantum efficiency [13]. It has been shown that non-polar m-plane and a-plane [14] orientations provided a significant reduction in polarization effects and enhanced internal quantum efficiency. Blue to green wavelengths (430-530 nm) can be achieved by varying the In concentration in the InGaN alloy.

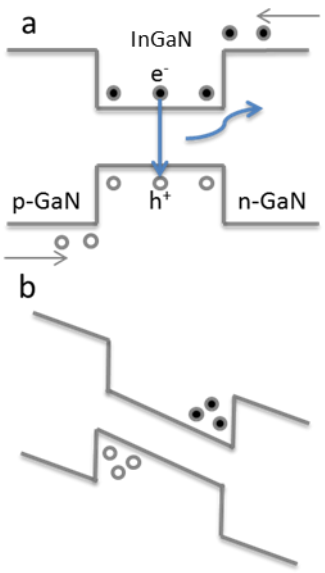

Figure 1.2 a) radiative carrier recombination in an InGaN well b) separation of carriers due to the quantum-confined Stark effect

LED Performance Metrics

The total efficacy of a LED is a product of the efficiency of various processes within the material and the device. The electrons that are injected into the LED must radiatively recombine to form photons, and these photons must escape from the die for it to be useful light. Along the way, both electrons and photons are lost through non-radiative pathways or absorbance, respectively. The ratio between radiative recombination and total carrier recombination is known as internal quantum efficiency (IQE or η_{iq}), while the ratio of optical power out of the device to the optical power generated within is known as light extraction efficiency (LEE

or η_{le}). The fraction of electrons that are injected into the device and either recombine radiatively or non-radiatively is known as the injection efficiency (η_{inj}). It is usually considered unity since few pathways block electrons from entering the semiconductor.

Internal quantum efficiency, η_{iq}, can also be described as the ratio between the rate of photons emitted from the active region to the rate of electrons injected into it. This is shown in equation (**1.1**) where φ_i is the optical power out of the active region, h is Planks constant, c is the speed of light, λ_{avg} is the emission wavelength, I is the current, and q is the charge of the electron.

$$\eta_{iq} = \frac{photon\ emission\ rate\ from\ active\ region}{electron\ injection\ rate} = \frac{\phi_i \lambda_{avg}/hc}{I/q} \tag{1.1}$$

Another way to express IQE is in terms of carrier density (n) using the well-known ABC model shown in equation (1.2).

$$\eta_{iq} = \frac{Bn^2}{An + Bn^2 + Cn^3} \tag{1.2}$$

In this model, non-radiative recombination rate due to carrier recombining in defect/trap states (Shockley-Reed-Hall recombination) is expressed as An. Bimolecular recombination, i.e., radiative recombination, the rate is shown as Bn^2. Auger recombination rate being expressed as Cn^3. A, B, and C are the respective coefficients for each process. This model is commonly used to help explain the phenomenon of efficiency droop in LEDs. From this expression, it can be shown

that increasing the carrier density in the active region by increasing the applied current into an LED increases the effects of non-radiative Auger recombination. Also, a further loss in efficiency can occur at high current densities due to ohmic heating.

Once the light is generated in the active region, it must escape the GaN/Al_2O_3 crystal. Light extraction efficiency (LEE or η_{le}) is the ratio with rate of photons emission out of the device to the rate of photon generation in the active region, as shown in equation (1.3), where φ_r is the optical power out of the device.

$$\eta_{le} = \frac{rate\ of\ photons\ emitted\ out\ of\ crystal}{rate\ of\ photons\ generated\ in\ crystal} = \frac{\phi_i/h\nu}{\phi_r/h\nu} \tag{1.3}$$

Due to the high contrast in refractive indexes between GaN (n~2.4 @440 nm), Al_2O_3 (n~1.7 @440 nm), and air (n=1), the angle for total internal reflection given by Snell's law is quite small (~24° for GaN to air). In addition, Fresnel reflections are also considered under these conditions. Designing devices with high light extraction efficiencies is challenging, especially on free-standing GaN substrates.

Since it is hard to measure both LEE and IQE directly, the most commonly quoted efficiency metric for LEDs is external quantum efficiency (EQE or η_{eq}). It is simply the product of LEE and IQE and represents the ratio between the rate of photons emitted out of the LED to the rate of electrons injected into the LED, see equation (1.4) [15].

$$\eta_{eq} = \frac{rate\ of\ photons\ out}{rate\ of\ electrons\ in} = \eta_{le}\eta_{iq} = \frac{\phi_i/h\nu}{I/q} \tag{1.4}$$

It is a much simpler value to measure since we only need to know the optical power out of the device and the input current and provides a useful metric for light generation for a given device. However, since this expression does not consider operating voltage, it does not provide a full picture of a LED's performance.

When discussing the total efficiency of monochromatic light generated from a LED, another important metric is referred to as the power conversion efficiency or wall-plug efficiency (WPE or η_{wp}). It is simply the ratio of optical power out of the device (φ_r) and the electrical power (P) into the device, shown in (1.5) [16].

$$\eta_{wp} = \frac{optical\ power\ out}{electrical\ power\ in} = \frac{\phi_r}{P} = \frac{\phi_r}{IV} = \frac{\eta_{eq}hc}{V\lambda_{avg}q} \tag{1.5}$$

If the monochromatic light is converted to white light, such as when a blue emitting LED and a yellow emitting phosphor is used, then metrics such as color rendering index (CRI), and luminous efficacy (lm/W) are considered. **Figure 1.3** illustrates the sources of loss in a LED with the input being electrons into the device and the output being either heat or photons out into free space.

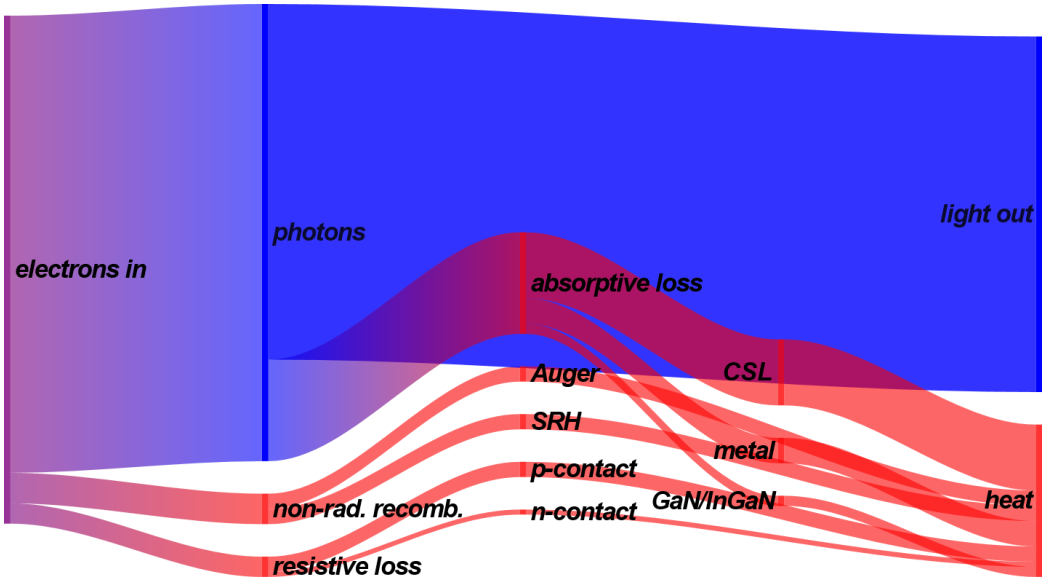

Figure 1.3 Sankey diagram illustrating the efficiency of light emitting diodes

1.2. Motivation for Transparent Current Spreading Layers

Due to its high resistivity (1-2 Ω cm), Mg-doped p-GaN requires a conductive contact layer between it and the p-side contacts in order mitigate current crowding near the metal contacts and allow carriers to be uniformly injected into the active region across the device [17]. Originally, very thin semi-transparent Ni/Au films were deposited due to the ability of Ni to make ohmic contact to p-GaN and its low sheet resistivity [18]. However, in addition to a low resistivity, this layer also requires low optical absorbance to increase extraction efficiency, making thin Ni/Au films not ideal.

Transparent conductive oxides (TCOs) are now typically used for this application since they exhibit both high optical transparency and high electrical

conductivity. Sn-doped In_2O_3 (ITO) is a commonly used TCO for this purpose given its low electrical resistivity [19] and lower light absorption. For the TCO to be an effective CSL, it must be able to transfer current away from the metal contact layer laterally.

Tunnel Junction Contacts

Since there are no practical p-type transparent conductors, the most common way to inject carriers into p-GaN is through forming tunnel junctions with a wide bandgap n-type semiconductor. It has been shown that heavily doped p-n junctions enable carriers to undergo interband transfer [20]. In the case of p-GaN, we need holes to be injected through this junction. This can occur when a p-n junction is placed under reverse bias as is the case when a LED is positioned under forward bias, as illustrated in **Figure 1.4**. If the dopant concentrations in both the n and p side of the junction are sufficient, interband tunneling can occur, allowing holes to be injected from the conduction band of the n-GaN into the valence band of the p-GaN. From there the holes travel to the quantum well layer where they can radiatively recombine with an electron.

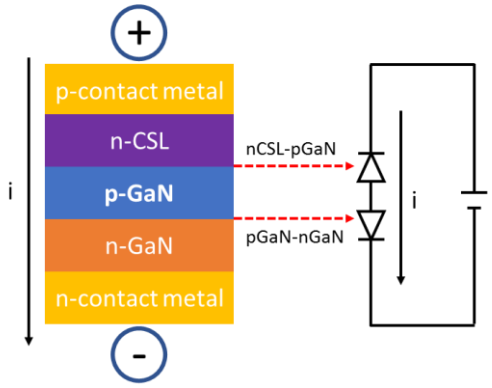

Figure 1.4 Schematic of an LED with an n-type CSL p-contact with its equivalent circuit on the right

As displayed in **Figure 1.5**, this reverse bias displaces the conduction band of the n side and the valence band of the p side such that they overlap and enable quantum tunneling of electrons through the barrier defined by the depletion width.

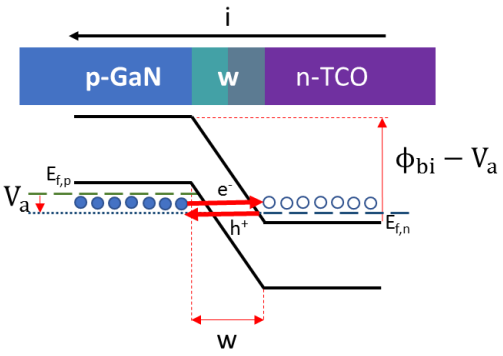

Figure 1.5 Schematic of an n-CSL and p-GaN TJ contact (top) and a simplified band diagram illustrating tunneling (bottom)

The depletion width of a p-n junction is defined by equation (1.6) [21],

$$w = \sqrt{\frac{2\varepsilon}{q}\left(\frac{1}{N_A}+\frac{1}{N_D}\right)(V_{bi}-V)} \tag{1.6}$$

where ε is the permittivity of the semiconductor, q is the charge of an electron, N_A is the acceptor concentration, N_D is the donor concentration, V is the applied voltage, and V_{bi} is the built-in potential defined by equation (1.7). It is important to note that when the junction is placed under reverse bias, the depletion width increases due to the accumulation of charge carriers near the interface. This increase in depletion width hinders tunneling. Thus, having higher donor and acceptor concentration is essential for narrowing the depletion width and decreasing the voltage penalty of these types of junctions.

$$V_{bi} = \frac{kT}{q} ln\left(\frac{N_D N_A}{n_i^2}\right) \tag{1.7}$$

The built-in potential of the junction can be expressed as a function of Boltzmann's constant k, temperature T, intrinsic carrier concentration n_i, as well as both N_A and N_D. Lowering V_{bi} is another approach to lowering the depletion width. One way to do so is by increasing n_i, which can be accomplished by selecting materials with lower bandgaps E_g, see equation **Error! Reference source not found.**.

$$n_i = \sqrt{N_C N_V}\, e^{-\frac{E_g}{2kT}} \tag{1.8}$$

Transparent Conductive Oxides

Since the earliest known report of a CdO based transparent conducting oxide by Bädeker in 1907 [22], materials that are both optically transparent and electrically conductive have served a role in many optoelectronic applications. In general, TCOs are alloyed or doped intrinsically insulating metal oxides that exhibit sheet resistances on the order of 10 Ω/□, absorption coefficients less than 10^4 cm^{-1} at wavelengths between 300 to 900 nm, and resistivities in the range of 10^{-3} to 10^{-4} Ω cm. Therefore, suitable oxide materials should have carrier concentrations on the order of 10^{18} cm^{-3} or greater and band gap energies above 3 eV [23]. Electric current in TCOs is transported by electrons introduced into the conduction band, and the conduction band must constitute an extended state so that doped electrons can migrate in the lattice under a weak applied electric field. Most conductive oxides are composed of binary or ternary compounds, containing either one or two metallic elements. Electron doping in oxide crystals is achieved using techniques such as substitution of cations or anions or by the introduction of oxygen vacancies/excess cations. At least one of the techniques must prove effective in the selected host material [24]. With a few exceptions, the majority of known TCOs

are composed of alloys found in phase systems consisting of either ZnO - In_3O_2 - Al_2O_3 - Ga_2O_3 or In_3O_2 - SnO_2 - ZnO, see **Figure 1.6**.

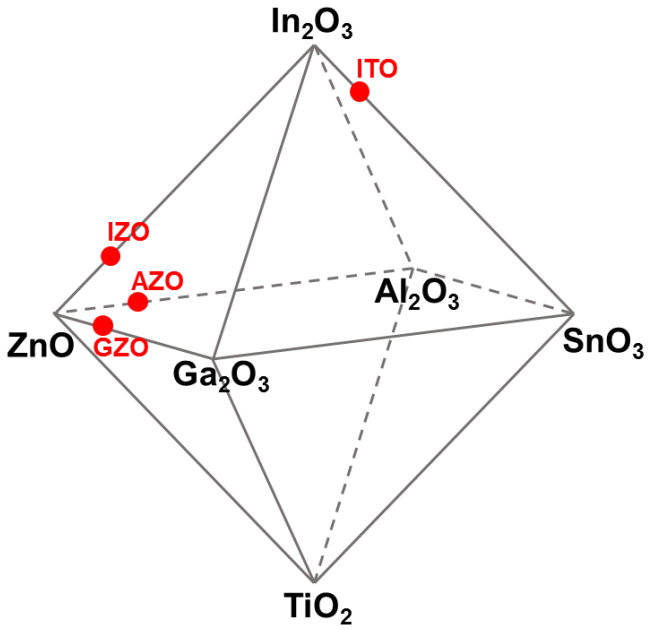

Figure 1.6. Phase space for common TCO materials

Of these systems, Al-doped ZnO, Sb-doped In_3O_2, and F doped SnO_2 are the most well-studied host compounds capable of being doped or alloyed to induce TCO behavior [25]. Also, a more recently discovered TCO system is Nb/Ta-doped TiO_2 [26]. **Table 1** summarizes the properties of several TCOs found in the literature with a focus on mainly ZnO based materials.

Table 1 Review of TCO materials, the substrate used, growth technique, and their respective properties

Material	Substrate	R_{SH}	ρ	n	μ	Growth	Ref

		Ω/□	10^{-4} Ω cm	10^{20} cm^{-3}	cm^2 $V^{-1}s^{-1}$	Method	
Sb:In_2O_3	**Glass**	**45**		**4.3**	**35**	**Sputter**	[27]
Mo:In_2O_3	Glass	5.0	1.80	2.50	50.0	PLD	[28]
Sb:In_2O_3	GaN	18.09	3.98	25.4	6.13	E-Beam	[29]
SnO_2	Glass	16.7		5.00	15.0	Sputter	[30]
Ga: ZnO	GaN	16.54	3.64	5.43	14.9	MOCVD	[29]
Ga: ZnO	GaN		3.80	3.40	48.0	MBE	[31]
Ga: ZnO	Glass	3300		0.56	3.40	Sol Gel	[32]
H:ZnO	Si		2.00	6.00	38.9	Sputter	[33]
Ga:ZnO	Glass			8.38	27.9	Hydro	[34]
Ga:ZnO	Al_2O_3			10.6	38.9	Hydro	[34]
Ga:ZnO	$MgAl_2O_3$			3.10	28.0	Hydro	[35]
Ga:ZnO	GaN			5.43		Hydro	[29]
Ga:ZnO	GaN			4.70	14	Hydro	[31]
Cd:SnO_2	Glass	7.2		3.20	54.0	Sputter	[30]
Si:ZnO	Glass	10	3.80	10		Sputter	[36]
Al:ZnO	Glass		0.85	15.1	47.6	PLD	[37]
Ga:ZnO	Quartz		0.81	146	31.0	PLD	[38]
Al:ZnO	Al_2O_3	15	2.2	8.8	32	PLD	[39]
Ga:ZnO	GaAs					ALD	[40]
Ga:ZnO	p-GaN		3.4	150	11.3	ALD	[41]
In,Ga:ZnO	Spinel		7.4	3.14	41.9	Hydro	[42]
Ga:ZnO	Spinel		10.4	2.27	26.9	Hydro	[42]
ZnO	GaN			0.031	10.3	Hydro	[43]
Mg/Ga:ZnO	Glass		6.89	5.23	9.91	Sputter	[44]
ZnO	**Gan**	**15**		**0.23**	**71**	**Hydro**	[45]

Indium Tin Oxide

In III-Nitrides optoelectronics, an alloy of 10% SnO_2 and 90% In_2O_3 (ITO) is the TCO of choice for current spreading applications. Since its demonstration on

GaN LEDs [46], ITO has replaced thin metal current spreading electrodes in LEDs and become the industry standard. This is due to its low resistivity and good contact resistance to p-GaN [47], improved optical absorbance over thin Ni/Au, and ease of deposition using an electron beam and sputtering techniques.

Zinc Oxide

Due to its relatively high optical absorbance [48], ITO films for LED applications are typically deposited at thicknesses less than 300 nm to mitigate the absorption of light generated by the device [49]. An alternative TCO which has a relatively low absorbance in the visible range [50] and good electrical conductivity [51] is zinc oxide. Hydrothermally deposited ZnO transparent CSLs have been shown to outperform both Ni/Au [52] and ITO [45] in LED applications. In addition, group III elements such as Al, Ga, and In have been shown to be effective n-type dopants in ZnO [53], allowing for further optimization of the film. Figure 1.7 shows simulated n-ZnO to p-GaN junctions at 0 and -0.5 V bias, illustrating that under a reverse bias the band offset is such that interband tunneling is possible. Table 2 compares the properties of hydrothermal ZnO and e-beam ITO. It shows that although resistivity for ZnO is higher, the lower absorption coefficient allows for thicker films and thus lower sheet resistances.

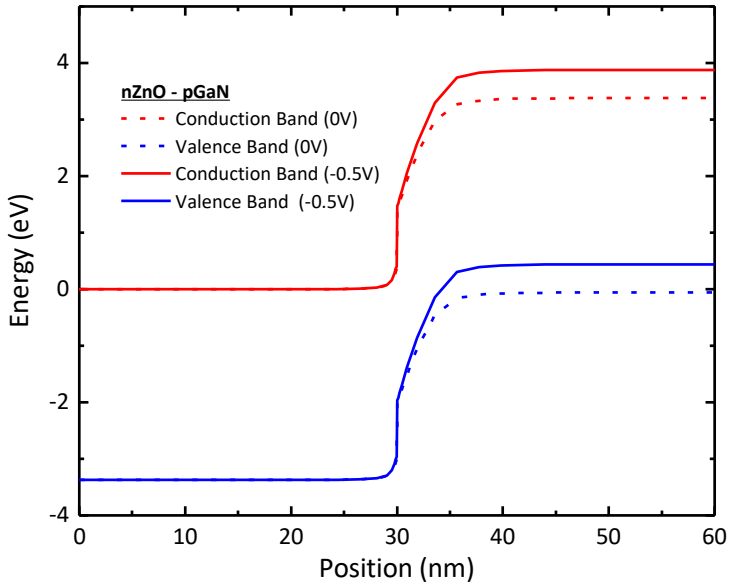

Figure 1.7 p-n junction band diagrams generated using SiLense modeling software dashed lines are under no bias $n_{ZnO}= 10^{19}$ cm^{-3} $p_{GaN}= 2(10)^{18}$ cm^{-3} and solid lines are under a 0.5 V reverse bias

Table 2 Comparison between optoelectronic properties of ITO and ZnO

CSL	t (μm)	ρ_c (Ω cm^2)	α (cm^{-1})	R_{sh} ($\Omega/\square$)	ρ (Ω cm)
ITO	0.2	0.0032	2000	23	4.53×10^{-4}
ZnO	2.0	0.0022	100	11	2.64×10^{-3}

Gallium Nitride

Another material which may be used to spread current across p-GaN is highly doped n-GaN. In the past few years it has garnered increasing interest due to the

possibility of expanding the design space for LED devices to include buried contacts and multijunction designs [54]. **Figure 1.8**(a) shows a simulated band structure of a p-n GaN homojunction including the direction of electron flow under reverse bias. **Figure 1.8**(b) displays a schematic of the junction including the depletion region that is formed when the junction is formed. This method of forming a CSL has been demonstrated for LEDs, edge emitting LDs, and vertical cavity surface emitting laser diodes (VCSELs). Currently, the regrowth of n-GaN on p-GaN is carried out due to Mg passivation when grown in metal organic chemical vapor deposition (MOCVD) systems. Molecular beam epitaxy (MBE) is used to regrow high-quality n-GaN on top of p-GaN. However, efforts are underway to find an alternative deposition method.

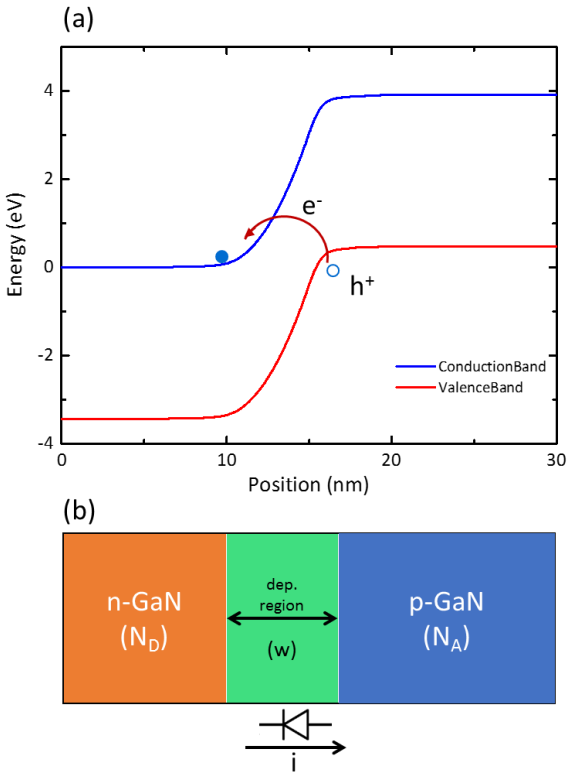

Figure 1.8 (a) simulated band diagram of a p-n GaN tunnel junction under a 0.5 V reverse bias (b) schematic of the junction along with direction of current flow

1.3. Transparent Current Spreading Layer Performance Metrics

It is important to know which metrics must be evaluated when comparing different CSLs to one another. One way to view them is through a parameter known as the current spreading length. Current spreading length, Ls, can be defined as the distance past a metal contact where the current density drops by 1/e (~37%) of its value at the metal contact [55]. It is described by equation (1.9) and illustrated in **Figure 1.9**.

$$L_S = \sqrt{\frac{n_i kT}{eJ_0}\frac{1}{R_{SH}}} \tag{1.9}$$

Where n_i is the diode ideality factor, k is the Boltzmann constant, T is temperature, e is the charge of an electron, J_0 is the current density at the metal contact, and R_{SH} is sheet resistance.

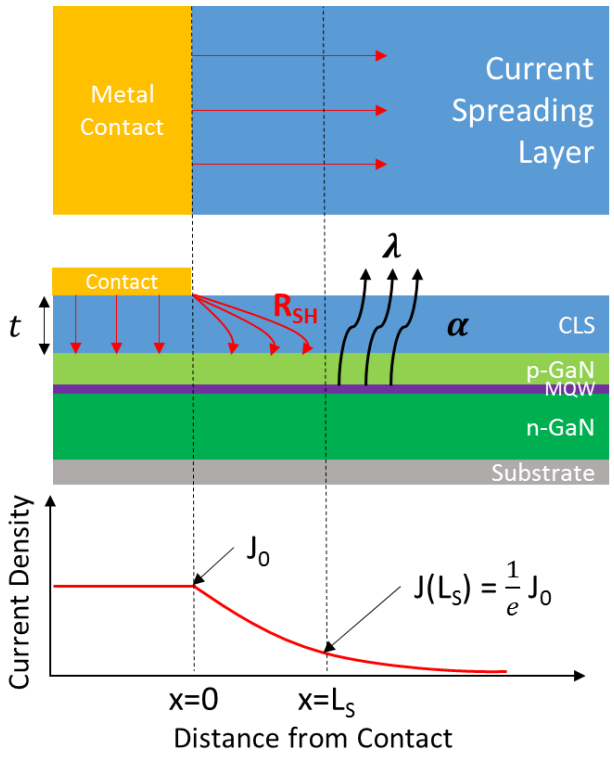

Figure 1.9 Schematic illustrating the function of the CSL on InGaN GaN LEDs

To achieve high current spreading length, the CSL must have a low sheet resistance values. Since sheet resistance is the ratio between resistivity and thickness, it can be accomplished by either decreasing resistivity or increasing thickness. The Comsol simulation presented in Figure 1.10 shows the effect that

lowering sheet resistance of the CSL has on the spreading of current across a device. When going between a sheet resistance similar to the p-GaN layer to that of the n-GaN, we can observe a substantial improvement in current spreading.

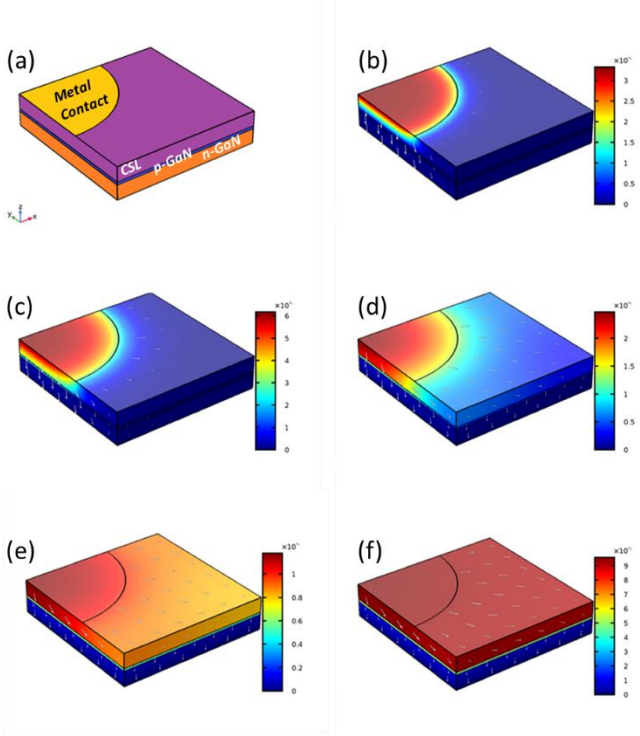

Figure 1.10 Comsol simulations of current spreading across a thin film resistor (a) test structure used for simulation (b) CSL R_{sh} 1000 Ω/sq (c) CSL R_{sh} 100 Ω/sq (d) CSL R_{sh} 10 Ω/sq (e) CSL R_{sh} 1 Ω/sq (f) CSL R_{sh} 0.1 Ω/sq

In addition, having low optical absorption is crucial for improving light extraction efficiencies in LEDs. Another metric to compare current spreading layers is to use a figure of merit (FOM) using a ratio of appropriate metrics. One commonly used figure of merit is shown in equation (1.10).

$$TCO_{FOM} = \frac{\sigma}{\alpha} = -\frac{1}{R_{SH} ln(T + R)} \quad (1.10)$$

Where T and R represent transmittance and reflectance respectively. It is simply the ratio between the films conductivity, σ (S/cm), and its absorption coefficient, α (cm^{-1}) [56].

Table 3 compares figure of merits for several common TCO CSLs [57].

Table 3 Figure of merit for several TCO materials with their respective sheet resistances and absorption coefficients [57]

TCO	Dopant	R_{SH} (Ω/□)	α (cm^{-1})	FOM ($Ω^{-1}$)
ZnO	F	5.0	0.03	7.0
SnO_2	CdO	7.2	0.02	7.0
ZnO	Al	3.8	0.05	5.0
In_2O_3	Sn	6.0	0.04	4.0
SnO_2	F	8.0	0.04	3.0
ZnO	Ga	3.0	0.12	3.0
ZnO	B	8.0	0.06	2.0
SnO_2	Sb	20.0	0.12	0.4
ZnO	In	20.0	0.20	0.2

1.4. Deposition of Current Spreading Layers

Physical Vapor Deposition

Several techniques currently exist for depositing thin films of TCOs [58]. The most common approach found in the literature is by physical vapor deposition (PVD), through a sputtering mechanism such as RF reactive sputtering [59], RF magnetron sputtering [33], electron cyclotron resonance (ECR) sputtering [60], e-

beam evaporation [61], pulsed laser deposition (PLD) [37], or MBE [31]. These techniques all require solid source materials with the required composition that are bombarded by some particle to form a vapor which deposits on a substrate. The quality of these kinds of films is highly dependent on parameters such as deposition rate, substrate temperature, and source material.

Chemical Vapor Deposition

Chemical vapor deposition (CVD) techniques are also widely used to deposit TCO films. These methods form films through chemical reactions on the substrate surface. For example, ZnO can be deposited using MOCVD using diethylzinc as a precursor [62]. Molecular beam epitaxy has been utilized to grow doped ZnO transparent electrodes using elemental Zn as a precursor [63]. Although these methods can produce high-quality thin films, they come at a high cost due to expensive precursors and slow deposition rates. Aerosol spray pyrolysis is commonly used to deposit TCO materials onto a substrate through a process in which a precursor solution is atomized to form droplets which are then carried by a flowing gas through a heated reactor. Once the droplets enter the reactor, the solvent evaporates and the solutes undergo thermal pyrolysis to form a film [30]. Due to the fast kinetics of this process, the film quality is typically not as good as other methods.

Another CVD technique that is fast gaining popularity for the growth of a broad range of thin films is atomic layer deposition (ALD) [64]. As the name implies, ALD works by depositing monolayers of material at a time through cycling precursor gases into a reaction chamber. For ZnO films this is typically zinc acetate and water with dopants such as Ga or Al provided by metalorganic sources. This technique is like that of MOCVD except for the cycling of the precursors into the chamber. Precise control over film quality can be achieved, but at the cost of slow deposition rates.

Hydrothermal Deposition

Hydrothermal deposition involves the use of aqueous solutions under elevated temperatures and pressures to crystallize films on a given substrate. Like any solution based crystal growth method, the driving force behind crystallization is the formation of a supersaturated solution. This is accomplished by modulating either temperature, pH, or both. Using this deposition method to form transparent current spreading layers is not as common as the PVD and CVD methods discussed earlier. However, this technique is quite advantageous because it only requires simple equipment and basic chemistry to form films. Additional discussions on hydrothermal growth will be provided in subsequent chapters.

1.5. Synopsis of the Dissertation

This dissertation examines the role TCOs as well as MBE grown n-GaN CSLs have on the performance of InGaN/GaN-based LEDs. Also, novel LED device designs are evaluated with these current spreading layers.

In the second chapter of this thesis, the growth of hydrothermal ZnO thin films is presented. The effect of growth conditions on the morphology and crystal structure of the films will be discussed. In particular, we studied the effects that group III dopants (Al, Ga, and In) have when introduced into the hydrothermal ZnO thin films. The third chapter discusses the optoelectronic properties of doped hydrothermal ZnO thin films.

Chapter four focuses on an alternative approach to forming transparent contacts to p-GaN. This involved the regrowth of highly doped n-type GaN using ammonia molecular beam epitaxy (NH_3 MBE) to form epitaxial tunnel junction (TJ) contact. We discuss several aspects of the growth and performance of regrown TJ contacts on p-n diode structures as well as InGaN/GaN LEDs. Preliminary work on sputtered n-GaN TJ contacts is also presented.

Finally, chapter five of this thesis will focus on processed LED devices. Devices fabricated using doped ZnO films will be analyzed and compared to devices with ITO contacts. Preliminary work utilizing MBE n-GaN TJ contacts on blue InGaN flip-chip triangular LEDs grown on free-standing GaN substrates using MOCVD will be presented as well. Device fabrication and performance will be

discussed and will be followed by concluding remarks and recommendations on future work.

1.6. References

[1] H. J. Round, Electr. World **49**, 309 (1907).

[2] O. Ambacher, J. Phys. D. Appl. Phys. **31**, 2653 (1998).

[3] R. Dingle, D. D. Sell, S. E. Stokowski, and M. Ilegems, Phys. Rev. B **4**, 1211 (1971).

[4] S. Nakamura, T. Mukai, M. Senoh, and N. Iwasa, Jpn. J. Appl. Phys. **31**, L139 (1992).

[5] S. Nakamura, T. Mukai, and M. Senoh, Appl. Phys. Lett. **64**, 1687 (1994).

[6] S. Nakamura, M. Senoh, S. ichi Nagahama, N. Iwasa, T. Yamada, T. Matsushita, H. Kiyoku, and Y. Sugimoto, Japanese J. Appl. Physics, Part 2 Lett. **35**, L74 (1996).

[7] Y. Narukawa, M. Ichikawa, D. Sanga, M. Sano, and T. Mukai, J. Phys. D. Appl. Phys. **43**, 354002 (2010).

[8] J. Iveland, L. Martinelli, J. Peretti, J. S. Speck, and C. Weisbuch, Phys. Rev. Lett. **110**, 177406 (2013).

[9] Seoung-Hwan Park and Yong-Tae Moon, IEEE Photonics J. **6**, 1 (2014).

[10] S. Pimputkar, J. S. Speck, S. DenBaars, and S. Nakamura, Nat. Photonics **3**, 2 (2009).

[11] R. Quay, *Gallium Nitride Electronics*, 1st ed. (Springer Berlin Heidelberg, Berlin, Heidelberg, 2008).

[12] J. Ryou, P. Yoder, and J. Liu, … Top. Quantum … **15**, 1080 (2009).

[13] A. E. Romanov, T. J. Baker, S. Nakamura, and J. S. Speck, J. Appl. Phys. **100**, (2006).

[14] P. Waltereit, O. Brandt, a Trampert, H. Grahn, J. Menniger, M. Ramsteiner,

M. Reiche, and K. Ploog, Nature **406**, 865 (2000).

[15] E. F. Schubert, T. Gessmann, and J. K. Kim, in *Kirk-Othmer Encycl. Chem. Technol.* (John Wiley & Sons, 2005), pp. 1–31.

[16] E. F. Schubert, *Light Emitting Diodes*, 2nd ed. (Cambridge University Press, Cambridge, 2006).

[17] J. Chen, G. Sheu, F. Hwu, H. Chen, and J. Sheu, Opt. Rev. **16**, 213 (2009).

[18] C. H. Lin, D. L. Hibbard, a. Au, H. P. Lee, Z. J. Dong, F. J. Szalkowski, J. Chen, and C. Chen, MRS Proc. **639**, 2 (2000).

[19] A. Suzuki, T. Matsushita, T. Aoki, Y. Yoneyama, and M. Okuda, Jpn. J. Appl. Phys. **40**, L401 (2001).

[20] L. Esaki, Phys. Rev. **109**, 603 (1958).

[21] S. Sze and K. Ng, *Physics of Semiconductor Devices*, 3rd ed. (John Wiley & Sons, 2006).

[22] K. Bädeker, Ann. Phys. **327**, 749 (1907).

[23] T. Minami, Semicond. Sci. Technol. **20**, S35 (2005).

[24] H. Kawazoe and K. Ueda, J. Am. Ceram. Soc. **36**, 3330 (1999).

[25] D. R. Kammler, D. D. Edwards, B. J. Ingram, T. O. Mason, G. B. Palmert, A. Ambrosini, and K. R. Poeppelmeier, in *Photovoltaics 21st Century*, edited by V. K. Kapur (The Electrochemical Society, 1999), pp. 68–75.

[26] T. Hitosugi, N. Yamada, S. Nakao, Y. Hirose, and T. Hasegawa, Phys. Status Solidi **207**, 1529 (2010).

[27] Y. J. Kim, S. B. Jin, S. I. Kim, Y. S. Choi, I. S. Choi, and J. G. Han, J. Phys. D. Appl. Phys. **42**, 75412 (2009).

[28] M. F. a. M. van Hest, M. S. Dabney, J. D. Perkins, and D. S. Ginley, Thin Solid Films **496**, 70 (2006).

[29] R. Horng, K. Shen, and C. Yin, Opt. Express **21**, 14452 (2013).

[30] D. S. Ginley and C. Bright, MRS Bull. **25**, 15 (2011).

[31] K. Tamura, K. Nakahara, M. Sakai, D. Nakagawa, N. Ito, M. Sonobe, H. Takasu, H. Tampo, P. Fons, K. Matsubara, K. Iwata, A. Yamada, and S. Niki, Phys. Stat. Sol. **201**, 2704 (2004).

[32] M.-C. Jun, S.-U. Park, and J.-H. Koh, Nanoscale Res. Lett. **7**, 639 (2012).

[33] L.-Y. Chen, W.-H. Chen, J.-J. Wang, F. C.-N. Hong, and Y.-K. Su, Appl. Phys. Lett. **85**, 5628 (2004).

[34] S. W. Shin, S. M. Pawar, T.-W. Kim, J.-H. Moon, and J. H. Kim, J. Mater. Res. **24**, 441 (2012).

[35] H. Q. Le, S. K. Lim, G. K. L. Goh, S. J. Chua, and J. Ong, J. Electrochem. Soc. **157**, H796 (2010).

[36] H. Kim, G. P. Kushto, R. C. Y. Auyeung, and A. Piqué, Appl. Phys. A **93**, 521 (2008).

[37] H. Agura, A. Suzuki, T. Matsushita, T. Aoki, and M. Okuda, Thin Solid Films **445**, 263 (2003).

[38] S.-M. Park, T. Ikegami, and K. Ebihara, Thin Solid Films **513**, 90 (2006).

[39] H. Kim, J. . Horwitz, S. . Qadri, and D. . Chrisey, Thin Solid Films **420**–**421**, 107 (2002).

[40] S. Chen, H. Syu, C. Liao, Y. Chang, and C. Huang, **34**, 972 (2013).

[41] K. Yen, C. Chiu, C. Li, C. Chou, P. Lin, T. Chen, T. Lin, and J. Gong, IEEE Photonics Technol. Lett. **24**, 2105 (2012).

[42] H. Q. Le and S. J. Chua, J. Phys. D. Appl. Phys. **44**, 125104 (2011).

[43] J. H. Kim, E.-M. Kim, D. Andeen, D. Thomson, S. P. DenBaars, and F. F. Lange, Adv. Funct. Mater. **17**, 463 (2007).

[44] S. W. Shin, G. L. L. Agawane, I. Y. Kim, S. H. Jo, M. S. Kim, G.-S. S. Heo, J. H. Kim, and J. Y. Lee, Surf. Coatings Technol. **231**, 364 (2013).

[45] A. H. Reading, J. Richardson, C.-C. Pan, S. Nakamura, and S. P. DenBaars, Opt. Express **20**, A13 (2012).

[46] T. Margalith, O. Buchinsky, D. A. Cohen, A. C. Abare, M. Hansen, S. P.

DenBaars, and L. a. Coldren, Appl. Phys. Lett. **74**, 3930 (1999).

[47] K.-M. Chang, J.-Y. Chu, and C.-C. Cheng, Solid. State. Electron. **49**, 1381 (2005).

[48] Y. S. Jung, Thin Solid Films **467**, 36 (2004).

[49] M. V. Bogdanov, K. a. Bulashevich, O. V. Khokhlev, I. Y. Evstratov, M. S. Ramm, and S. Y. Karpov, Phys. Status Solidi Curr. Top. Solid State Phys. **7**, 2127 (2010).

[50] X. W. Sun and H. S. Kwok, J. Appl. Phys. **86**, 408 (1999).

[51] R. E. Treharne, K. Hutchings, D. a Lamb, S. J. C. Irvine, D. Lane, and K. Durose, J. Phys. D. Appl. Phys. **45**, 335102 (2012).

[52] D. B. Thompson, J. J. Richardson, S. P. DenBaars, and F. F. Lange, Appl. Phys. Express **2**, 42101 (2009).

[53] A. Janotti and C. G. Van de Walle, Reports Prog. Phys. **72**, 126501 (2009).

[54] S. Krishnamoorthy, F. Akyol, P. S. Park, and S. Rajan, Appl. Phys. Lett. **102**, 113503 (2013).

[55] E. F. Schubert, *Light-Emitting Diodes*, 2nd ed. (Cambridge University Press, 2006).

[56] G. Haacke, J. Appl. Phys. **47**, 4086 (1976).

[57] R. Gordon, MRS Bull. 52 (2000).

[58] A. Stadler, Materials (Basel). **5**, 661 (2012).

[59] C.-C. Li and D.-H. Kuo, J. Mater. Sci. Mater. Electron. **25**, 1404 (2014).

[60] S. Kaneko, H. Torii, M. Soga, K. Akiyama, M. Iwaya, M. Yoshimoto, and T. Amazawa, Jpn. J. Appl. Phys. **51**, 01AC02 (2012).

[61] J. T. Leonard, D. A. Cohen, B. P. Yonkee, R. M. Farrell, S. P. Denbaars, J. S. Speck, and S. Nakamura, Under-Review (Journal Appl. Physics) **XX**, Manuscript Available on Request (2015).

[62] T. Ben-Yaacov, T. Ive, C. G. Van de Walle, U. K. Mishra, J. S. Speck, and

S. P. Denbaars, J. Electron. Mater. **39**, 608 (2010).

[63] K. Nakahara, K. Tamura, M. Sakai, D. Nakagawa, N. Ito, M. Sonobe, H. Takasu, H. Tampo, P. Fons, K. Matsubara, K. Iwata, A. Yamada, and S. Niki, Japanese J. Appl. Physics, Part 2 Lett. **43**, 8 (2004).

[64] M. Ylilammi, Thin Solid Films **279**, 124 (1996).

Chapter 2. Zinc Oxide Thin Film Growth

2.1. Introduction

Zinc Oxide (ZnO), a III-VI semiconductor with its direct and wide band gap (3.4 eV) as well as high exciton binding energy (60 meV), has and is attracting a significant amount of research attention due to its potential in a wide array of applications, especially in optoelectronics and transparent electronics [1]. These applications range from light emitters, low emissivity window coatings, and transparent conducting layers to piezoelectric transducers, sensors, and high power electronics [2]. Although ZnO has many desirable intrinsic properties, application of this material as the only active material in optoelectronic devices is hampered due to the lack of stable p-type dopants. Due to its wide band gap and ease of achieving n-type conductivity, ZnO thin films can simultaneously achieve high optical transparency and low electrical resistivity. Transparent electrodes composed of ZnO have been shown to apply to optoelectronic devices such as light emitting diodes (LEDs), [3,4] laser diodes, [5] and photovoltaics [6,7]. For example, hydrothermally deposited ZnO thin films have been shown to outperform both thin Ni/Au [8] Sb-doped In_2O_3 (ITO) [9] as current spreading transparent electrodes for InGaN based LEDs. In addition to those devices, conductive thin films containing zinc oxide can also be applied to thin film transistors, varistors,

piezoelectric transducers, as well as gas, chemical and biological sensors [10–12]. ZnO thin films can be readily made highly conductive through extrinsic substitutional doping such as with trivalent group three elements (i.e., B, Al, Ga, and In) [13,14]. ZnO films can also be easily patterned using either wet or dry etching methods [15]. When compared to transparent conductive electrodes such as ITO, ZnO can typically be deposited at lower costs using a greater variety of physical and chemical deposition techniques.

In this chapter, we will review the three different processes used for the growth of crystalline ZnO. These include hydrothermal crystal growth, atomic layer deposition (ALD), and electron beam (e-beam) deposition. We will also discuss the morphological and structural effects group III dopants have on these films.

2.2. Hydrothermal Growth of ZnO Thin Films

Background

Hydrothermal synthesis typically utilizes single or heterogeneous phase reactions in aqueous media at elevated temperatures and pressures to crystallize ceramic materials, such as metal oxides, directly from solution in a closed reaction vessel. Synthesis usually occurs at autogenous pressures corresponding to the saturated vapor pressure of the solution defined by the temperature and composition of the solution [16]. All forms of ceramics can be synthesized through this method including powders, fibers, single crystals, and both thin and thick film coatings on

a variety of substrates. For TCO materials, hydrothermal processing can take place in many combinations of metal precursors as the source, mineralizers to adjust the pH, and crystal growth modifiers to control crystal growth. The two most commonly synthesized TCO via a hydrothermal method is ITO [17] and ZnO [18]. Currently, only ZnO TCOs have been reported to grow as thin films [19] directly. One commonly used the method to hydrothermally grown ZnO thin films uses a Zn source, such as a nitrate salt, mineralizer, such as ammonium hydroxide, and crystal growth modifiers such as sodium citrate which can mitigate the growth of certain crystal faces [20]. The mineralizer is a key ingredient in the solution since it modifies the pH of the solution to change the solubility of the dissolved metal ions. This change in solubility is the thermodynamic driving force behind the formation of precipitates and the deposition of material on a substrate. Dopants can be easily incorporated into the films through the addition of additional nitrate salts such as Ga, In, and Al nitrates. Deposition temperatures are typically below 100 °C, while pressures are not much above atmospheric. **Figure 2.1**, shows an example of one method to deposit ZnO films hydrothermally, this process involves the use of a thin seed layer which can help guide the growth of a second, much thicker, layer.

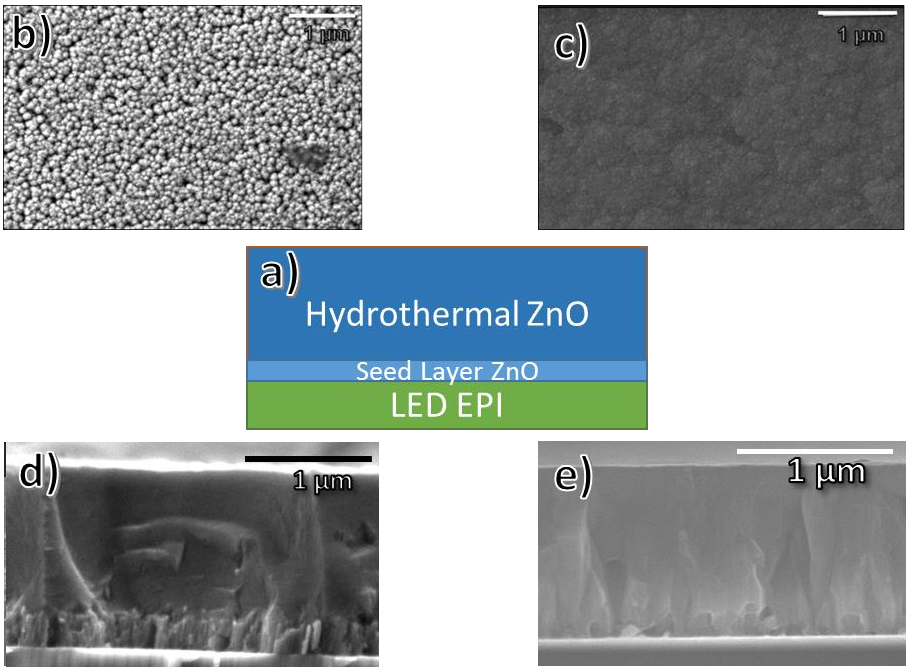

Figure 2.1 a) Schematic of ZnO deposition, SEM micrographs of b) hydrothermal ZnO seed layer c) hydrothermal ZnO bulk layer d) cross-sectional view of hydrothermal ZnO e) ZnO film using hybrid ALD seed/hydrothermal bulk layers

A significant advantage of this deposition method over the ones described earlier is its low cost and simple processing procedures. An alternative to the hydrothermal growth of a seed layer is through the deposition of a thin film of ZnO using atomic layer deposition (ALD) or electron beam (e-beam) deposition. This is advantageous given that these approaches can provide uniform films on which the much thicker hydrothermal film can grow from.

CHAPTER 2. Zinc Oxide Thin Film Growth

Overview of ZnO Growth

There exist several methods for depositing ZnO thin films. These include sol-gel, [21] metalorganic chemical vapor deposition (MOCVD), [22] molecular beam epitaxy (MBE), [23] pulsed laser deposition (PLD), [24] e-beam deposition, [25] thermal evaporation, [26] and dc magnetron sputtering. [27] All approaches have benefits and drawbacks in terms control over growth rate, uniformity, and composition. However, most require high vacuum conditions to operate, which increases production costs. Atmospheric or near atmospheric deposition schemes can drastically reduce the expenses associated with the deposition of this materials and allow for its widespread application. Atomic layer deposition (ALD) provides the precise growth of thin conformal coatings of ZnO on a variety of substrates, but the thickness is restricted to reasonable deposition times due to the self-limiting aspect of the growth mechanism [28]. If this technique can be successfully combined with a deposition method with faster growth rate, then it would be possible to practically grow transparent and conductive ZnO thin films on a variety of substrates for various applications. Hydrothermal growth [29], also referred to as chemical bath or aqueous solution deposition, of ZnO allows for the deposition of relatively thick films of ZnO with relatively fast growth rates at comparatively mild conditions of less than 100 °C and atmospheric or autogenous pressures. The composition and morphology of the film growth through this method can simply be changed through modifying the precursors in the growth solution. The growth

of ZnO occurs due to the presence of supersaturated Zn ions at elevated temperatures due to the retrograde solubility of Zn in aqueous solutions [30]. These films can be readily doped through the addition of impurities in growth solution such as the salts of group III elements.

Precursors for Hydrothermal Synthesis

As with any chemical reaction, precise control of the precursor chemicals used is essential to achieving repeatable and scalable results. For our experiments, we used the chemicals listed in **Table 2.1**. Zinc, oxygen, and dopant source is required to form doped ZnO films in solution. Zinc is provided by zinc nitrate, hydroxide ions in water provide the oxygen, and group III nitrate salts provide the impurity dopant.

Table 2.1 List of chemical precursors used for hydrothermal growth of ZnO

Chemical	Formula	Purpose	Supplier	Catalog #
zinc nitrate hexahydrate	$Zn(NO_3)_2 \cdot 6H_2O$	Zn source	Sigma Aldrich	96482-500G
sodium citrate tribasic dihydrate	$Na_3C_6H_5O_7 \cdot 2H_2O$	crystal growth modifier	Sigma Aldrich	C3434-250G
ammonium Hydroxide	NH_4OH	pH modifier	Sigma Aldrich	320145-500ML
aluminum nitrate Nonahydrate	$Al(NO_3)_3 \cdot 9H_2O$	Al source	Sigma Aldrich	237973-10G
gallium nitrate hydrate	$Ga(NO_3)_3 \cdot xH_2O$	Ga source	Sigma Aldrich	289892-25G
Indium nitrate hydrate	$In(NO_3)_3 \cdot xH_2O$	In source	Sigma Aldrich	326135-10G

In addition, the pH is modified by ammonium hydroxide, and film morphology is controlled by sodium citrate [48].

It is important to note that most of the precursors used are deliquescent salts. This means that when exposed to humidity in the air they readily absorb moisture. Given that UCSB is located by an ocean, humidity levels are typically high. Keeping these salts away from humidity is essential when dealing with concentrations in the millimolar range. Otherwise, the fraction of water in the hydrated salts may be higher than expected and expected concentrations would deviate significantly from actual values, making reproducibility an issue. To keep moisture away from the nitrate salts, they were stored in a dry box containing silica gel desiccant. Care was taken to not leave containers open for longer than necessary, and stock solutions were prepared to measure concentrations more accurately. Stock solutions should not be stored for very long, considering that CO_2 dissolved in the deionized water can react with the nitrate salts and form carbonates.

As seen in **Table 2.1**, the salts used as the Ga and In dopant sources do not label how many water molecules are present per molecule of the salt. The number of water molecules present in both the indium and gallium nitrate salts was determined by thermogravimetric analysis (TGA). [31] For this experiment a known weight of the salt was added to a small alumina crucible and heated 600 °C at a ramp rate of 10 °C/min in an N_2 environment. This heating drives off any water attached to the salts and allows one to determine water content. **Figure 2.2**(a) displays the results

of the TGA analysis in terms of % mass loss during heating for the Ga salts. The dehydration reaction can be expressed by the following reaction:

$2\ Ga(NO_3)_3\ xH_2O(s) \rightarrow Ga_2O_3(s) + N_2O_5(g) + xH_2O(g)$. Since the 23% of mass left after heating represents the Ga_2O_3 left over, it was determined that 8.4 moles of water were driven out of the salt, meaning that the chemical formula for the Ga nitrate salt is $Ga(NO_3)_3\ 8H_2O$. The same analysis can be conducted for the In salt, displayed in **Figure 2.2**(b), with the dehydration express by the following reaction: $2\ In(NO_3)_3\ xH_2O\ (s) \rightarrow In_2O_3 + N_2O_5 + xH_2O$. In this case, 40% of the mass was left over after heating, indicating that the amount water was such that the chemical formula for In nitrate is $In(NO_3)_3\ 3H_2O$.

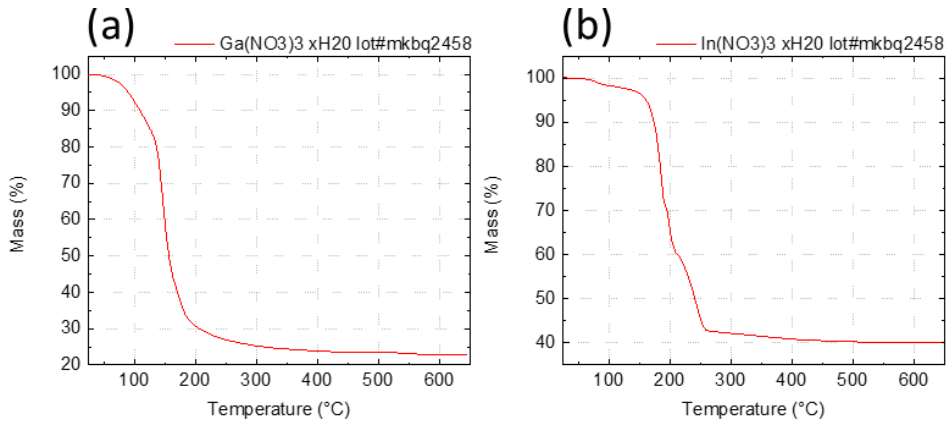

Figure 2.2 TGA analysis of (a) $Ga(NO_3)_3 \cdot xH_2O$ and (b) $In(NO_3)_3 \cdot xH_2O$

A simplified flow diagram of hydrothermal growth of ZnO is displayed in **Figure 2.3**. The process involves four steps. The first is a thin seed layer

deposition, followed by an anneal. The second is the growth of a much thicker 2nd layer, followed by a lower temperature anneal. More details about the growth conditions will be provided in subsequent chapters.

Figure 2.3 process flow diagram for hydrothermal ZnO growth

Two basic chemical reactions occur in solution to form ZnO [32]. The first is a hydroxide formation step, where Zn ions from the dissolved salt react with hydroxide ions in solution to form films of zinc hydroxides as shown in the reaction in the following reaction:

$$Zn^{2+}+2OH^{-} \rightarrow Zn(OH)_2$$

The zinc hydroxide in films then undergo a dehydration reaction to form the final zinc oxide films illustrated by the following reaction:

$$Zn(OH)_2 \rightarrow ZnO + H_2O$$

A similar mechanism likely occurs for the dopant which is introduced into a solution through their respective nitrate salts. Group III hydroxides and oxides must also form alongside ZnO during crystal growth. However, given their different elemental makeup, the reaction kinetics would be different to that of ZnO formation.

Substrates Requirements

The choice of substrate for ZnO growth is important in determining the properties of the films. Growing on top of GaN typically yield the best results, since ZnO share the same crystal structure and has similar lattice constants to the of GaN. Hydrothermal ZnO can epitaxially grow on most planes of GaN including c-plane and semi-polar orientation [4]. GaN templates grown on c-plane sapphire substrates are an easy way to generate GaN surfaces for ZnO thin film growth.

Another common substrate common substrate to grow ZnO on is (111) Mg-spinel, $MgAl_2O_4$. The c-plane (0001) orientation of ZnO can grow out of the (111) plane of Mg-spinel due to a 30° in-plane rotation allowing the closed packed oxygen directions of both materials to lay in a position with only a small lattice strain. Mg-Spinel substrate can be purchased as transparent double side polished wafers and are easy to characterize optically and electronically. They are also much less costly then wafers of bulk single crystal GaN.

Sapphire, Al_2O_3, was another substrate that was used for some experiments. Since the difference in lattice spacing is significant, a seed layers using a non-hydrothermal method must be used to deposit ZnO before hydrothermal grown. Films were grown on this substrate usually showed worse optoelectronic properties than those grown on GaN or Mg-spinel surfaces. Samples were diced into 1 cm^2 pieces so that they may be easily handled.

Seed Layer Experimental Conditions

Like the growth of GaN on sapphire, an initial layer of small highly oriented crystals of ZnO is required to form a single crystal film of ZnO hetero-epitaxially with low mosaicity. A seed layer is grown on the substrate to achieve this. This seed layer is formed by placing a sample in a solution containing $Zn(NO_3)_2$ which is heated to 90 °C and injecting a sufficient amount of NH_4OH to increase the pH of the solution from less than 4 to about 8. A picture of the experimental setup is shown in **Figure 2.4**. Zn containing salts exhibit retrograde solubility concerning temperature. This means that adding $Zn(NO_3)_2$ and NH_4NO_3 into deionized water at room temperature (20 °C) and heating the solution creates a supersaturation of Zn. The ammonium nitrate acts as a pH buffer for the solution. The injection of NH_4OH forces the precipitation of Zn into its hydroxide and oxide phase by increasing the hydroxide ion concentration in the films and further reducing the solubility of the Zn in solution.

Figure 2.4 Picture of experimental setup for hydrothermal ZnO seed layer growth

For a typical experiment, a 25 ml solution containing 350 mmol/L NH_4NO_3 and 20 mmol/L of $Zn(NO_3)_2 \cdot 6H_2O$ in 18 MΩ deionized (DI) water is placed in a 60 ml glass beaker and stirred using a Teflon coated stir bar set on a stir plate. An outer Kapton coated resistive heater is wrapped around the beaker, and the temperature is monitored and controlled by a Teflon insulated type K thermocouple attached to a temperature controller box. The solution can be heated to 90 °C while covered with a watch glass and stirred. Care must be taken to ensure that there are no air bubbles trapped between the sample surface and solution. Lowering the sample at an angle into the solution can help mitigate this issue. Once the solution has come to temperature, a Teflon holder containing the sample substrate to be coated is placed into the solution, with the growth surface face down. The solution is then allowed to come back to temperature, and 130 µL of NH_4OH is injected into

the solution using a calibrated adjustable volume pipette. Within a few seconds of injecting the NH_4OH, the solution turns from clear to cloudy white. This indicates that the Zn in solution has precipitated out as $ZnO/Zn(OH)_2$ crystallites both homogeneously into the solution and heterogeneously onto the sample surface. The sample sits in this solution for 1 min. The Teflon holder is then removed from the solution and rinsed with DI water. The samples are then removed from the holder and placed into a 70x50 crystallization dish containing about 50 ml of DI water. This is then put in a sonication bath for 1 min to remove any remaining free-floating ZnO particles. The solution in the dish is dumped and rinsed three times to remove any remaining loose particles.

The end-product can be seen by eye as a slightly iridescent white film on top of the substrate. Both the NH_4NO_3 and the $Zn(NO_3)_2$ in solution influences the seed layer film. As seen in **Figure 2.5**, increasing the NH_4NO_3 concentration in the solution increased the density of the nanocrystals on the films. The film thickness is on the order of 200 nm.

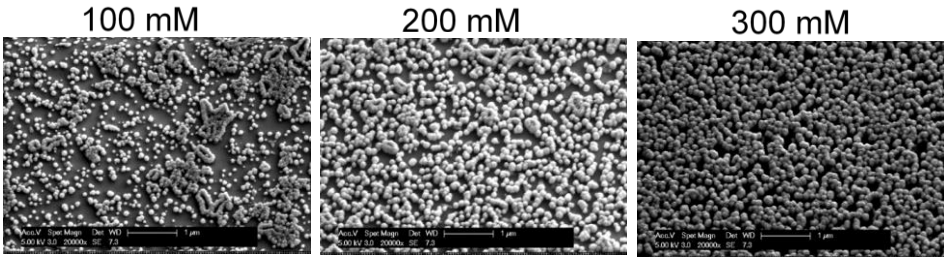

Figure 2.5 Effect of NH_4NO_3 concentration on ZnO seed layer films, all images taken at x20k magnification with the scale bar representing 1 µm

The spent seed layer solution must be disposed of properly since ZnO and dissolved Zn ions can be harmful to marine animals. All the glassware, thermocouple, and sample holders used in this step were rinsed with dilute nitric acid (1:4 /vol) and then DI water after the reaction was completed and samples removed.

After the deposition and washing step, samples are annealed in a rapid thermal annealer (RTA) for 10 min at 500 °C in N_2 ambient. This is to ensure that all excess $Zn(OH)_2$ has dehydrated to ZnO and that the contact resistance between the ZnO and p-GaN is reduced. More information about seed layer conditions can be found in Appendix A.

The main drawback with this method of depositing a ZnO seed layer is its difficulty with obtaining uniform and repeatable results. Keeping the sample face down gives the best results, but 's hard to maintain with the setup that was used. Throughput is also low since samples would have to be processed individually.

Alternative methods for seed layer deposition will be discussed in subsequent sections of this chapter.

Second Layer Experimental Conditions

After the seed layer is deposited and annealed, a much thicker second layer of ZnO is deposited using hydrothermal deposition. This layer coalesces the initial seed layer and forms the bulk of the film. Substrates were placed face up in a reaction vessel containing a 25 ml solution composed of 25 mmol/L zinc nitrate ($Zn(NO_3)_2$) and 5 mmol/L trisodium citrate ($Na_3C_6H_5O_7$) in 18 MΩ DI water. The reaction vessel used in these studies were 60 mL digestion vessel from Savillex Corp. Before submerging the substrates into solution, 1.3 ml of 29 wt% ammonium hydroxide (NH_3OH) was added to achieve a pH about 11. Calibration curves are shown in Figure 2.6.

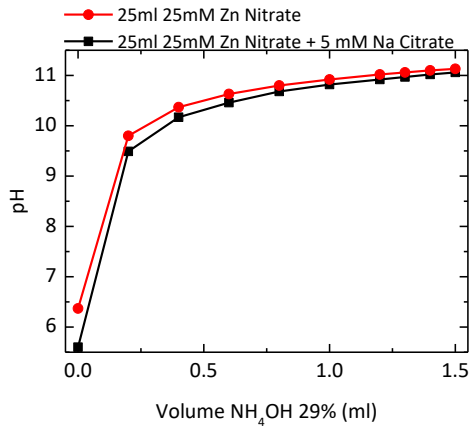

Figure 2.6 Change in pH as a function of NH_4OH addition

The reaction vessel was capped, placed in 90°C oven, and allowed to react for 2 h, after which the samples were rinsed with DI water. The samples then underwent a second RTA at 300° C for 10 min in the air before characterization or further devices processing. Doping of these films was carried out by simply adding between 0 to 1 mmol/L of either aluminum nitrate ($Al(NO_3)_3$), gallium nitrate ($Ga(NO_3)_3$), or indium nitrate ($In(NO_3)_3$) into the growth solution.

The driving force behind the growth of ZnO, in this case, is the steady increase in temperature of the solution when placed in a preheated oven. Since the pH is already quite high in the initial solution, the increase in temperature drives the Zn in solution to precipitate out as a film on the substrate. For our reactor, it took about 1 hour for the solution to reach 90 °C, as shown in **Figure 2.7**. This growth is guided by the seed crystals grown earlier. The $Na_3C_6H_5O_7$ in solution retards growth in the c-directions by preferentially binding to this polar plane. The films coalesce by growing out in the a and m planes and then grow upward. The film thickness can be varied by reaction run time and $Zn(NO_3)_2$ concentration. Typical film thicknesses were on the order of 1-2 μm. This method of growing ZnO is quite simple as it involves simple wet chemistry and mild conditions. Stock growth solutions can be prepared (without NH_3OH), and several reactions can be run in parallel.

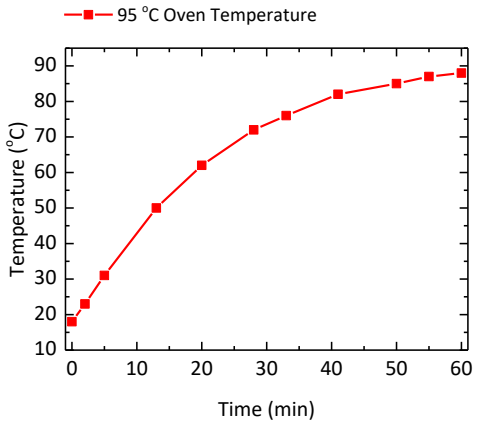

Figure 2.7 Temperature calibration curve for 2nd layer ZnO growth solution in 90 °C oven

Although the growth is mainly homogeneous nucleation on the ZnO seed layer, some heterogeneous nucleation occurs in solution, which is particles of ZnO in solution. Particle generation is suppressed when either Ga or Al nitrate salts are added to the growth solution. The spent growth solution must be disposed of properly since ZnO and dissolved Zn ions can be harmful to marine animals. As with seed layer growth, reactor vessels were rinsed with dilute nitric acid (1:4 /vol) and then DI water after the reaction was completed. The dilute nitric acid can be reused several times before having to make a new stock solution. More information about seed layer conditions can be found in Appendix A.

2.3. Atomic Layer Deposition of ZnO

Background

As its name would suggest, atomic layer deposition (ALD) is a self-limiting chemical vapor deposition technique that can deposit films with atomic monolayer precision. This is accomplished by alternating the injection of gaseous precursors into a chamber containing the substrate to be coated. The precursors chemisorb onto the substrate surface as a monolayer thick film. When the next precursor is introduced, it reacted with the first layer and formed the desired material. Conformal films of ZnO can readily be deposited using this technique. Its advantage over hydrothermal deposition of a seed layer is that it can be utilized in a variety of large area substrates.

ZnO Reaction

For our experiments, we used diethyl zinc, $Zn(C_2H_5)_2$, and water, H_2O, for precursors as zinc and oxygen sources respectively. The reaction is simply $Zn(C_2H_5)_2$ (g) + H2O (g) → ZnO (s) + $2C_2H_6$ (g). As shown in **Figure 2.8**, the deposition occurs in four step cycles. The substrate is heated to a temperature between 200 to 300 °C, and the reactor is purged of any air. Diethylzinc is flown into the reactor and allowed to form a monolayer. This gas is then evacuated using an N_2 purge. Water vapor is then introduced and allowed to react with the diethyl

zinc to form ZnO. The reactor is again purged using nitrogen gas prior to the start of a new cycle.

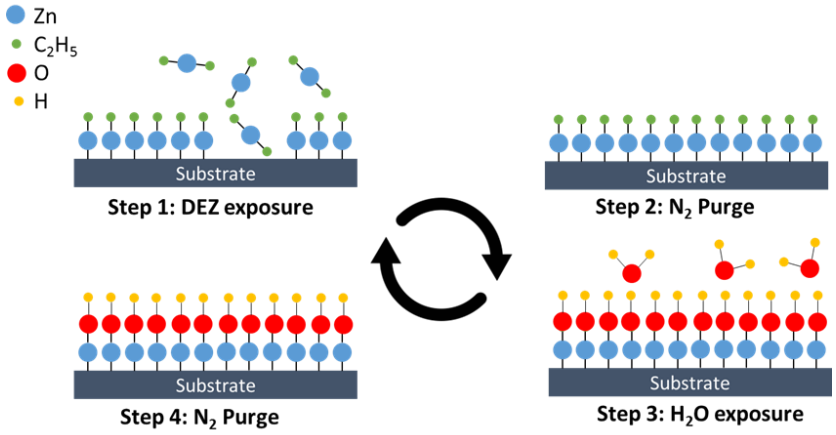

Figure 2.8 schematic outline of the steps involved in ALD ZnO

Run Conditions

ALD ZnO films were successfully deposited on several substrates, including GaN, Al_2O_3, and thermally oxidized Si. Films deposited on thermally oxidized silicon substrates were used as thickness monitors by analyzing the films with ellipsometry models. The growth rates of the films were determined to be approximately 1.6 Å/cycle, Figure 2.9(a). This corresponds to slightly less than a theoretical monolayer of 2.14 Å per cycle, indicating that a full monolayer coverage may not be achieved during each cycle. Nevertheless, thin films of ZnO were shown to be able to be grown on all substrates studied.

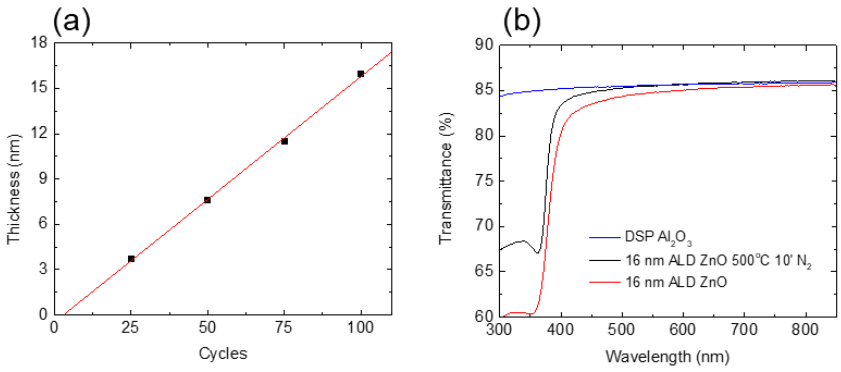

Figure 2.9 (a) thickness vs. ALD cycle for ZnO deposited @ 200 °C using DEZ and water (b) Optical transmission spectra of sapphire (blue), 16 nm ZnO before thermal anneal (red) and after 500 °C anneal (black)

It was also found that by annealing at 500 °C for 10 min in 80/20% N_2/O_2, the ALD ZnO films increased their transparency when measured on double side polished sapphire samples, Figure 2.9(b).

2.4. Electron Beam Deposition of ZnO

Background

As the name implies electron beam deposition utilizes a focused beam of electrons onto a target material, which is then vaporized and allowed to travel under vacuum to your substrate. In the case of ZnO, either pure Zn metal or ZnO could be used. Oxygen can also be flown into the chamber to improve the layers stoichiometry. This method was used to deposit an alternative seed layer since there still are repeatability issues with hydrothermal seed layers.

Run Conditions

Alfa Aesar zinc oxide pellets (stock # 44264) were used as the source material for these experiments. The chamber was pumped down to below $1x10^{-6}$ torr, and the sample was heated to 300 °C by setting the stage temperature to 600 °C. 30 sccm of oxygen was flown into the reactor, raising its pressure to ~$3x10^{-4}$ Torr. Films formed using this method were typically dark/black, likely due to oxygen deficiencies. Films were annealed in an RTA at 500 °C for 15 min in 80/20% N_2/O_2 environment, after which they turned transparent by eye. **Figure 2.10** shows that this method created films composed of a platelet-like structure. Deposition thickness was set to 200nm, but actual thickness ~20 nm when measured with ellipsometry after annealing. It is difficult to accurately monitor the deposition since the quartz crystal monitor was not heated. Unfortunately, due to chamber fouling from the highly mobile Zn vapor, only a few experiments were conducted using e-beam deposition. The results of which are presented in chapter 6.

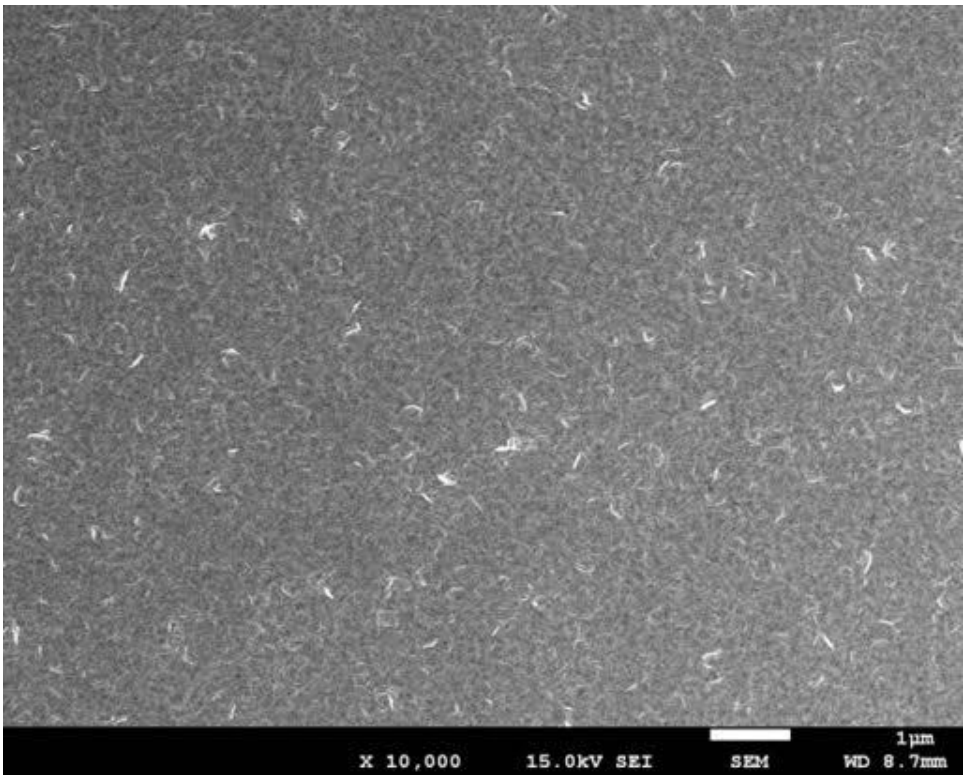

Figure 2.10 SEM micrograph of e-beam deposited ZnO seed layer

2.5. Determining Proper Dopants for Hydrothermal ZnO

As grown, hydrothermal ZnO exhibits significant n-type conductivity. Native point defects such as oxygen vacancies and zinc interstitial are commonly cited as the source of unintentional n-type conductivity in ZnO. However, it has been

shown through first-principles calculations that are not likely the case. Zinc interstitials are proved to be shallow donors; oxygen vacancies are found to be deep donors in ZnO [33]. One feasible alternative explanation for unintentional n-type conductivity in ZnO is the unintentional incorporation of hydrogen as a donor impurity.

Hydrogen is a ubiquitous element that is extremely difficult to remove from the environment in which ZnO films are grown. In most semiconductors, hydrogen exhibits amphoteric behavior such that it counteracts the prevailing conductivity of the material. However, it has been found through first-principles calculations that in ZnO hydrogen is very likely to behave exclusively as a donor dopant [34]. These results have also been confirmed experimentally [35]. Hydrogen is thought to most stable when occupying an O substitutional site [36]. It can also occupy interstitial sites such as bond centers in ZnO, bind strongly to O to form hydroxyls. In both cases, hydrogen acts as a shallow donor.

In addition to unintentional donor dopants and impurities, ZnO can be further doped n-type through the addition of several elemental donor impurities. The most common donor dopants for ZnO are found to be group III elements such as Al, Ga, and In. All three readily form shallow donor states in ZnO given their low activation energies [13].

The possibility of p-type conductivity in ZnO has stirred quite a bit of controversy in the literature. Group I metals (Li, Na, and K) when found in Zn

substitutional sites are thought to form acceptors in ZnO, but their activation energies are not agreed upon. Many also report nitrogen behaving a shallow acceptor. However, nitrogen has been shown to act as a deep level acceptor shown experimentally through photoluminescence (PL) experiments [37] and theoretically by calculated configuration-coordinate diagrams [38]. Hall measurements are claiming p-type conductivity may be explained by inhomogeneous doping concentrations [39], low carrier mobilities, or contact misplacement [40].

Doped hydrothermal ZnO films have been demonstrated for In [41] Ga [42] and In/Ga co-doping [43]. However, to date no systematic study on the effect of dopants on structural and optical properties of hydrothermal ZnO films. **Table 2.2** lists possible substitutional or interstitial dopant elements.

Table 2.2 List of possible dopants for hydrothermal ZnO along with their respective charge, precursors, atomic coordination number (C#), and ionic radii

Ion	precursor	C #	radius (Å)	Ion	precursor	C #	radius (Å)
Zn^{+2}	$Zn(NO_3)_2$	4	0.60 (0%)	Mn^{+2}	$Mn(NO_3)_2$	4	0.66 (10%)
Li^{+1}	$LiNO_3$	4	0.59 (-2%)	Fe^{+3}	$Fe(NO_3)_3$	4	0.49 (-18%)
Na^{+1}	$NaNO_3$	4	0.99 (65%)	Co^{+3}	$Co(NO_3)_3$	4	0.56 (-7%)
K^{+1}	KNO_3	4	1.37 (128%)	Ni^{+2}	$Ni(NO_3)_2$	4	0.49 (-18%)
Mg^{+2}	$Mg(NO_3)_2$	4	0.57 (-5%)	Pb^{+2}	$Pb(NO_3)_2$	8	1.29 (115%)

Ca^{+2}	$Ca(NO_3)_2$	6	1.00 (67%)	Cu^{+2}	$Cu(NO_3)_2$	4	0.57 (-5%)
Sc^{+3}	$Sc(NO_3)_3$	6	0.75 (25%)	Ag^{+1}	$AgNO_3$	8	1.15 (92%)
Ti^{+4}	$Ti(NO_3)_4$	4	0.42 (-30%)	Cd^{+3}	$Cd(NO_3)_3$	4	0.78 (30%)
Zr^{+4}	$Zr(NO_3)_4$	4	0.59 (-2%)	Al^{+3}	$Al(NO_3)_3$	4	0.39 (-35%)
V^{+3}	VCl_3	4	0.64 (7%)	Ga^{+3}	$Ga(NO_3)_3$	4	0.47 (-22%)
Cr^{+3}	$Cr(NO_3)_3$	3	0.62 (3%)	In^{+3}	$In(NO_3)_3$	4	0.62 (3%)

Transition metals are commonly used to alter the magnetic properties of ZnO but are typically not used to increase its conductivity [44]. Given that group III elements have a +3 charge state compared to Zn's +2, excess electrons can be produced by doping with these elements. Of the group III dopants, In shows the least difference in ionic radius compared to that of Zn, followed by Ga then Al.

2.6. Growth Rate & Dopant Concentration

Growth of doped hydrothermal ZnO thin films on spinel substrates was carried out in a manner similar to that of Andeen et al. [19] Prior to deposition, 1 cm^2 (111) $MgAl_2O_4$ spinel substrates (MTI, Richmond, CA) were cleaned by 3 min dips in acetone and isopropanol followed by an 18 MΩ deionized (DI) water rinse and 5 min dip in a 1:1 solution of HCl and H_2O. The substrates were then rinsed again with DI water and dried under N_2. A 5 nm thick seed layer was deposited onto the substrate at 200 °C using a FlexAl ALD system (Oxford Instruments, Abingdon, UK) with $(C_2H_5)_2Zn$ and H_2O as precursors. This layer was then annealed at 600

°C for 10 min in air using an AET RX6 rapid thermal anneal (RTA) system. Following this, the substrates were placed in a 60 ml perfluoro alkoxy (PFA) reaction vessel (Savillex, Eden Prairie, MN) containing a 25 ml solution composed of 25 mM $Zn(NO_3)_2$ $6H_2O$ (Sigma-Aldrich, St. Louis, MO), 5 mM $Na_3C_6H_5O_7$ (Sigma-Aldrich, St. Louis, MO) and 0 to 1 mM of either $Al(NO_3)_3$ $9H_2O$, $Ga(NO_3)_3$ $8H_2O$, or $In(NO_3)_3$ $8H_2O$ (Sigma-Aldrich, St. Louis, MO) dissolved in DI water. Before submerging the substrates into solution, 1.3 ml of 29 wt% NH_3OH (Sigma-Aldrich, St. Louis, MO) was added to achieve a pH of 11. The reaction vessel was capped, placed in 90 °C oven, and allowed to react for 2 hours, after which the samples were rinsed with DI water and dried with N_2. All samples then underwent a second RTA at 300 ° C for 10 min in air prior to characterization.

Film morphology was observed using a field emission scanning electron microscope (FESEM, JEOL 7600F). Film thickness was determined by surface profilometry measurements (Dektak 6M). ICP-AES (Thermo iCAP 6300) was used to establish group III impurity concentrations within the thin films quantitatively. [46] ZnO films were dissolved into a 2% HNO_3 solution. Optical absorption intensities related to the relevant elements, produced using an Ar plasma, were then compared to calibration curves produced from standard solutions with known concentrations of dissolved elements in question (i.e., Zn^{2+}, Al^{3+}, Ga^{3+}, and In^{3+}) in a 2% HNO_3 solution.

The thin films that resulted from the hydrothermal growth of doped ZnO on an ALD seed layer had thicknesses which ranged between 1 to 3 micrometers. A cross-sectional SEM micrograph of a typical ZnO thin film on a spinel substrate is shown in **Figure 2.11**. The nanoscale pores form during the second annealing step and can be caused by either the coalescence of zinc vacancies [47] or the result of a phase change that occurs from the dehydration of less dense $Zn(OH)_2$ to the denser ZnO phase. [32] The porosity of these films decreased with increasing dopant concentrations with films doped at 1mM generally showing very little porosity.

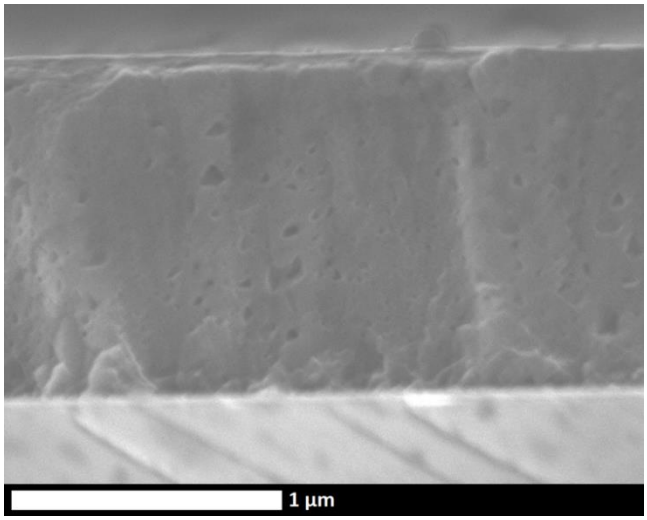

Figure 2.11 SEM cross-sectional micrograph of a typical ALD/ Hydrothermal ZnO thin film on spinel substrate after annealing

Figure 2.12(a) shows cross-sectional SEM micrographs of an unintentionally doped hydrothermal ZnO thin film prior to annealing. This morphology was similar in morphology to the doped films grown for this study. Film thicknesses ranged between 0.5 to 2.5 μm, depending on dopant type and concentration in solution. The growth rate of the films varied significantly with dopant type. As seen in **Figure 2.12**(b), increasing dopant concentrations generally resulted in a decrease in growth rate of the films. Films grown in solutions containing In showed the most drastic decrease, while those with Ga had a stable growth rate until 0.6 mM was added. Since hydrothermal ZnO growth is dependent on charges at the surface of the growth direction, the introduction of nitrate salts composed of trivalent metals may affect these charges leading to slower growth [49]. For instance, it has been shown that the presence of In^{3+} suppresses the growth rate along the +c direction in ZnO due to the partial replacement of Zn^{2+} with In^{3+} resulting in a decrease of the positive charge of the surface and a reduction in the incorporation of negatively charged Zn containing species [50].

Dopant concentration within the films was determined through performing inductively coupled plasma – atomic emission spectroscopy (ICP-AES) on doped ZnO thin films dissolved in dilute nitric acid. Survey scans showed the presence of only Zn and the group III dopants within the films. **Figure 2.12**(c) indicates the relationship between the concentration of group III nitrate salts and the concentration of those elements within the film. Dopant concentrations ranged

between 0 to 0.5 at. % within the films measured, with 0.5 at % correlating to a dopant density of approximately $2(10)^{20}$ cm^{-3}. Both Ga and Al-doped films showed fairly linear incorporation into the film with the addition of higher concentrations of their respective precursors in solution. However, In-doped films begin to show signs of saturation in dopant incorporation at much lower precursor concentrations. This difference in dopant incorporation rates may be related to the electronegativity of the elements.

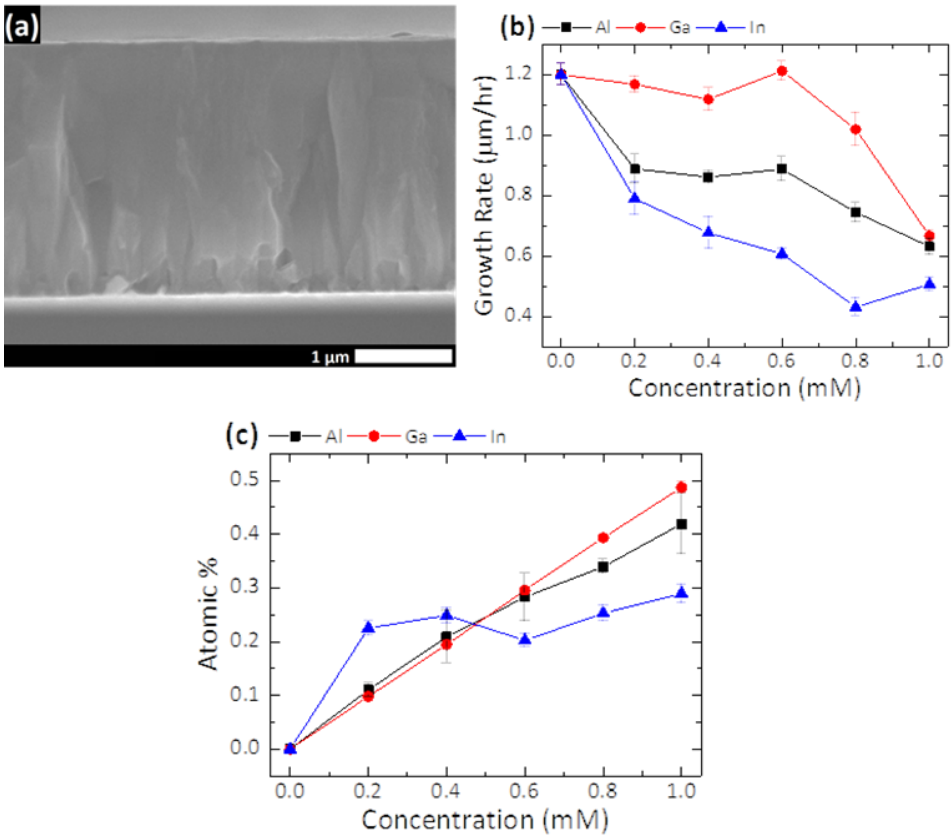

Figure 2.12 a) cross-sectional SEM micrograph of a hydro-thermal ZnO thin film prior to annealing b) growth rates for ZnO films deposited under varying concentrations of Al, Ga, and In in solution. c). ICP-AES calibration curves relating

molar concentrations of the dopant precursor in solution to at. % of the dopants in the films

It is known that Zn and Ga have the most similar electronegativity values, while they are the most dissimilar with In [51]. Incorporation of In into hydrothermal ZnO has been shown to be challenging [52], given that it can form phase separated In hydroxide [53].

2.7. Morphology & Crystal Structure

Morphology

Atomic force microscopy (AFM), using a Bruker Dimension Icon AFM system, was carried out in most of the samples discussed in this paper. AFM scans were conducted under tapping mode. **Figure 2.13** displays the AFM scan results, with the insets indicating the type and roughness of the films. The ALD ZnO films were slightly less rough than the bare spinel substrate, possibly due to polishing scratches being buried under the layer. Analysis carried out on these films show that the root mean square (rms) roughness varied between 3.9 to 8.9 nm with the surface of In-doped films being rougher than the other cases The smoothest sample was found to be the 0.2 mM Al-doped film, while the roughest was the 0.6 mM Ga doped film. A complete listing of root mean square roughness measurements are provided in Table 2.3. Roughness values did not correlate well with electrical properties. Although the most conductive sample, 0.8mM Ga, did have relatively smoother

surface morphology (4.15 nm), the second most conductive sample, 0.6mM Ga, was the roughest film measured.

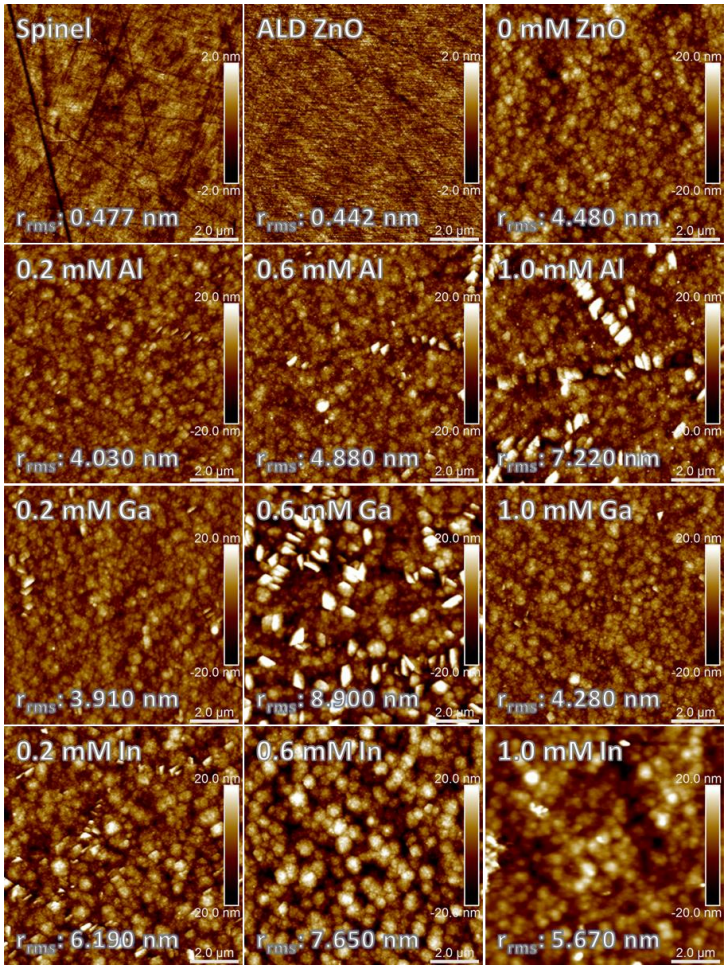

Figure 2.13 AFM scans of bare spinel, ALD ZnO, undoped ZnO, and selection of doped ZnO films

Table 2.3 Root mean square (RMS) roughness for spinel substrates, ALD ZnO template, and select ZnO thin films.

Sample	r_{rms} (nm)	Sample	r_{rms} (nm)	Sample	r_{rms} (nm)
25cy ZnO	0.442	**0.2mM Ga**	3.910	**0.2mM In**	6.190
0.0mM	4.480	**0.4mM Ga**	4.340	**0.6mM In**	7.650
0.2mM Al	4.030	**0.6mM Ga**	8.900	**1.0mM In**	5.670
0.6mM Al	4.880	**0.8mM Ga**	4.150	**Spinel**	0.477
1.0mM Al	7.220	**1.0mM Ga**	4.280		

Crystal Structure

X-ray diffraction spectra were collected using a Panalytical MRD PRO high-resolution x-ray diffractometer with a Cu kα1 (1.5405 Å) source. A triple axis configuration was used to acquire on axis 2θ/ω spectra, while a double axis, rocking curve, the configuration was used for on-axis omega scans and off-axis phi scans.

Figure 2.14 displays a log scale plot of a 2theta/omega scan of an unintentionally doped (UID) ZnO thin film. Although the (0002) reflection of the ZnO film and the (111) reflection of the $MgAl_2O_4$ are the major features, the scans show a weak reflection from the $(10\bar{1}1)$ plane of ZnO as well. This feature is found in several but not all the doped samples as well. It indicates that the film and substrate have a $<111>_{MgAl2O4} \parallel <0001>_{ZnO}$ out of plane orientation.

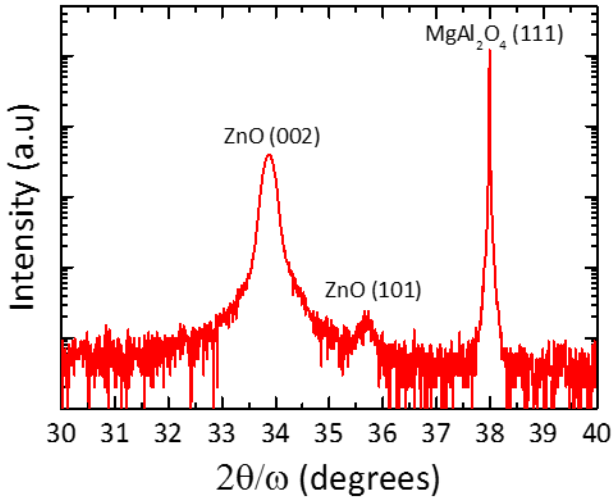

Figure 2.14 2theta/omega scans of UID ZnO film

Their in-plane alignment was determined by off-axis phi scans of the (10-11) ZnO and (400) $MgAl_2O_4$ peaks, shown in **Figure 2.15**. The respective peaks of the substrate and film lineup, meaning that they have $<\bar{1}\bar{1}2>_{MgAl2O4}$ || $<01\bar{1}0>_{ZnO}$ and $<\bar{1}\bar{1}0>_{MgAl2O4}$ || $<2\bar{1}\bar{1}0>_{ZnO}$ in-plane orientation. This indicates that the closed packed oxygen planes of both ZnO and $MgAl_2O_4$ are aligned with a lattice mismatch of 13.6%, similar to MBE grown films [54]. Sputtered and hydrothermal ZnO seed layers on $MgAl_2O_4$ typically have a 30° rotation of the between the closed packed oxygen directions, resulting in a much smaller lattice strain [19,55]. The well-defined six-fold symmetry of the (10-11) peak of ZnO is also indicative of a highly c-plane oriented film.

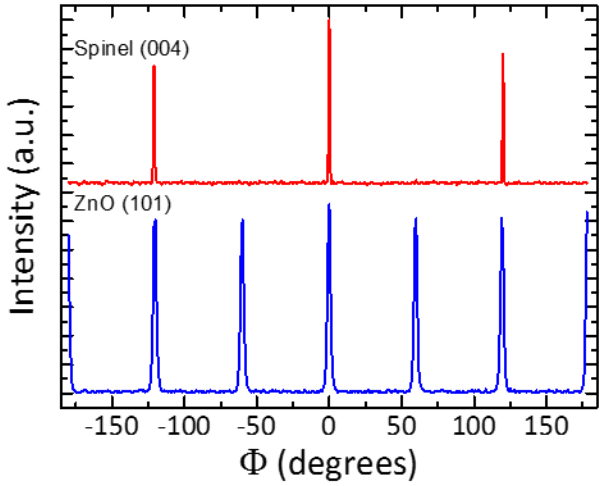

Figure 2.15 Off-axis phi scans for Spinel (400) and ZnO (101) reflections

The large lattice mismatch between film and substrate results in films with a high degree of mosaicity. A representative rocking curve scan, shown in **Figure 2.16**(a), was fitted to a Gaussian function from which line widths were determined. The line widths of films doped by varying the concentration of Al, Ga, and In in they hydrothermal growth solution are shown in **Figure 2.16**(b). The overall trend shows that increasing the concentration of dopant initially increases the films mosaic spread, but at a certain concentration the films crystal quality improves. It is believed that the group III elements in the hydrothermal growth solution undergo a similar dehydration reaction from a hydroxide phase to an oxide during film formation [52]. At a certain concentration, the lattice strain that is formed by the

incorporation of a dopant of a different ionic radius into the film may offset the strain brought on by the lattice mismatch between film and substrate. This may allow for the growth of ZnO films with a lower defect density.

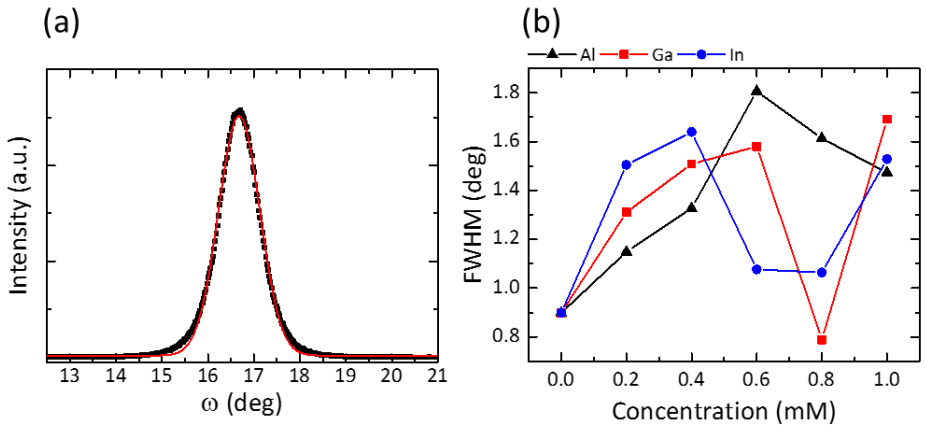

Figure 2.16 (a) rocking curve scan of the (002) ZnO reflection (b) FWHM of rocking curve scans for doped ZnO films

2.8. Conclusions

In summary, we have successfully demonstrated that doped hydrothermal thin films of ZnO can be grown on ALD ZnO seed layers. Dopant concentrations in the films can be precisely measured using ICP-AES. Although its crystalline quality and roughness are not ideal, this approach is an acceptable method for evaluating the effects that dopants have on the optoelectronic properties of the films. In the next chapter, we will discuss in detail the results of the optoelectronic characterization of these films.

2.9. References

[1] C. Klingshirn, Phys. Status Solidi Basic Res. **244**, 3027 (2007).

[2] D. C. Look, Mater. Sci. Eng. B **80**, 383 (2001).

[3] A. J. Mughal, S. Oh, A. Myzaferi, S. Nakamura, J. S. Speck, and S. P. DenBaars, Electron. Lett. **52**, 304 (2016).

[4] J. Richardson, I. Koslow, C.-C. Pan, Y. Zhao, J.-S. Ha, and S. P. DenBaars, Appl. Phys. Express **4**, 126502 (2011).

[5] M. Stattin, J. Bengtsson, and A. Larsson, Jpn. J. Appl. Phys. **52**, 54001 (2013).

[6] E. Fortunato, L. Raniero, L. Silva, a Goncalves, a Pimentel, P. Barquinha, H. Aguas, L. Pereira, G. Goncalves, and I. Ferreira, Sol. Energy Mater. Sol. Cells **92**, 1605 (2008).

[7] X. Liu, X. Li, Y. Li, C. Song, L. Zhu, W. Zhang, H.-Q. Wang, and J. Fang, Adv. Mater. **28**, 7405 (2016).

[8] D. B. Thompson, J. J. Richardson, S. P. DenBaars, and F. F. Lange, Appl. Phys. Express **2**, 42101 (2009).

[9] A. H. Reading, J. Richardson, C.-C. Pan, S. Nakamura, and S. P. DenBaars, Opt. Express **20**, A13 (2012).

[10] U. Ozgur, D. Hofstetter, and H. Morkoc, Proc. IEEE 1255 (2010).

[11] H. Morkoç and U. Ozgur, in *Zinc Oxide Fundam. Mater. Device Technol.* (Wiley-VCH, 2009), pp. 1–76.

[12] H. C. Cheng, C. F. Chen, and C. C. Lee, Thin Solid Films **498**, 142 (2006).

[13] A. Janotti and C. G. Van de Walle, Reports Prog. Phys. **72**, 126501 (2009).

[14] T. Minami, H. Sato, H. Nanto, and S. Takata, Jpn. J. Appl. Phys. **24**, L781 (1985).

[15] H. Zheng, X. L. Du, Q. Luo, J. F. Jia, C. Z. Gu, and Q. K. Xue, Thin Solid Films **515**, 3967 (2007).

[16] W. L. W. Suchanek and R. E. Riman, Adv. Sci. Technol. **45**, 184 (2006).

[17] X. Li and G. M. Kale, J. Phys. Conf. Ser. **26**, 319 (2006).

[18] J.-L. Wang, P.-Y. Yang, T.-Y. Hsieh, C.-C. Hwang, and M.-H. Juang, J. Nanomater. **2013**, 1 (2013).

[19] D. Andeen, L. Loeffler, N. Padture, and F. F. Lange, J. Cryst. Growth **259**, 103 (2003).

[20] J. H. Kim, E.-M. Kim, D. Andeen, D. Thomson, S. P. DenBaars, and F. F. Lange, Adv. Funct. Mater. **17**, 463 (2007).

[21] M. Ohyama, H. Kouzuka, and T. Yoko, Thin Solid Films **306**, 78 (1997).

[22] R. Horng, K. Shen, and C. Yin, Opt. Express **21**, 14452 (2013).

[23] H. J. Ko, Y. F. Chen, S. K. Hong, H. Wenisch, T. Yao, and D. C. Look, Appl. Phys. Lett. **77**, 3761 (2000).

[24] A. Suzuki, T. Matsushita, T. Aoki, Y. Yoneyama, and M. Okuda, Jpn. J. Appl. Phys. **40**, L401 (2001).

[25] A. N. Gruzintsev, V. T. Volkov, and L. N. Matveeva, Russ. Microelectonics **31**, 227 (2002).

[26] O. A. Fouad, A. A. Ismail, Z. I. Zaki, and R. M. Mohamed, Appl. Catal. B Environ. **62**, 144 (2006).

[27] Z.-C. C. Jin, I. Hamberg, and C. G. Granqvist, J. Appl. Phys. **64**, 5117 (1988).

[28] T. Tynell and M. Karppinen, Semicond. Sci. Technol. **29**, 43001 (2014).

[29] R. E. Riman, W. L. Suchanek, and M. M. Lencka, Ann. Chim. Sci. Des Mater. **27**, 15 (2002).

[30] J. Richardson and F. F. Lange, Cryst. Growth Des. **9**, 2570 (2009).

[31] V. Berbenni, C. Milanese, G. Bruni, and A. Marini, J. Therm. Anal. Calorim. **82**, 401 (2005).

[32] N. J. Nicholas, G. V. Franks, and W. a. Ducker, CrystEngComm **14**, 1232

(2012).

[33] A. Janotti and C. G. Van De Walle, Phys. Rev. B - Condens. Matter Mater. Phys. **76**, 1 (2007).

[34] C. G. Van De Walle, Phys. Rev. Lett. **85**, 1012 (2000).

[35] L.-Y. Chen, W.-H. Chen, J.-J. Wang, F. C.-N. Hong, and Y.-K. Su, Appl. Phys. Lett. **85**, 5628 (2004).

[36] M. D. McCluskey and S. J. Jokela, J. Appl. Phys. **106**, 1 (2009).

[37] M. C. Tarun, M. Z. Iqbal, and M. D. McCluskey, AIP Adv. **1**, 22105 (2011).

[38] J. L. Lyons, a. Janotti, and C. G. Van de Walle, Appl. Phys. Lett. **95**, 252105 (2009).

[39] O. Bierwagen, T. Ive, C. G. Van De Walle, and J. S. Speck, Appl. Phys. Lett. **93**, 0 (2008).

[40] T. Ohgaki, N. Ohashi, S. Sugimura, H. Ryoken, I. Sakaguchi, Y. Adachi, and H. Haneda, J. Mater. Res. **23**, 2293 (2008).

[41] L. H. Quang, L. Swee Kuan, and G. G. Kia Liang, J. Cryst. Growth **312**, 437 (2010).

[42] H. Q. Le, S. K. Lim, G. K. L. Goh, S. J. Chua, and J. Ong, J. Electrochem. Soc. **157**, H796 (2010).

[43] H. Q. Le and S. J. Chua, J. Phys. D. Appl. Phys. **44**, 125104 (2011).

[44] K. Ueda, H. Tabata, and T. Kawai, Appl. Phys. Lett. **79**, 988 (2001).

[45] D. K. Schroder, *Semiconductor Material and Device Characterization* (John Wiley & Sons, Inc., Hoboken, NJ, USA, 2005).

[46] A. Gorgulla, D. P. Ertel, M. Steyer, G. Hahn, and B. Terheiden, Energy Procedia **77**, 687 (2015).

[47] J. Richardson, G. K. L. Goh, H. Q. Le, L.-L. Liew, F. F. Lange, and S. P. DenBaars, Cryst. Growth Des. **11**, 3558 (2011).

[48] L. Schmidt-Mende and J. L. MacManus-Driscoll, Mater. Today **10**, 40

(2007).

[49] L. N. Demianets, D. V. Kostomarov, I. P. Kuz'mina, and S. V. Pushko, Crystallogr. Reports **47**, S86 (2002).

[50] L. N. Demianets and D. V Kostomarov, Ann. Chim. Sci. Des Matériaux **26**, 193 (2001).

[51] S. Kohiki, M. Nishitani, and T. Wada, J. Appl. Phys. **75**, 2069 (1994).

[52] A. Escobedo Morales, M. Herrera Zaldivar, and U. Pal, Opt. Mater. (Amst). **29**, 100 (2006).

[53] E. Pál, V. Hornok, A. Oszkó, and I. Dékány, Colloids Surfaces A Physicochem. Eng. Asp. **340**, 1 (2009).

[54] Y. Chen, S. Hong, H. Ko, M. Nakajima, T. Yao, and Y. Segawa, Appl. Phys. Lett. **76**, 245 (2000).

[55] S. W. Shin, Y. Bin Kwon, a. V. Moholkar, G.-S. Heo, I. O. Jung, J.-H. Moon, J. H. Kim, and J. Y. Lee, J. Cryst. Growth **322**, 45 (2011).

Chapter 3. ZnO Optoelectronic Characterization

3.1. Introduction

This chapter continues the evaluation of the doped ZnO films started in the previous chapter. Whereas chapter 2 discussed growth, morphology, and crystal structure of the group III doped ZnO thin films, this chapter focuses on the results and discussion of optical and electrical characterizations carried out on those hydrothermal ZnO films. We measure the transparency of the film in terms of percent transmittance and model the data as harmonic oscillators to extract values for absorption coefficient and refractive index. Hall effect measurements were conducted using the Van der Pauw method with processed test structures. Circular transmission line method was used to determine the contact resistance between ZnO and p-GaN. Most of the data presented here come from the same samples which were analyzed in the previous chapter.

3.2. Advantages of Hybrid Deposition of ZnO

Poor crystalline quality in conductive oxides can cause a reduction in carrier mobility because of increased point defects, grain boundaries, and lattice distortions. Therefore, it is desirable to deposit epitaxial films with a single crystallographic orientation and low degree of mosaicity. To achieve this, substrates need to be selected that such that they allow for heteroepitaxial growth.

These substrates must be composed of a material that contains crystallographic orientations with lattice parameters which can accommodate the growth of ZnO with minimal tensile or compressive stress. For ZnO, suitable substrates for epitaxial growth include materials such as crystalline Al2O3, GaN, AlN, SiO2, SiC, GaAs, and $MgAl_2O_4$. One major drawback to depositing a ZnO seed layer using the hydrothermal approach is that the only substrates on which it would be possible to grow off are those that share similar lattice parameters and crystal structures to that of ZnO, which only include GaN, ZnO, and $MgAl_2O_4$.

As shown in the previous chapter, depositing a ZnO seed layer using the hydrothermal approach makes it difficult to achieve reproducible results with high throughput. When evaluating dopants for ZnO it is essential to be able to quickly and reliably deposit films. One approach to achieving higher throughputs is to use an alternative deposition method for the seed layer. Due to reaction kinetics and thermodynamics, each deposition method can yield films of varying quality and growth rate. Techniques such as sputtering and ion beam deposition introduce high energy ions into the substrate, resulting in inferior quality electrical contacts. Selecting an appropriate deposition method for ZnO would depend on several factors such as desired properties and costs.

This multistep approach would allow one to leverage the advantages of the various deposition techniques to achieve specific film properties. For example, when deposited on p-type GaN as a transparent contact layer in a III-N device such

as a LED, the first deposition can use a technique that allows for a thin layer of epitaxial ZnO with high doping density which functions both a contact layer to the p-type GaN and as a seed layer for a thicker bulk layer of ZnO deposited using another technique. The seed layer would dictate the structure of subsequent layers by functioning as a template, allowing for a heteroepitaxial relationship to the underlying substrate.

For the experiments presented in this chapter, we used atomic layer deposition (ALD) to deposit our ZnO seed layers.

3.3. Experimental Methods

Film thickness was determined by surface profilometry measurements (Dektak 6M). Carrier type, concentration, mobility, and resistivity were determined at room temperature using a Hall effect system (Lakeshore 7504) with a maximum magnetic field of 6000 Gauss. Hall effect measurements were performed using the van der Pauw method on lithographically defined Greek cross type test patterns.[1] Mesas were etched using a dilute solution of o-phosphoric acid and acetic acid in DI water (1:1:50 /vol), ohmic metal contacts were composed of Ti/Au 20/200 nm. Four-point probe (CDE Resmap) was used to measure the resistivity of the film during the annealing studies. Before hall effect and four-point probe measurements, a UV-Vis-NIR spectrophotometer (Agilent Cary 500) was used to carry out normal incident transmission measurements on the ZnO thin films.

3.4. Electrical Characterization

Hall Effect Measurements

Hall effect measurements using the van Der Pauw method was extensively used to characterize the films we deposited. It provides a wealth of information regarding the electronic properties of thin film semiconductor. We can determine the type of semiconductor (n or p), the carrier density, carrier mobility, and the Hall coefficient of the films from these measurements. The conductivity of our ZnO thin films are given by,

$$\sigma_{ZnO} = \mu_e n + \mu_h p = \mu_e n \tag{3.1}$$

Where μ_e and μ_h are the mobilities ($cm^2V^{-1}s^{-1}$) of the negative and positive charge carriers and n and p are the densities of the electrons and holes (cm^{-3}). Since the hole concentration is negligible in ZnO, we can simplify the expression the product of the electron mobility and concentration. We use the Hall effect to decouple these two terms by introducing a magnetic field perpendicular to the film. When a current is passed perpendicular the magnetic field, a voltage is produced in the plane of the current and transverse to it. This voltage is caused by the deflection of charge carriers due to the applied magnetic field, (B_Z). To experimentally carry out this measurement would require the processing of a "Hall bar" with metal contacts wrapping the sidewalls of two ends of the bar. To simplify the device to be

measured the Van de Pauw method is used, and an appropriate test structure is processed into the films. We used a "Greek Cross" test structure, shown in **Figure 3.1**, to conduct our measurements.

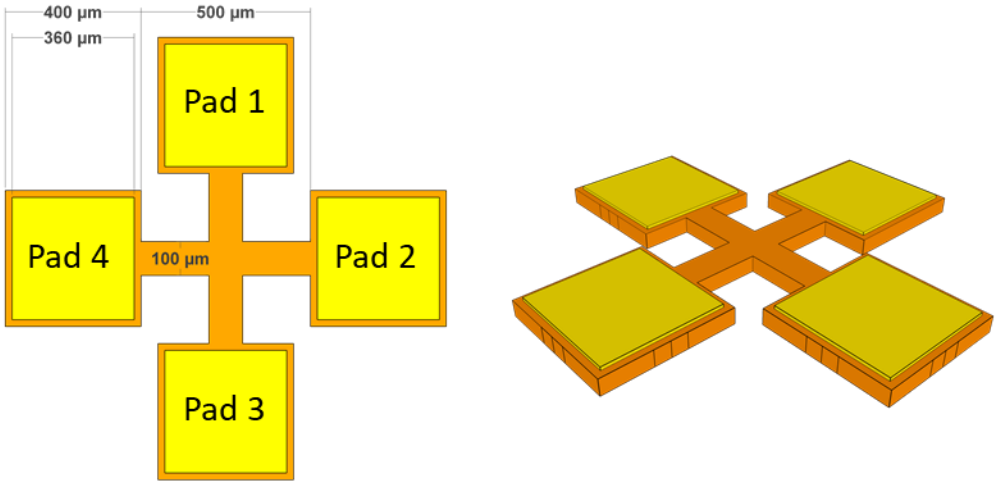

Figure 3.1 Greek cross test structure used for Hall effect measurements using the Van de Pauw method, yellow represent metal contact and orange represent the semiconductor to be measured

The Van de Pauw method calculated the hall voltage, V_H, of the material by passing a constant current between pads directly across from one another and measuring the voltage of the other two pads while the sample is under a positive magnetic field (P). All the possible permutations of this are run and repeated with a negative magnetic field(N). The Hall voltage is calculated by,

$$V_H = \left(\frac{V_{24} + V_{13} + V_{31} + V_{42}}{8}\right)_P - \left(\frac{V_{24} + V_{13} + V_{31} + V_{42}}{8}\right)_N \quad (3.2)$$

The sign of the Hall voltage indicates what the majority carriers are of the films (+ p-type – n-type). Once a hall voltage is obtained, a sheet carrier density, n_{sh}, can be calculated through,

$$n_{sh} = \frac{IB_Z}{e|V_H|} \quad (3.3)$$

where e represents the charge of an electron. Sheet carrier density (cm^{-2}) can be converted to bulk carrier density (cm^{-3}) by dividing by the film thickness, t (cm).

$$n = \frac{n_{sh}}{t} \quad (3.4)$$

The sheet resistance of the film, R_S (Ω/sq), is obtained from two measured characteristic resistances, R_A & R_B, by numerically solving the van der Pauw equation by iteration.

$$R_{21,34} = \frac{V_{34}}{I_{21}} \quad (3.5)$$

$$R_A = \frac{R_{21,34} + R_{12,43} + R_{43,12} + R_{34,21}}{4} \quad (3.6)$$

$$R_B = \frac{R_{32,41} + R_{23,14} + R_{14,23} + R_{41,32}}{4} \quad (3.7)$$

$$e^{-\frac{\pi R_A}{R_S}} + e^{-\frac{\pi R_B}{R_S}} = 1 \quad (3.8)$$

Finally, the mobility of the film can be calculated by,

$$\mu_e = \frac{1}{n_{sh} R_S e} \tag{3.9}$$

Conductivity, σ (S cm^{-1}), or resistivity, ρ (Ω cm), can be determined by the thickness and sheet resistance.

$$\rho = \frac{1}{\sigma} = R_S t \tag{3.10}$$

Results on Sapphire Substrates

Initial measurements were conducted on sapphire substrates on which 5 nm thick ZnO films were deposited via ALD and annealed at 500 °C for 10 min. The doped ZnO layers were formed hydrothermally. For this set of experiments dopants included unintentionally doped (UID) ZnO, group III elements Al, Ga, and In, as well as Li. Li is a group II element and may be an efficient donor dopant, in that it can donate up to 2 electrons to the conduction band of ZnO [2]. Preliminary work was conducted to determine the optimal hydrothermal layer anneal temperature. Samples were annealed at three different temperatures for 5 min, and their resistivity was determined using a four-point probe. **Figure 3.2** displays the results of the annealing study. The lowest resistivity was achieved when annealing at 250 °C, with Ga doped films having the lowest value of around 2 Ω cm. The highest resistivities were found for samples doped with Li or In.

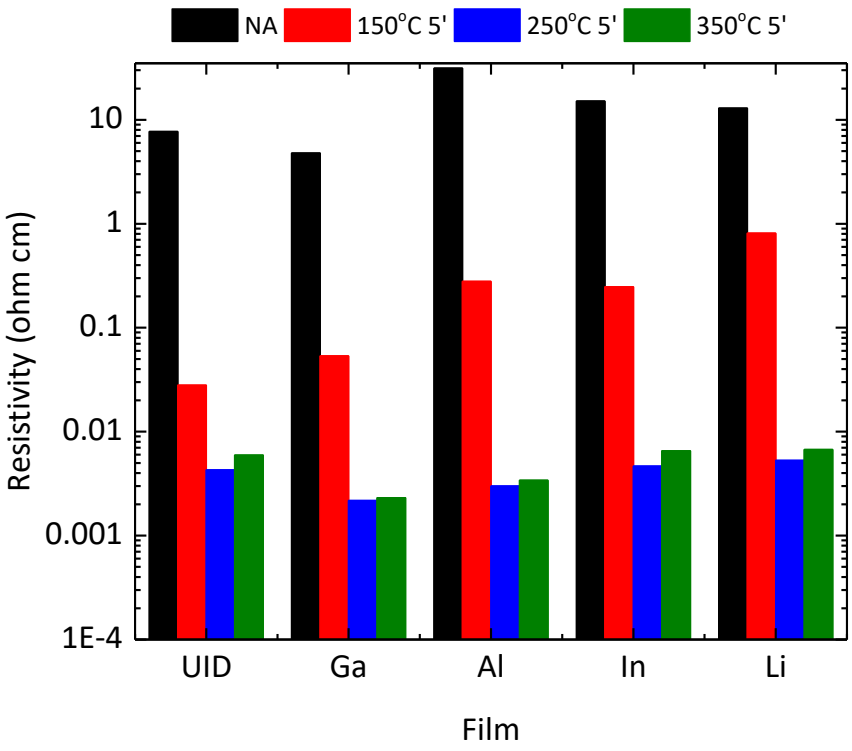

Figure 3.2 Resistivity of UID and doped ZnO films before and after annealing

Prior to annealing samples showed very high resistivities, the process of heating the films likely helps dehydrate any hydroxide phases to oxides. Hall measurements carried out on these films to probe their electronic properties. **Figure 3.3** shows the results of these measurements.

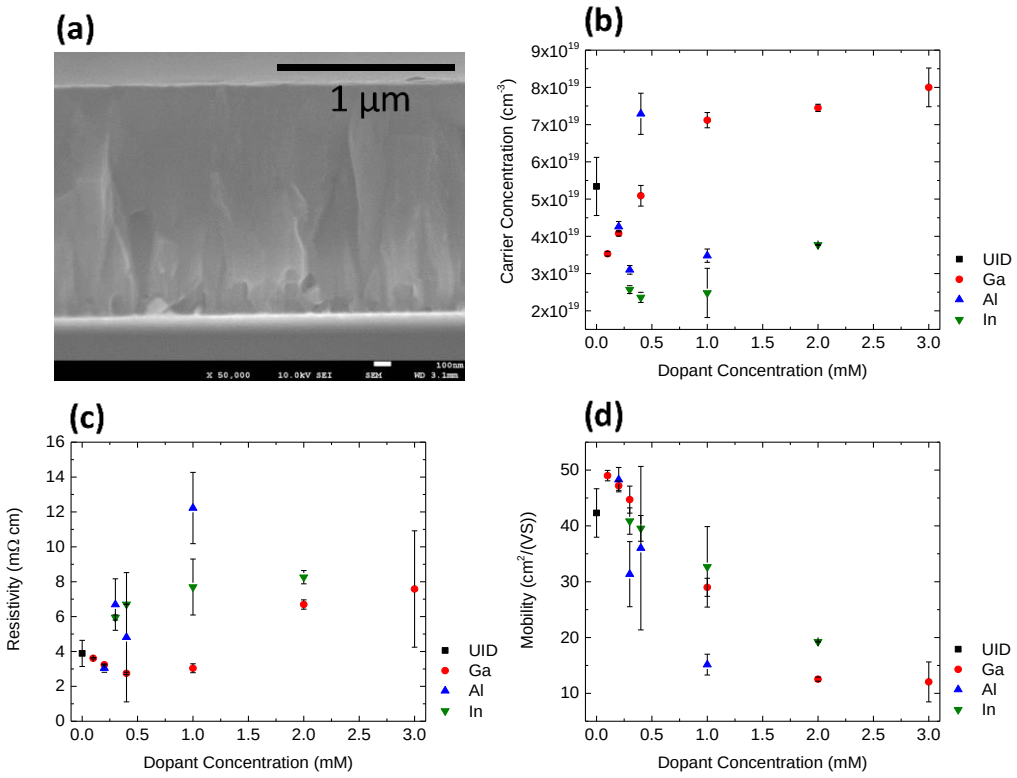

Figure 3.3 a) cross-sectional SEM micrograph of ALD/Hydrothermal ZnO film on a sapphire substrate b) carrier density vs. dopant concentration for doped ZnO films c) resistivity vs. dopant concentration for doped ZnO films d) mobility vs. dopant concentration for doped ZnO films

Figure 3.3a shows an example of the typical cross-sectional morphology of the films. **Figure 3.3**b indicates that the highest carrier density was found in Ga doped films of about $8x10^{18}$ cm^{-3}. This corresponded to low resistivity in the Ga doped films as well (~2.5 Ω cm), **Figure 3.3**c.

As can be expected, mobility dropped with increasing carrier density due to increased free carrier scattering. Highest mobilities were found for samples that

had the lowest dopant concentration. It should also be noted that increasing the nitrate salt concentration for the dopants studies made the films less hazy and also more likely to crack when annealed.

Results on Spinel Substrates

Electronic properties were investigated through Hall effect measurements using the Van de Pauw method. Test patterns were lithographically defined, and an example of one is shown in **Figure 3.4**a. Doping of ZnO crystals with group III metal cations under hydrothermal conditions results in the substitution of Zn-positions by group III metals and formation of the point defects of the In_{Zn}^{+} type point defect. Group III impurities when substituted on the Zn site act as shallow donors in ZnO. The extra valance electron of these impurities is loosely bound and exist in states near the CBM of ZnO allowing them to become ionized into the conduction band [3] easily. All films studied in this work exhibited n-type conductivity. Undoped ZnO typically exhibits n-type conductivity due to either hydrogen which can incorporate at high concentrations and behaves as a shallow donor or from the presence of crystallographic defects such as the presence of oxygen vacancies and or zinc interstitials [4]. Given its similar electronic properties to Zn, Ga doped ZnO thin films showed the greatest increase in carrier concentration, as seen in **Figure 3.4**b. In doped films showed the least carrier

concentration, possibly due to the presence of In hydroxide phases. Al-doped films also exhibited an increase in carrier concentration with increasing Al content, but not as significant as Ga doped films. Electron mobility generally decreased with the addition of impurity dopants, **Figure 3.4**c, but was less apparent of In-doped films. In and Zn share similar ionic radii which could limit carrier scattering from point defects formed by Zn substitutions. As shown in **Figure 3.4**d, Ga doped films exhibited the lower resistivities than In and Al-doped films, with the lowest being 1.9 mΩ cm. This is in line with experiments conducted on sputtered ZnO films with ion implanted Ga and is likely due to the similarities in electronegativity between it and Zn [5].

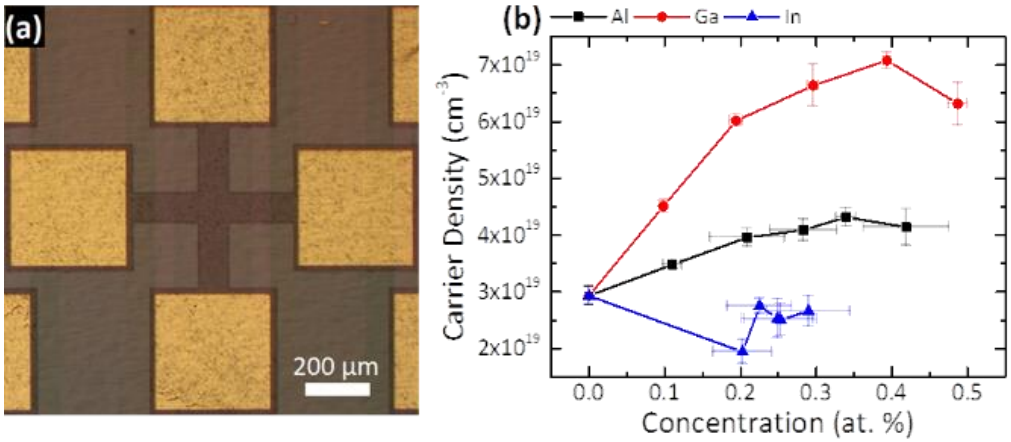

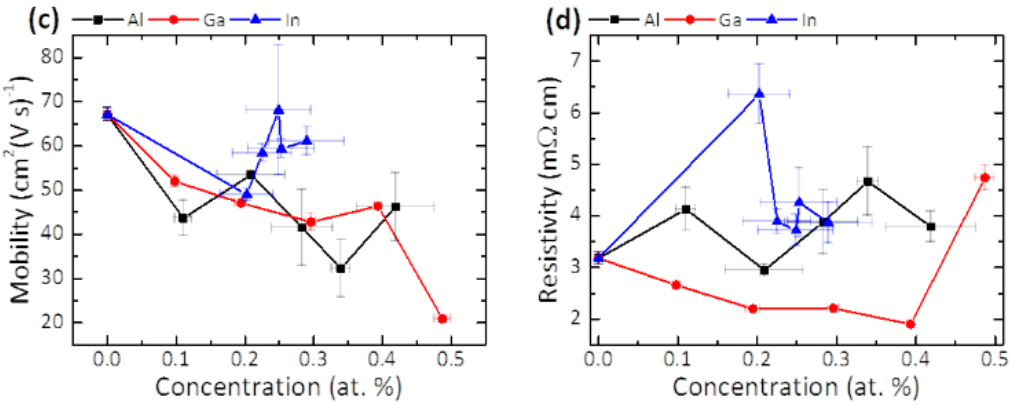

Figure 3.4 a) optical micrograph of a typical Greek cross hall test pattern used to determine b) carrier density, c) carrier mobility, and d) resistivity of doped hydrothermal ZnO thin films using Hall effect measurements

Temperature Dependent Hall Effect Measurements

Temperature-dependent Hall effect measurements provide one possible method to obtain donor and acceptor binding energies and mobilities. For non-degenerately doped semiconductors, the free carriers freeze out as the temperature is decreased. Since carrier concentrations have an Arrhenius dependence on temperature, binding energies can be obtained through determining from the slope of carrier concentration versus inverse temperature.

Preliminary measurements of hydrothermally grown ZnO films have been carried out using temperature dependent Hall measurements using Greek cross test structures, **Figure 3.5**a. Typical films morphologies are shown in **Figure 3.5**b. Room temperature values for resistivity carrier density and Hall mobility were

2.43E-3 Ω cm, 3.84E19 cm^{-3}, and 66 $cm^2V^{-1}S^{-1}$ respectively. **Figure 3.5**c, shows metallic conductivity, carrier concentration and mobility constant over temperature range measured. The significant fluctuations in mobility may be due to the porosity of the film. Resistivity versus temperature also trends as a degenerately doped semiconductor, **Figure 3.5**d.

In degenerately doped semiconductors, as is likely the case in our samples, the carriers have a kinetic energy orders of magnitude larger than the thermal energy. The kinetic energy of the carriers is given by the difference between the Fermi energy, and the eigenstate energy of the occupied sub-band. The thermal energy of the carriers is equal to 0.344 meV at a temperature of 4K. Even at 300K, the thermal energy is only equal to 25.9 meV which is much smaller than the kinetic energy of the carriers, which are on the order of 100 meV. In degenerate systems, the temperature independent Fermi velocity is much larger than the thermal velocity and the mobility is expected to remain constant throughout the temperature range as was evident in these films. Further control of the deposition process is required to produce non-degenerately doped films.

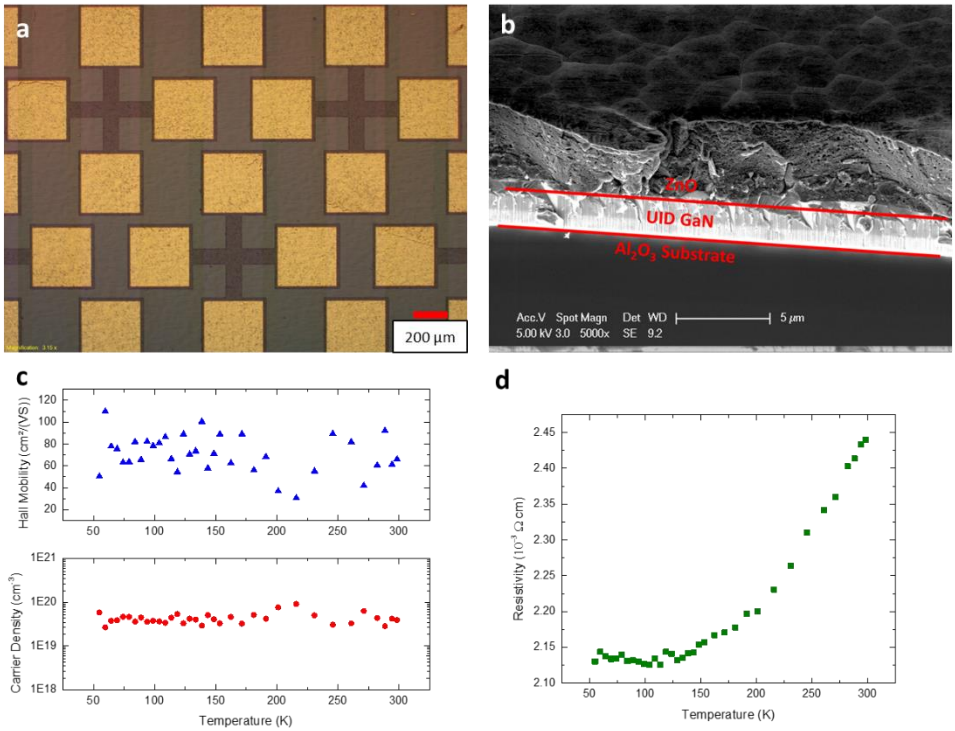

Figure 3.5 a) Greek Cross van de Pauw Hall test structures, b) 45deg tilted SEM micrograph of ZnO film on GaN template c) carrier density and hall mobility as a function of temperature d) Resistivity as a function of temperature

X-ray Photoelectron Spectroscopy

X-ray photoelectron spectroscopy (XPS) was carried out on doped films to elucidate further electronic and structural properties; it provides information on which chemical composition and bonding states present on the sample's surface. A Kratos Axis Ultra X-ray Photoelectron Spectroscopy system was used in these studies. XPS is a surface sensitive technique which can provide information on the elemental composition as well as chemical and electronic states of the first ~8 nm

of material. The detection limit for this technique is roughly 0.1 at% which corresponds to ~10^{19} cm^{-3}. Shown in **Figure 3.6** is a typical survey scan of UID hydrothermal ZnO. Surface contamination of carbon-containing impurities is evident by the C 1s peak; all other signals correspond to those from either Zn or O.

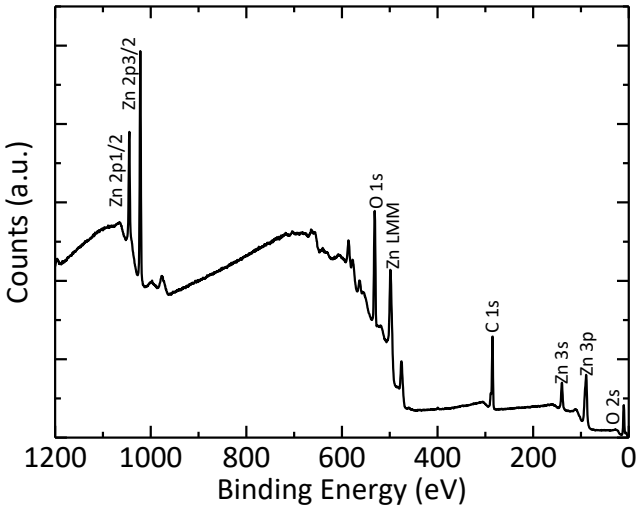

Figure 3.6 XPS survey scan of UID ZnO

XPS scans were also taken of 1mM Al, Ga, and In-doped ZnO films. The results of these scans are presented in **Figure 3.7**. Unfortunately, on the In-doped film exhibited dopant signals intense enough to analyze quantitatively. Peaks corresponding to In's 3d orbital was present in our scans. Ga doped films showed very weak signals from its 2p orbital, 2p 1/2 at 1114 eV and 2p 3/2 at 1117 eV. The Al-doped film did not exhibit any characteristic energy signals, such as the 2p at 74.4 eV and the 2s at 118 eV.

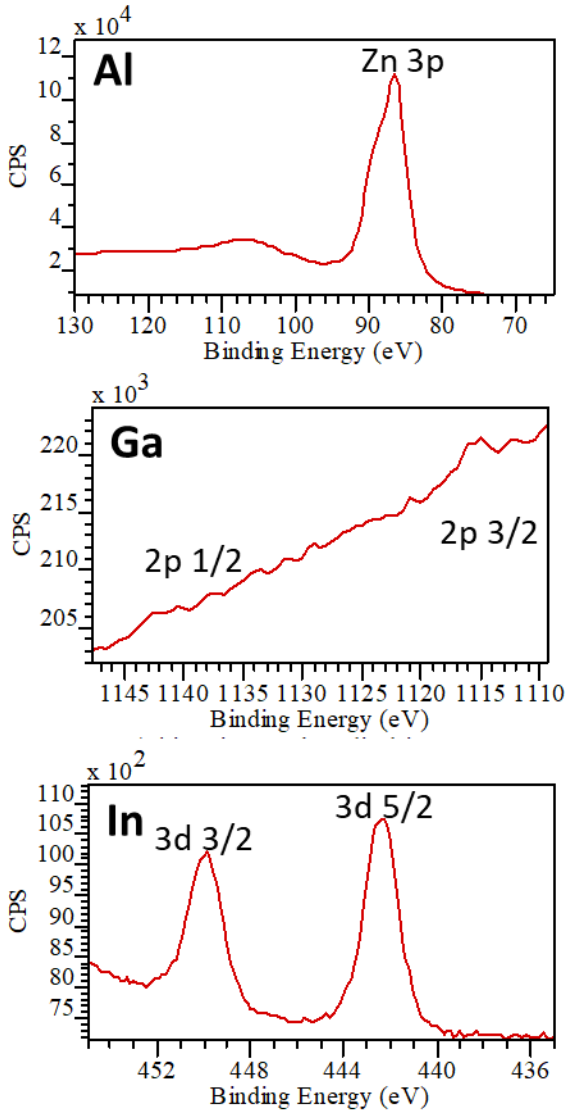

Figure 3.7 XPS scans of 1mM Al, Ga, and In-doped hydrothermal ZnO thin films

3.5. Circular Transmission Line Measurements

Circular transmission line method (CTLM) measurements were carried out between p-GaN and various materials including hydrothermal ZnO [6]. CTLM measurements allow one to determine the sheet resistance, R_S, of the underlying

material (p-GaN) and the transfer length, L_T, between the contacted and contacting materials. From those values, the contact resistance can be determined. The typical CTLM pattern used in most measurements is shown in **Figure 3.8**a. **Figure 3.8**b identifies that the inner radius is represented by r, and the gap spacing, g, is the distance between the inner and outer radius of the pattern. **Figure 3.8**c is a cross-sectional view of the pattern. The transfer length represents the distance at which the current density passing under the contacts drops to 1/e of the injected current density.

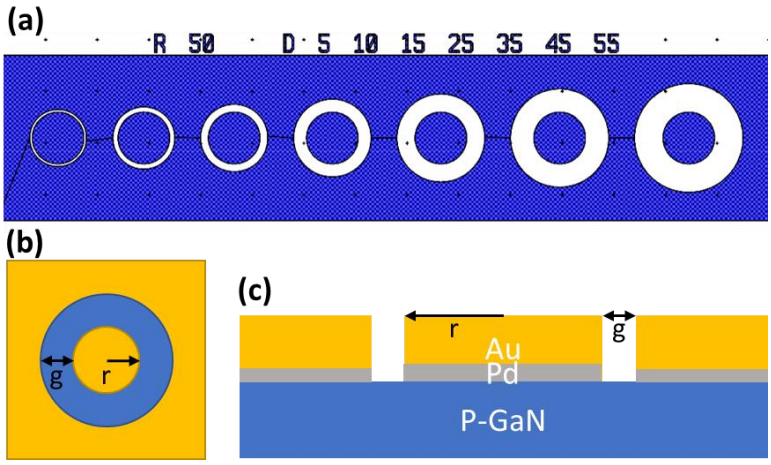

Figure 3.8 Schematic of CTLM pattern (a) full pattern on mask layout, (b) single gap spacing labeled, and (c) cross-sectional view of Pd/Au contact to p-GaN

Current-voltage measurements are taken between the inner circle and outer pattern. These IV curves were used to determine the total resistance, R_{CTLM}, for a given gap spacing. This resistance was measured for a set of gap spacings and fitted to the CTLM expression shown below.

$$R_{CTLM}(g) = \frac{\boldsymbol{R_{sh}}}{2\pi} \cdot \left[\frac{\boldsymbol{L_t}}{r} \cdot \frac{I_o\left(r/\boldsymbol{L_t}\right)}{I_1\left(r/\boldsymbol{L_t}\right)} + \frac{\boldsymbol{L_t}}{r+g} \cdot \frac{K_0\left(r+g/\boldsymbol{L_t}\right)}{K_1\left(r+g/\boldsymbol{L_t}\right)} + ln\left(\frac{r+g}{r}\right) \right] \quad (3.11)$$

Contact resistance is determined by the product of sheet resistance and transfer length squared, as shown by the equation below.

$$\rho_c = R_{sh}\, L_t^2 \quad (3.12)$$

The MATLAB code used to determine contact resistivities can be found in Appendix B. **Figure 3.9**a display typical ohmic IV curves for reference 20/200 nm Pd/Au contacts to p-GaN. Resistance values from there were then plotted as a function of gap spacing and fitted to equation 3.11, as shown in **Figure 3.9**b. CTLM analysis was carried out on several contacts including ITO, oxidized Ni/Au, and hydrothermal ZnO. The results are summarized in **Table 3.1**. Pd/Au and NiO/Au showed the lowest contact resistivities of 2 and 5 x10^{-3} **Ω** cm^2. ZnO films utilizing a hydrothermal seed layer showed the highest contact resistance of the set measured but was within the same order of magnitude as the rest.

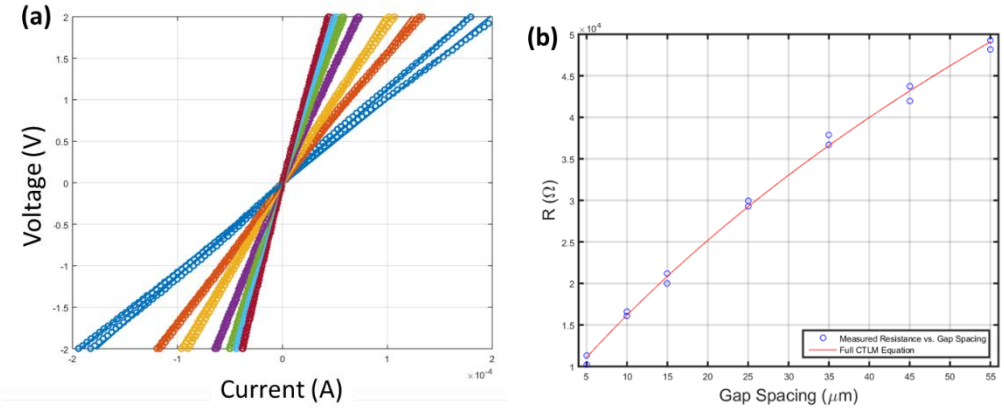

Figure 3.9 a) IV values for various gap spacings on CTLM test patterns of Pd/Au contacts on GaN LED epi, b) Total resistance vs. gap spacing with fitted CTLM equation

Table 3.1 CTLM analysis summary

Contact Material	R_S (kΩ/sq)	L_T (μm)	ρ_C (Ω cm^2)
Pd/Au (3/300 nm)	301	0.94	0.0027
ZnO (2000 nm)	331	1.42	0.0066
ITO (200 nm)	148	2.49	0.0092
NiO/Au (5/50 nm)	138	1.80	0.0045

Unfortunately, the CTLM patterns for ZnO films composed of an ALD seed layer did not exhibit completely ohmic IV characteristics and were not used for any devices. Metal contacts, such as Ti/Au or Cr/Al/Ni/Au, to either ITO or ZnO, exhibited low contact resistivities, on the order of 10^{-6} Ω cm^2. It was also found that metal contact to n-GaN can be improved by using $SiCl_4$ based RIE etches when isolating mesa structures.

3.6. Optical Characterization

Weakly Absorbing Films

Transparent conductive films such as TCOs have several characteristic features in the transmittance spectra. At wavelengths corresponding to energies above the bandgap of the material, interband transitions absorb a majority of the light. Above the bandgap, light can pass through with minimal absorption until it approaches energies corresponding to free carrier resonances. The free carriers responsible for conductivity also absorb in the infrared and far infrared spectrum as seen in Figure 3.10 [7].

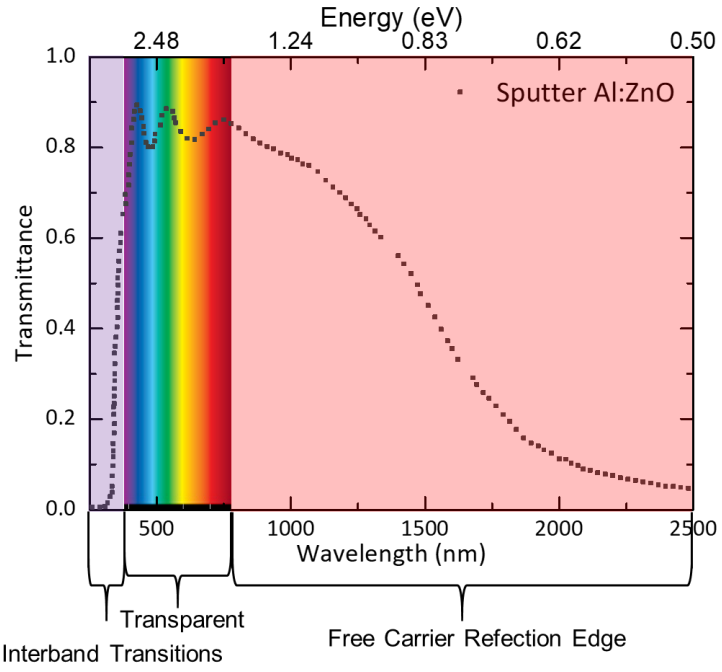

Figure 3.10 Transmittance spectra of sputtered Al-doped ZnO

Given that transparent current spreading thin films are highly transparent across the visible wavelength spectrum, developing a method for measuring optical absorbance is non-trivial. Optical absorbance, α (cm^{-1}), is defined by the Beer-Lambert law,

$$I = I_0 e^{-\alpha x} \tag{3.13}$$

Where I and I_0 are the transmitted and initial optical power respectively and x is distance. A straightforward way to understand this absorbance is that its inverse represents the distance at which the initial optical transmittance drops to 1/e (~37%) of the original value. So, for example, if ITO (n~2) has an absorption coefficient of 2000 cm^{-1} at 450 nm, it means that a 5 μm thick film in the air (n=1) will transmit 37% of the initial normal incident light. Fresnel reflectance due to refractive index contrasts must also be accounted for in an actual transmittance measurement. For normal incidence it is,

$$R = \left|\frac{n_1 - n_2}{n_1 + n_2}\right|^2 \tag{3.14}$$

For our ITO film, this amounts to 22 % loss due to Fresnel reflections. This is the case all film thicknesses until the film thickness is much less than the wavelength of light passing through. Actual ITO films on LEDs are much thinner than 5 μm (~100 nm), and loss due to absorption is much lower.

The simple expression of absorbance A=1-T-R, where T and R are transmittance and reflectance respectively, cannot give a reliable result. Errors inherent in the measurement and nonuniformities in film thickness can lead to negative absorbance values which do not have physical meaning. The approach we took was to model the transmittance spectrum using a harmonic oscillator.

Optical Transmittance

Normal incidence transmittance spectra of unannealed films, **Figure 3.11**, show that Ga and Al-doped ZnO form smooth transparent films. Fabry-Perot resonance modes are indicated by the oscillations found in these spectra, indicating that both the top and bottom surfaces of the films are smooth. In-doped films were hazy to the eye and did not exhibit very pronounced resonance modes, indicating that they were not as smooth. AFM analysis of these films, discussed in the previous chapter, confirm this. The absorption tail around 375 nm is indicative of ZnO and will be discussed in detail later in this section. Another feature of interest is the absorption in the NIR to IR range. Ga doped films showed the most absorption in this range, which is indicative of free carrier absorption. Ga doped films also contained the highest concentration of free carriers. 300 nm ITO films, not shown, showed similar transmittance characteristics, but much larger free carrier absorption in the NIR and IR. This corresponds to their much lower resistivity values when compared with UID and doped ZnO.

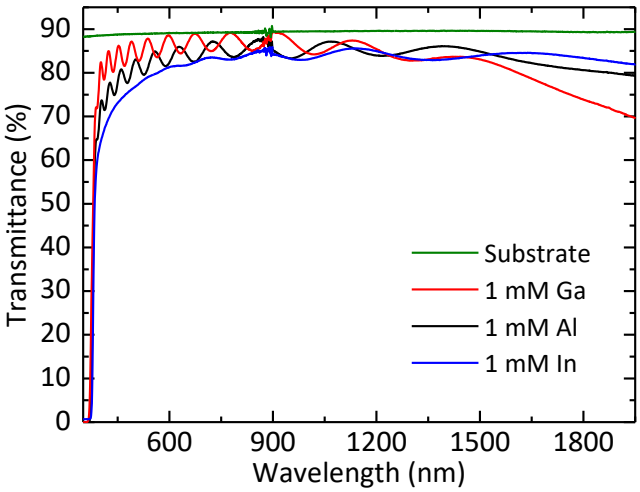

Figure 3.11 Normal incidence transmittance spectra of group III doped ZnO films on spinel substrates

UV-Vis transmittance spectra of annealed ZnO films are shown in **Figure 3.12**. Transparent films also exhibited Fabry-Perot resonance modes due to smooth interfaces and uniform film composition. Many of the low doped films did not exhibit resonance modes due to the formation of pores within the film during the annealing stage. The presence of porosity diffuse the transmitted light, reducing normalized light transmittance intensity.

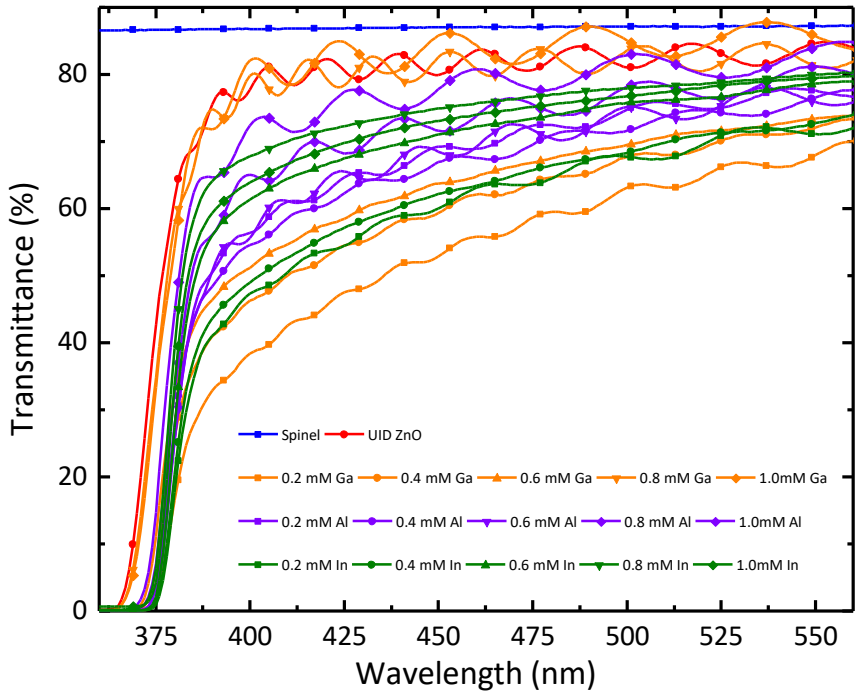

Figure 3.12 UV-Vis transmittance spectra of doped ZnO films after 300 °C anneal

Modelling

Optical properties of these films, such as extinction coefficient and refractive index, were extracted from UV-Vis-NIR transmittance spectra taken before the films were annealed. This was accomplished by preparing a model of the complex dielectric permittivity and using it to generate a theoretical transmittance spectrum and iteratively adjusting the parameters of the model till a suitable fit to the experimental data is achieved. For our analysis, we chose to model our films as Cody-Lorentz oscillator [7]. The spinel substrate was also modeled as a Cody-Lorentz oscillator, and the analysis was carried out using CompleteEASE fitting

software by J.A. Woollam Co. **Figure 3.13**a shows an example of a UID ZnO film that was fitted to this model. The refractive index and extinction coefficients calculated from the model can be seen in **Figure 3.13**b, additional details regarding optical modeling are available in the supplementary section.

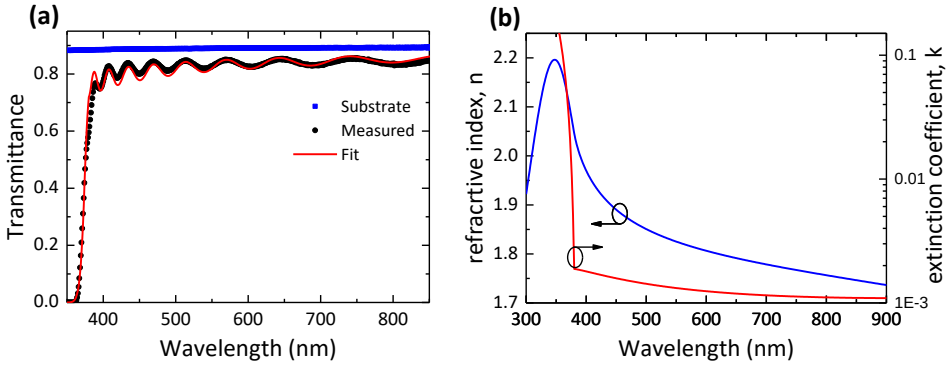

Figure 3.13 a) Optical transmittance spectrum of spinel substrate (blue) and UID ZnO thin film (black) along with the fitted *Cody*-Lorentz oscillator model (red) b) Refractive index and extinction coefficient values determined using the fitted model

Table 3.2 summarizes the absorption coefficient and refractive index for the films with the lowest measured resistivities in each dopant set. The undoped case showed the lowest absorption due to the absence of charged impurities. The lowest resistivity Ga films also showed the lowest absorption coefficient compared to Al or In-doped films. The high optical absorbance of In-containing ZnO thin films may be due to the same issues which give it poor electronic properties. Additionally, several of the low doped films became hazy after the annealing step due to the formation of pores [8]. This was not the case in Ga films and highly

doped Al films. The presence of porosity in the films would lower the films refractive index as well since the total index would become a composite between air (n=1) and ZnO (n~2). A more in-depth analysis of the optical properties of doped ZnO thin films has been carried out in an earlier work [9].

Table 3.2 Absorption coefficients and refractive indices for select ZnO thin films

Sample	Absorption Coefficient, α [cm^{-1}]	Refractive Index, n @ 450nm
0.00 at. %	389	1.91
0.40 at. % Ga	441	1.90
0.21 at. % Al	523	1.92
0.25 at. % In	1023	1.91

The most transparent and conductive films in this set were used to determine the refractive index and extinction coefficients. This was carried out by fitting the transmittance spectra to a model for the real ε_1 and imaginary parts ε_2 of the dielectric constant ε_{CL}. **Table 3.3** summarizes the values for the fitted parameters used in this model.

Table 3.3 Fitting parameters used for UID ZnO and Spinel

Material	Parameter	Value (eV)	Material	Parameter	Value (eV)
Spinel	Amp	57.414	**UID ZnO**	Amp	15.762
	Br	4.099		Br	1.723
	E0	7.777		E0	3.240
	Eg	6.075		Eg	4.146

	Ep	5.572		Ep	0.833
	Et	0		Et	0.0243
	Eu	0.5		Eu	1.201

$$\varepsilon_{CL} = \varepsilon_1 + i\varepsilon_2 \tag{3.15}$$

A Cody-Lorentz oscillator function was used to determine the refractive index and absorption coefficient of the doped ZnO films. The Cody-Lorentz oscillator defines a bandgap energy Eg, and a Lorentzian absorption peak (parameters A, Eo, and Br), with the dielectric constant ε being proportional to $(E\text{-}Eg)^2$ in the region just above Eg. It also defines two transitions (Et and Ep) from Lorentzian to Cody behavior. Ep is where absorption transitions from Lorentzian to Cody behavior, and Et is where the absorption transitions from Cody to Urbach behavior. The Kramers-Kronig integral is solved analytically with CompleteEASE.

$$\varepsilon_1 = \frac{2}{\pi} P \int_0^{\infty} \frac{\xi \varepsilon_2(\xi)}{\xi^2 - E^2} d\xi \tag{3.16}$$

$$\varepsilon_2(E) = \frac{E_1}{E} exp\left(\frac{E - E_g - E_t}{E_u}\right) \quad for \;\; 0 < E \leq \left(E_g + E_t\right) \tag{3.17}$$

$$\varepsilon_2(E) = G(E) \cdot L(E) \quad for \;\; E > \left(E_g + E_t\right) \tag{3.18}$$

G(E) is the near-bandgap function. It defines the Cody absorption behavior.

$$G(E) = \frac{\left(E - E_g\right)^2}{\left(E - E_g\right)^2 + E_p^2} \tag{3.19}$$

L(E) is the Lorentz oscillator function.

$$L(E) = \frac{AE_0\Gamma E}{(E^2 - E_0^2)^2 + \Gamma^2 E^2} \tag{3.20}$$

Finally, refractive index n and extinction coefficient k can be determined.

$$(n + i\kappa)^2 = \varepsilon_1 + i\varepsilon_2 \tag{3.21}$$

Absorption coefficient, α, can then be calculated, with λ being wavelength.

$$\alpha = \frac{4\pi\kappa}{\lambda} \tag{3.22}$$

A comparison between the optical properties of Ga:ZnO and ITO derived from models of transmittance spectra are provided in **Table 3.4.**

Table 3.4 Summary of optical properties of Ga:ZnO and ITO

	Ga:ZnO	ITO
Thickness	**1.30 µm**	**0.33 µm**
Transmittance	**80.02 %**	**80.68 %**
Refractive Index	**1.9**	**2.1**
Ext. Coeff.	**4.85×10^{-3}**	**1.58×10^{-3}**
Abs. Coeff. @ 450nm	**441.54**	**1355.60**

Optical Bandgap

Determining optical bandgap of a semiconductor is important when trying to evaluate the effect dopants have on the optical properties of the films. Converting transmittance spectra to Tauc plots[10] provides a simple way to determine this value. To produce a Tauc plot one simply needs to convert wavelengths (nm) into energy, hυ (eV), and convert transmittance to absorption coefficient by,

$$\alpha = -\frac{lnT}{t} \tag{3.23}$$

which is valid near the band edge of the transparent semiconductor. Plot $(\alpha h\upsilon)^2$ vs. hυ and extrapolate the linear region of the graph to the x-intercept to determine optical bandgap.

UV-Vis-NIR transmission spectra were taken of the same set of samples and were used to determine their optical bandgap. $(\alpha h\nu)^2$ vs. hνTauc plots[10], [11] were calculated from these spectra, and the linear portion of the absorption edge was extrapolated to the energy axis, as shown in **Figure 3.14**a for a UID ZnO film. Optical bandgap of ZnO is typically measured to be 3.3eV [12]. As seen in **Figure 3.14**b, the optical bandgap of ZnO can be substantially influenced by the addition of dopants in the hydrothermal growth solution, ranging from 3.28 to 3.39 eV depending on the type and concertation of dopants.

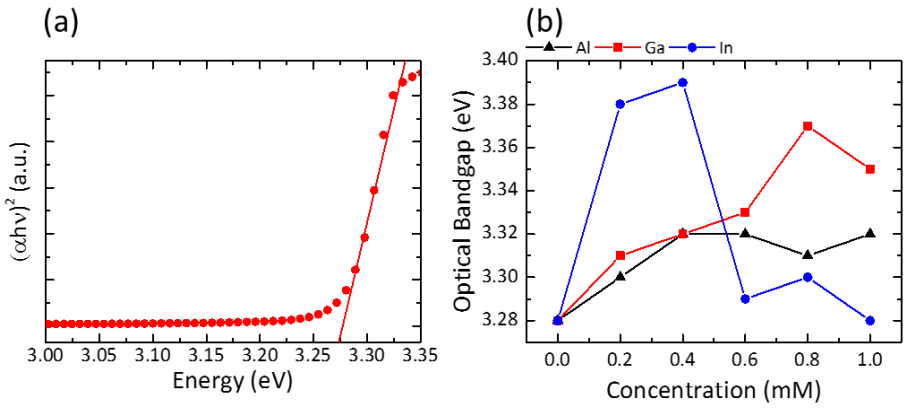

Figure 3.14 (a) Tauc plot for UID ZnO (b) optical bandgap for doped ZnO films

For Ga and Al-doped films, there was a general broadening of the optical bandgap, likely due to the Burstein-Moss effect [13]. As the addition of dopants increases the materials carrier density, the Fermi level enters into the conduction band affecting band gap absorption by forcing excited carriers to go into states above the Fermi level, see **Figure 3.15**.

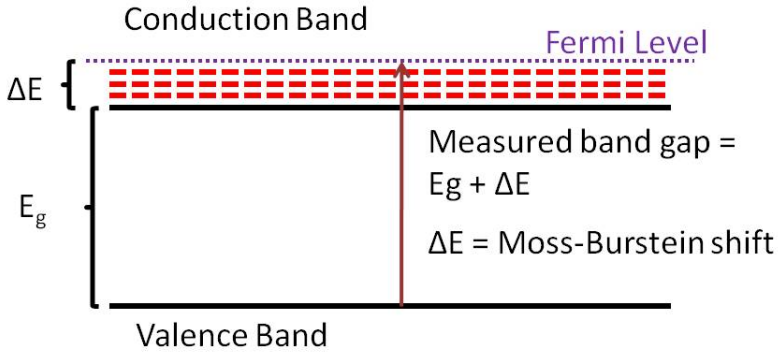

Figure 3.15 Schematic representation of the Moss-Burstein effect in semiconductors

Carrier scattering may also play a part in this change in the optical bandgap. Microstructural defects, ionized impurities, and lattice strain can all influence the absorption band edge of the film. In the case of In-doped films, the addition of greater concentrations of dopants in solution does not result in a broadening of the optical band gap after 0.4 mM. This is likely due to issues with the incorporation of In in the films and the conversion of $In(OH)_3$ into In_2O_3.

The optical bandgap of ZnO is also affected by the annealing step that is required to make the films conductive as displayed in Figure 3.16. As shown

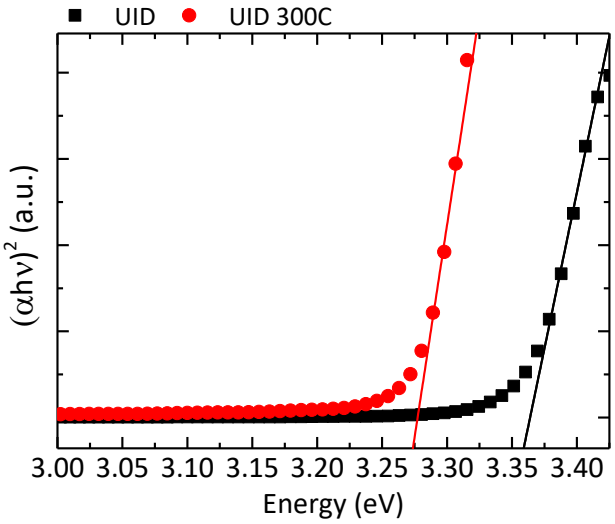

in

Figure 3.16 Tauc plots of UID ZnO before and after annealing

Table 3.5, the films bandgap tends to reduce slightly after annealing. This effect is less prevalent in doped ZnO films so that it may be due to the presence of porosity in the films. The formation of pores the in the films is due to an increase

in density of the film by the dehydration reaction that converts $Zn(OH)_2$ to ZnO while the volume remains similar.

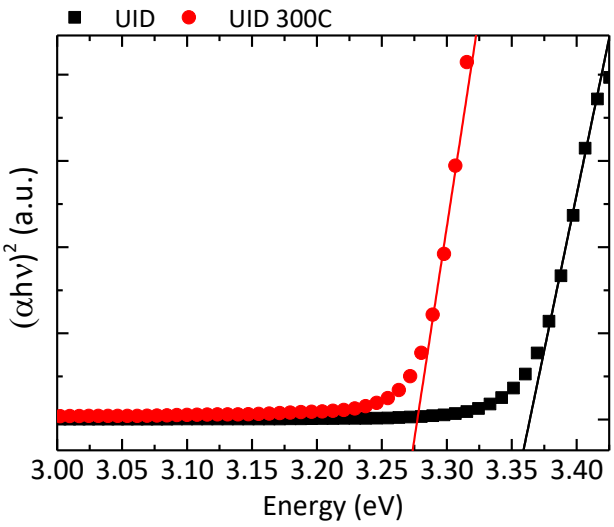

Figure 3.16 Tauc plots of UID ZnO before and after annealing

Table 3.5 Optical Bandgap of ZnO films before and after annealing at 300 °C for 5 min

Sample	E_g (eV) Before Anneal	E_g (eV) After Anneal
UID	3.36	3.28
Al	3.38-3.40	3.3-3.32
Ga	3.38-3.39	3.31-3.35
In	3.38-3.39	3.38-3.28

3.7. Conclusions

In summary, we have shown that group III doped hydrothermal ZnO thin films exhibit a range of electrical and optical properties. Low electrical resistivity was present in undoped films. The presence of these impurity dopants in the films can both enhance conductivity and transparency, as is the case for Ga and Al, or hinder it, in the case of In. The next chapter will focus on using n-GaN as a homoepitaxial current spreading layer.

3.8. References

[1] D. K. Schroder, *Semiconductor Material and Device Characterization*. Hoboken, NJ, USA: John Wiley & Sons, Inc., 2005.

[2] L. N. Demianets and D. V Kostomarov, "Mechanism of zinc oxide single crystal growth under hydrothermal conditions," *Ann. Chim. Sci. des Matériaux*, vol. 26, no. 1, pp. 193–198, 2001.

[3] A. Janotti and C. G. Van de Walle, "Fundamentals of zinc oxide as a semiconductor," *Reports Prog. Phys.*, vol. 72, no. 12, p. 126501, Dec. 2009.

[4] C. G. Van De Walle, "Hydrogen as a cause of doping in zinc oxide," *Phys. Rev. Lett.*, vol. 85, no. 1, pp. 1012–1015, 2000.

[5] S. Kohiki, M. Nishitani, and T. Wada, "Enhanced electrical conductivity of zinc oxide thin films by ion implantation of gallium, aluminum, and boron atoms," *J. Appl. Phys.*, vol. 75, no. 4, pp. 2069–2072, 1994.

[6] G. Reeves, "Specific contact resistance using a circular transmission line model," *Solid. State. Electron.*, no. x, pp. 1–4, 1980.

[7] R. E. Treharne, K. Hutchings, D. a Lamb, S. J. C. Irvine, D. Lane, and K. Durose, "Combinatorial optimization of Al-doped ZnO films for thin-film photovoltaics," *J. Phys. D. Appl. Phys.*, vol. 45, no. 33, p. 335102, Aug. 2012.

[8] A. Escobedo Morales, M. Herrera Zaldivar, and U. Pal, "Indium doping in nanostructured ZnO through low-temperature hydrothermal process," *Opt. Mater. (Amst).*, vol. 29, no. 1, pp. 100–104, 2006.

[9] A. J. Mughal, B. Carberry, J. S. Speck, S. Nakamura, and S. P. DenBaars, "Structural and Optical Properties of Group III Doped Hydrothermal ZnO Thin Films," *J. Electron. Mater.*, vol. 46, no. 3, pp. 1821–1825, Mar. 2017.

[10] J. Tauc, R. Grigorovici, and A. Vancu, "Optical Properties and Electronic Structure of Amorphous Germanium," *Phys. Status Solidi B*, vol. 15, no. 2, pp. 627–637, 1966.

[11] B. D. Viezbicke, S. Patel, B. E. Davis, and D. P. Birnie, "Evaluation of the Tauc method for optical absorption edge determination: ZnO thin films as a model system," *Phys. status solidi*, vol. 252, no. 8, pp. 1700–1710, Aug. 2015.

[12] V. Srikant and D. R. Clarke, "On the optical band gap of zinc oxide," *J. Appl. Phys.*, vol. 83, no. 10, p. 5447, 1998.

[13] E. Burstein, "Anomalous optical absorption limit in InSb [4]," *Phys. Rev.*, vol. 93, no. 3, pp. 632–633, 1954.

Chapter 4. MBE GaN Tunnel Junctions

4.1. Introduction

III-nitride semiconductors have seen high demand in optoelectronics and power electronic applications, due to the ability to alloy In, Ga, and Al nitrides and achieve a broad range of bandgaps and heterostructures. However, several material growth and device design challenges remain. For example, due to the high resistivity of p-type GaN (p-GaN), III-nitride-based optoelectronic devices typically require a transparent current spreading electrode to operate efficiently. Transparent conductive oxides (TCOs) such as n-type Sn-doped In_2O_3 (ITO) [1] or Ga doped ZnO [2,3] are typically employed as an ohmic current spreading contacts to p-GaN. They function as Esaki tunnel diodes under reverse bias [4] by allowing electrons to tunnel between the conduction band of the TCO and the valence band in the p-GaN at the junction interface when placed under reverse bias. Although TCOs are widely used, they suffer from high optical absorbance and limit the design possibilities of III-nitrides based optoelectronic devices.

An alternative approach to TCOs which has recently become the focus of intense interest is to use highly doped n-type GaN (n-GaN) layers as the current spreading contact [5–7]. This approach enables the design of buried contacts to form monolithically integrated LEDs that can overcome issues such as efficiency

droop [8,9]. One approach to achieving low-resistance ohmic contact, and thereby lowering operating voltage is through bandgap engineering. Small band gap semiconductors can promote the thermionic emission of carriers. Thus thin, heavily doped capping layers of small band gap semiconductors can be applied to various devices to obtain low contact resistance. InN, having a lower band gap than GaN and AlN, can produce a lower contact resistance when a layer of InN or InGaN is grown on GaN [20]. This has been shown to work for p-InGaN capping layers on p-GaN due to strong band bending in the InGaN induced by polarization fields [22].

In this work, we utilized a hybrid approach to creating TJ contacts by depositing epitaxial layers of Si-doped n-GaN grown by MBE onto p^+GaN and p^+InGaN material grown by MOCVD to determine the effect of incorporating of an InGaN layer and varying the Si concentration has on reducing excess voltages in our devices. Additionally, we compare the performance of InGaN based blue LEDs which contain varying concentrations of Si at the TJ regrowth interface.

4.2. Properties of GaN Tunnel Junction Contacts

Effective tunneling junctions (TJs) require that there be a high donor, N_d, and acceptor concentrations, N_a, at the junction interface to minimize the depletion width, equation (4.1) where ε is the permittivity of free space and q is the electron charge.

$$w = \sqrt{\frac{2\varepsilon}{q}\left(\frac{1}{N_A}+\frac{1}{N_D}\right)(V_{bi}-V)} \tag{4.1}$$

Additionally, the depletion width can be further reduced by minimizing the built-in potential of the diode, V_{bi}, which can be achieved by increasing the intrinsic carrier concentration, $n_{i,}$ by lowering the bandgap, E_g, at the interface, equations (4.2) and (4.3) where T is temperature N_c and N_v are the effective density of states of the conduction band and valence band respectively [10].

$$V_{bi} = \frac{kT}{q}\ln\left(\frac{N_D N_A}{n_i^2}\right) \tag{4.2}$$

$$n_i = \sqrt{N_C N_V}\, e^{-\frac{E_g}{2kT}} \tag{4.3}$$

This can be achieved utilizing a lower bandgap material such as InGaN in place of GaN. [11] In addition, including an InGaN layer takes advantage of strong piezoelectric and spontaneous polarization fields found in III-nitrides systems. The large electric fields at the heterointerfaces result in large band bending, further increasing tunneling probability [12]. Growing these types of junctions using metal organic chemical vapor deposition (MOCVD) is quite challenging due to issues such as the Mg memory effect resulting in significant amount of the p-dopant Mg incorporating into the subsequent n-type Si-doped GaN layers [13]. In addition, ambient hydrogen in the MOCVD reactor can re-passivated previously activated Mg [14] with the addition of Si-doped n-GaN behaving as a diffusion barrier when

attempting to reactivate the p-GaN [15]. One solution to this is to deposit the n-type GaN layer using an alternative deposition tool such as molecular beam epitaxy (MBE), which utilizes lower temperatures and contains much less ambient hydrogen. This technique has been successfully demonstrated on edge emitting laser diodes, [16] vertical-cavity-surface-emitting lasers (VCSELs), [17] and LEDs [18]. However, higher series resistance and operating voltage were realized in these devices when compared with more conventional contact materials, such as ITO.

4.3. Experimental Methods

MOCVD Growth of p-n Diodes

An atmospheric MOCVD reactor was used to grow GaN p-n diodes structures. Figure 1(a) and (b) show schematic illustrations of the epitaxial structures grown on single side polished sapphire substrates with their respective thicknesses and dopant concentrations. For these experiments, two types of highly doped p-type capping layers were utilized with one being a highly doped 12 nm p^+GaN layer with a Mg concentration of $9x10^{19}$ cm^{-3} and the other being a 5 nm p^+InGaN layer containing 15% In and a 7 nm p^+ GaN layer with a similar Mg concentration. A schematic representation of the structures is presented in **Figure 2.1**. Before MBE regrowth, the samples were activated in air at 600 °C for 15 min and dipped in buffered HF for 1 min to remove excess surface Mg. [19] For the LED samples

studied, commercially available InGaN blue (445nm) LED wafers from Powerway Advanced Material Co. were used, and they were also dipped in buffered HF before regrowth.

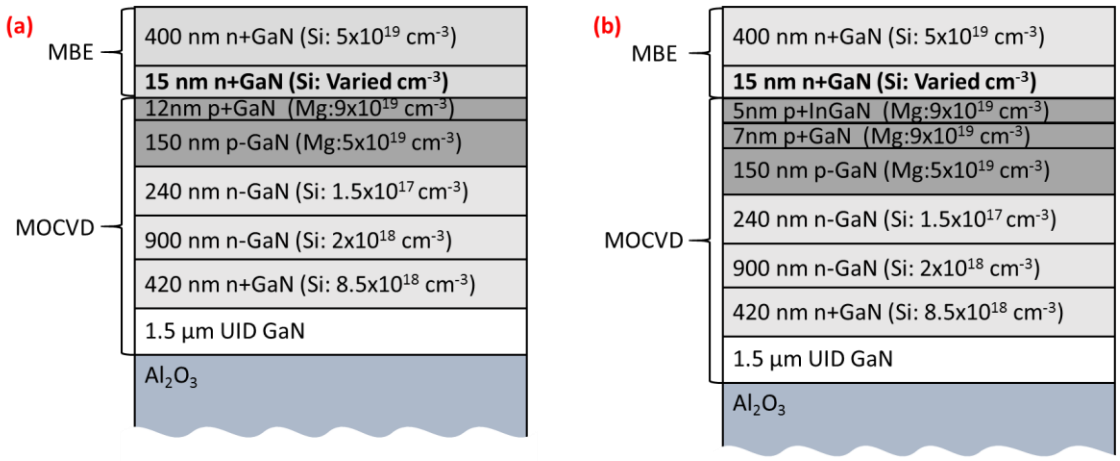

Figure 4.1 Schematic of the GaN p-n diode test structure with (a) p^+GaN and (b) p^+InGaN capping layer

MBE Deposition of n^+GaN

The p-n diode and LED samples were then loaded into a Veeco 930 NH_3 MBE tool, and outgassed at 400 °C for 1 hour prior to regrowth. The n-type GaN regrowths were performed at 700 °C using solid source effusion cells for gallium and silicon and NH_3 flow rate of 200 sccm. The silicon concentration in the n^{++}GaN:Si layers was varied by reducing the Ga flux incident during growth. The beam equivalent pressures of the Ga fluxes used were $1x10^{-7}$, $6x10^{-8}$, $4x10^{-8}$ and

$2x10^{-8}$ torr, corresponding to Si concentrations 1-4 respectively as listed in Table 2.1. The Si concentration in the tunnel junction samples was measured by secondary ion mass spectrometry (SIMS) in a Cameca IMF 7f system.

Device Processing

Mesa structures were etched into the p-n diodes and LED structures to expose the n^+ GaN contact layers. After the mesa etches, common, Ti/Al/Ni/Au contacts were deposited on both the bottom MOCVD and top MBE n^+ GaN layers for both diode and LED devices. Current-voltage measurements were carried out on diodes with a radius of 100 μm using a four-point probe configuration. For the LEDs, light output power, current, and voltage (LIV) were measured for the processed LEDs on the wafer. Both the p-n diodes and LEDs with MBE TJ contacts were subjected to a burn-in current of 300 A/cm^2 for 5 seconds to anneal the contacts.

4.4. Results and Discussion

Figure 4.2 shows the SIMs depth profile for the MBE calibration sample in which the Ga flux was varied to modulate the Si concentrations. AlGaN marker layers were introduced to distinguish layers with differing Ga flux. It can be seen that the Ga intensity reduces and Si concentration increases as we profile deeper into the film. This corresponds to a decrease in Ga flux incident on the film. The deposition conditions for this calibration sample were used during depositions on p-n diodes and InGaN LEDs. The average value of the Si concentrations for all

four cases was used in subsequent analysis and simulations.

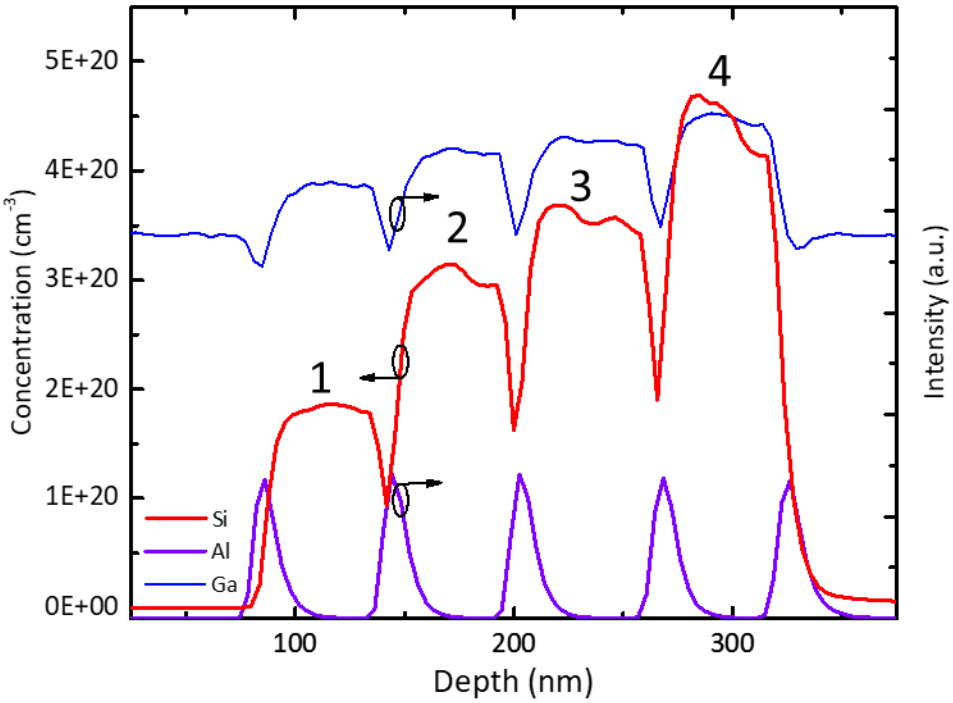

Figure 4.2 SIMS depth profile of a Si calibration sample

Table 2.1 shows the Si concentrations in the n+ side of the TJ for the samples in this study. All subsequent figures refer to sample numbers listed in this table. The band structure for the various junction conditions in this study was modeled using the SiLENSe software package. The quasi-fermi levels for electrons and holes are plotted in **Figure 4.3** for a TJ contact with a p-InGaN layer. The Fermi level on the p-side does not go below the valence band under a reverse bias of 0.5V, while on the n side it does go slightly past the conduction band.

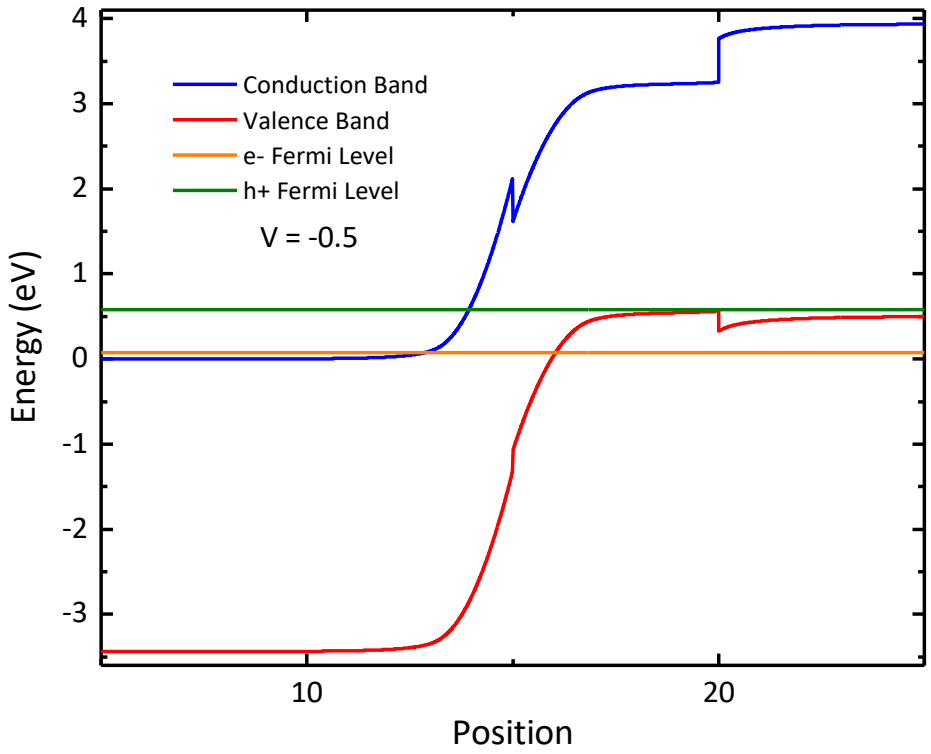

Figure 4.3 Simulated junctions are under reverse bias

Table 4.1 Summary of measured Si concentrations and Specific series resistances for the p-n diodes with TJ contacts as well as a reference Pd/Au contact

Sample #	Contact Layer Si Concentration (cm^{-3})	Specific Series Resistance p^+GaN ($\Omega\ cm^2$)	Specific Series Resistance p^+InGaN ($\Omega\ cm^2$)
1	1.86×10^{20} cm^{-3}	4.17×10^{-3}	3.73×10^{-3}
2	3.15×10^{20} cm^{-3}	4.17×10^{-3}	4.00×10^{-3}
3	3.65×10^{20} cm^{-3}	4.36×10^{-3}	4.01×10^{-3}
4	4.61×10^{20} cm^{-3}	3.75×10^{-3}	3.42×10^{-3}
ref	Pd/Au	1.97×10^{-3}	1.36×10^{-3}

Figure 4.4 shows one-dimensional simulations of the band structure of the tunnel

junction contacts at 300 K. The values for acceptor and donor concentrations were based off those measured by SIMS in this work and atom probe tomography measured in earlier work. [7] From the simulated band diagrams it can be seen that the minimum tunneling width is reduced from 4 to 3 nm at an applied voltage of -0.5 V when Si concentrations were increased from 1.8×10^{20} to 4.6×10^{20} cm^{-3}.

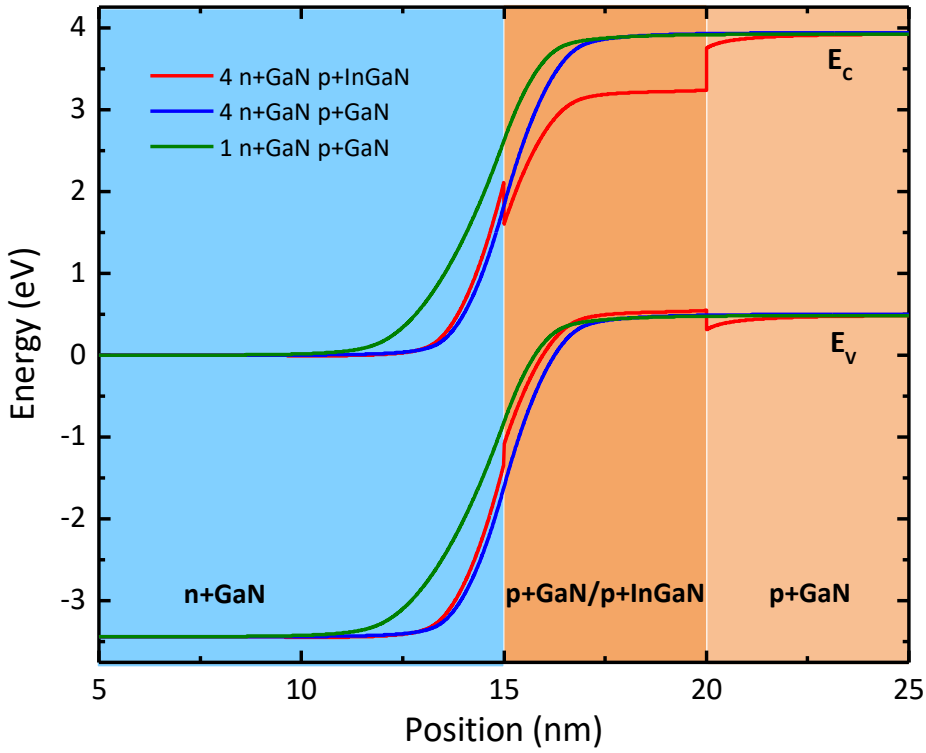

Figure 4.4 One-dimensional simulations of the band structures of the tunnel junctions at 300 K under a reverse bias 0.5V with and without a p^+InGaN capping layer and with high and low Si concentrations. Refer to Table 2.1 for sample conditions.

The addition of InGaN further reduces the barrier for interband tunneling distance due to the InGaN layer exhibiting a smaller bandgap than that of GaN. Due

to the presence of internal polarization fields in c-plane GaN, the bands around the tunnel junction interface bend even further with the addition of $In_{12}Ga_{88}N$ than they would without it. [20] This can be seen in the simulation with the further reduction in the tunneling width to 2.8 nm with the addition of a p^+InGaN capping layer.

Current-voltage measurements were taken of the processed diodes and are shown in **Figure 4.5** with sample numbers corresponding to conditions shown in Table 2.1. The presence of InGaN near the regrowth interface both reduced the turn-on voltage and series resistance of the GaN p-n diodes, indicating that the lower bandgap InGaN is indeed aiding in inter-band tunneling.

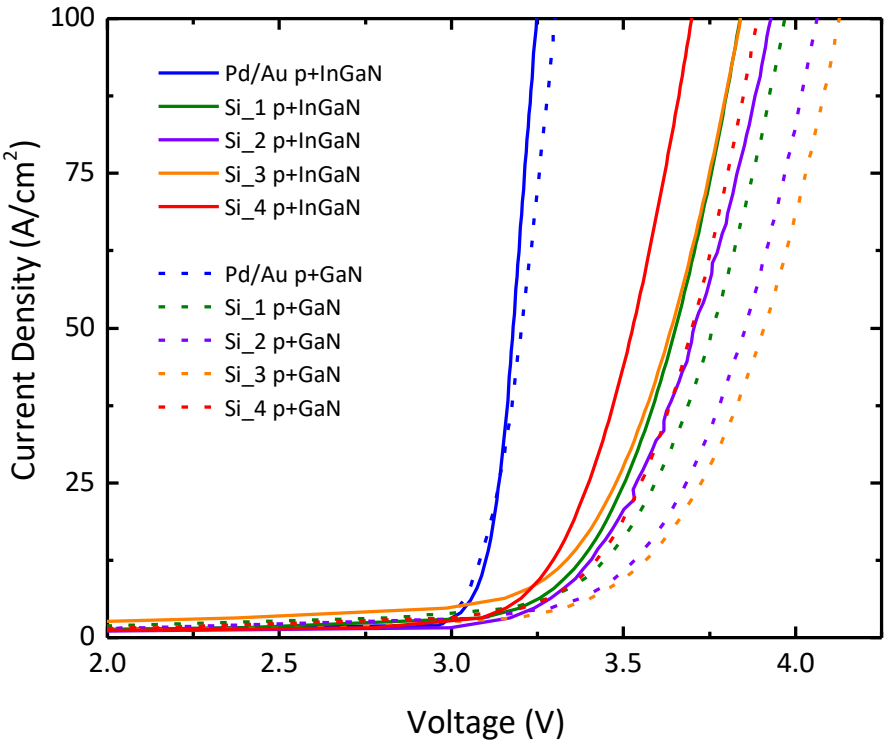

Figure 4.5 I-V characteristics of the p-n diodes containing either p^+GaN or p^+InGaN capping layers and MBE grown n^+GaN contacts with varying Si concentrations. Refer to Table 2.1 for sample conditions.

Defect states and indium fluctuations in the InGaN at the regrowth interface may also contribute to lowering the barrier to inter-band tunneling. [21] The specific series resistances of our p-n diodes are summarized in Table 2.1. Increasing Si concentration also reduced the turn-on voltages and series resistances in the p-n diodes. Specific contact resistances between metal contacts to MOCVD n^+GaN and MBE n^+GaN were measured through circular transmission line measurements (CTLM) and were found to be 3.9×10^{-6} and 1.9×10^{-5} Ω cm^2 respectively. The lowest series resistance measured, 3.4×10^{-3} Ω cm^2, was on the p-n diode containing 4.6×10^{20} cm^{-3} Si on the regrown n-GaN and a p-InGaN layer.

Although increasing the amount of Si in the regrown layer and p^+InGaN in the capping would cause increased free carrier absorption of the emitted light from optoelectronic devices, given the small thicknesses of the layers deposited these effects were negligible. As seen in **Figure 4.6**, on wafer LED LIV measurements show that increasing Si concentration at the TJ interface lowers operating voltages while light output powers are not directly affected.

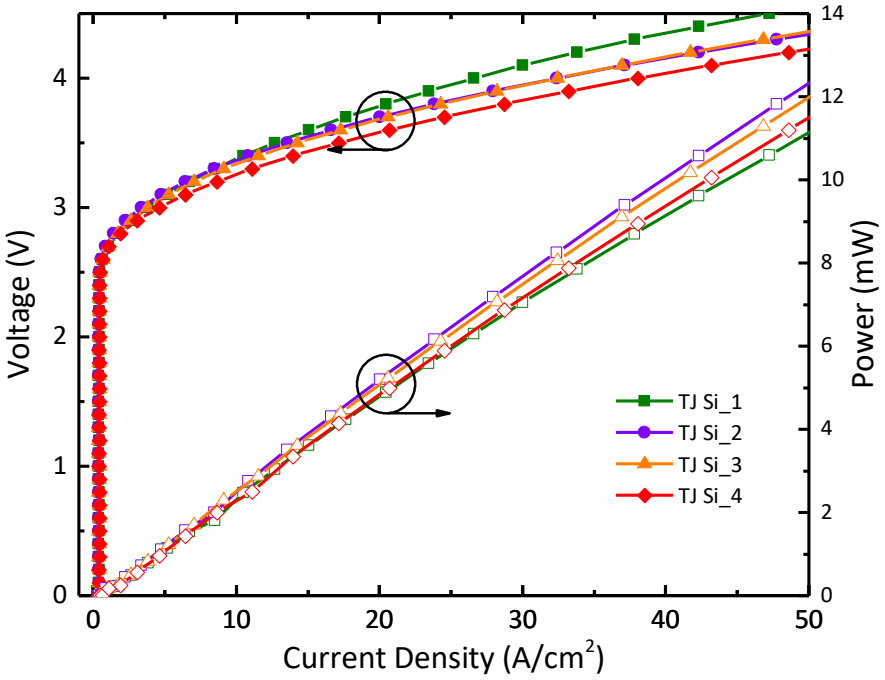

Figure 4.6 L-I-V characteristics of LEDs with MBE tunnel junctions with varying concentrations of Si at the tunnel junction interface. Refer to Table 2.1 for sample conditions.

4.5. Conclusions

In summary, we have shown that by increasing Si dopant concentrations and introducing p^+InGaN at the p-n interface of the TJ contact we can reduce resistive losses in the devices we investigated. Both conditions create a narrowing of the tunneling width required for electrons to inter-band transport.

4.6. References

[1] T. Margalith, O. Buchinsky, D. A. Cohen, A. C. Abare, M. Hansen, S. P. DenBaars, and L. a. Coldren, Appl. Phys. Lett. **74**, 3930 (1999).

[2] A. J. Mughal, S. Oh, A. Myzaferi, S. Nakamura, J. S. Speck, and S. P. DenBaars, Electron. Lett. **52**, 304 (2016).

[3] A. J. Mughal, B. Carberry, S. H. Oh, A. Myzaferi, J. S. Speck, S. Nakamura, and S. P. DenBaars, Phys. Status Solidi **214**, 1600941 (2017).

[4] L. Esaki, Phys. Rev. **109**, 603 (1958).

[5] M. Malinverni, D. Martin, and N. Grandjean, Appl. Phys. Lett. **107**, 51107 (2015).

[6] S. Krishnamoorthy, F. Akyol, and S. Rajan, Appl. Phys. Lett. **105**, 141104 (2014).

[7] E. C. Young, B. P. Yonkee, F. Wu, S. H. Oh, S. P. DenBaars, S. Nakamura, and J. S. Speck, Appl. Phys. Express **9**, 22102 (2016).

[8] C. Weisbuch, M. Piccardo, L. Martinelli, J. Iveland, J. Peretti, and J. S. Speck, Phys. Status Solidi Appl. Mater. Sci. **212**, 899 (2015).

[9] S. Krishnamoorthy, F. Akyol, and S. Rajan, Proc. SPIE - Int. Soc. Opt. Eng. **8986**, 89861F (2014).

[10] S. Sze and K. Ng, *Physics of Semiconductor Devices*, 3rd ed. (John Wiley & Sons, 2006).

[11] S. Krishnamoorthy, P. S. Park, and S. Rajan, Appl. Phys. Lett. **99**, 2 (2011).

[12] S. Krishnamoorthy, D. N. Nath, F. Akyol, P. S. Park, M. Esposto, and S. Rajan, Appl. Phys. Lett. **97**, (2010).

[13] T. Takeuchi, G. Hasnain, S. Corzine, M. Hueschen, R. P. Schneider, Jr., C. Kocot, M. Blomqvist, Y. Chang, D. Lefforge, M. R. Krames, L. W. Cook, S. A. Stockman, R. P. Schneider, C. Kocot, M. Blomqvist, Y. Chang, D. Lefforge, M. R. Krames, L. W. Cook, and S. A. Stockman, Japanese J. Appl. Phys. / Part2 **40**, L861 (2001).

[14] Y. Kuwano, M. Kaga, T. Morita, K. Yamashita, and K. Yagi, Jpn. J. Appl. Phys. **12**, 8 (2013).

[15] S. Neugebauer, M. P. Hoffmann, H. Witte, J. Bläsing, A. Dadgar, A. Strittmatter, T. Niermann, M. Narodovitch, and M. Lehmann, Appl. Phys. Lett. **110**, 102104 (2017).

[16] B. P. Yonkee, E. C. Young, C. Lee, J. T. Leonard, S. P. DenBaars, J. S. Speck, and S. Nakamura, Opt. Express **24**, 7816 (2016).

[17] J. T. Leonard, E. C. Young, B. P. Yonkee, D. A. Cohen, T. Margalith, S. P. DenBaars, J. S. Speck, and S. Nakamura, Appl. Phys. Lett. **107**, 1 (2015).

[18] B. P. Yonkee, E. C. Young, S. P. DenBaars, S. Nakamura, and J. S. Speck, Appl. Phys. Lett. **109**, 191104 (2016).

[19] H. Xing, D. S. Green, H. Yu, T. Mates, P. Kozodoy, S. Keller, S. P. DenBaars, and U. K. Mishra, Jpn. J. Appl. Phys. **42**, 50 (2003).

[20] T. Gessmann, Y.-L. Li, E. L. Waldron, J. W. Graff, E. F. Schubert, and J. K. Sheu, J. Electron. Mater. **31**, 416 (2002).

[21] T. Yang, R. Shivaraman, J. S. Speck, and Y. Wu, J. Appl. Phys. **116**, 113104 (2014).

[22] K. Kumakura, T. Makimoto, and N. Kobayashi, Appl. Phys. Lett. **79**, 2588 (2001).

Chapter 5. MOCVD Growth & Device Results

5.1. Introduction

This section will discuss the both the MOCVD growth of LED epitaxial layers on free-standing GaN substrates and device results with devices containing the three current spreading layers dealt with in this work. We will first go over a comparison between ZnO and ITO as transparent p-contacts on InGaN GaN LEDs grown on patterned sapphire substrates. Next, we will compare MBE grown n-GaN to ITO on flip chip InGaN GaN LEDs grown on patterned sapphire substrates. This is followed by growth and characterization of LEDs and device results for triangular flip chip LEDs.

5.2. ZnO vs. ITO Current Spreading Layers

Experimental Details

This work utilized commercially acquired III-nitride based LED wafers grown by metal organic chemical vapor deposition (MOCVD) epitaxially grown on patterned c-plane sapphire substrates. A 220 nm thick ITO films were deposited using e-beam deposition and rapid thermal annealer (RTA) at 600 °C for 10 minutes in 80% N_2 20% O_2. A 1100 nm thick layer of Ga doped ZnO was deposited on the LED epi-structure using a two-step approach. The first step involved the deposition of a 20 nm seed layer of unintentionally doped ZnO using heated stage (300 °C) e-

beam deposition in an O_2 ambient with a partial pressure of 3×10^{-4} Torr, followed by RTA at 500 °C for 15 min. in 80% N_2 20% O_2. The remainder of the film was then grown through the hydrothermal deposition [1] of a Ga doped ZnO film using a solution composed of 3 mMol/L sodium citrate, 25 mMol/L zinc nitrate, and 2 mMol/L gallium nitrate in 90 ml of deionized water. The sample was reacted in this solution at 90 °C for 3 hours. Sheet resistance was measured by the four-point probe, and thickness was determined with surface profilometry. This was followed by a second RTA at 250 °C for 15 min. in 80% N_2 20% O_2. 0.1 mm^2 active area LEDs were fabricated using a chlorine-based inductively coupled plasma (ICP) etch to expose the n-GaN layer. A Ti/Al/Ni/Au based n-contact, and Cr/Al/Ni/Au p-contact were deposited using ebeam deposition. The fabricated devices were packaged on a silver header and encapsulated within a silicone based truncated cone. All measurements were carried out under room temperature continuous-wave operation. White light emitting LEDs were fabricated by placing a silicone cap containing 10 wt% YAG based yellow phosphors on the blue emitting LEDs. Optical emissions were measured in a calibrated integrating sphere. More details on LED processing can be found in Appendix A.

Hydrothermal ZnO with e-beam ZnO Seed Layer

Compared to ebeam deposited ZnO seed layers, hydrothermal seed layers showed increased operating voltages, indicating that e-beam seeds should have lower contact resistances, **Figure 5.1**.

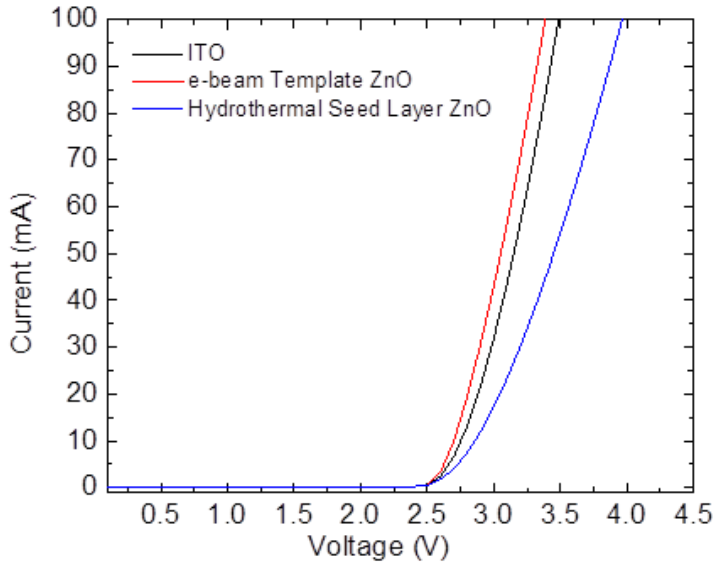

Figure 5.1 IV curves comparing ITO, full hydrothermal, and e-beam seed and hydrothermal ZnO

The power outputs and voltages of packaged LEDs containing ZnO and ITO CSL are shown in **Figure 5.2**. The two devices exhibit similar turn-on voltages, but with increasing drive currents ZnO CSL LEDs exhibit lower forward voltages. The series resistances measured from ZnO and ITO devices are 5.6 and 7 Ω respectively. Since the LED epi-structure is the same for in both cases, these results

indicate that ZnO may have a lower contact resistance to p-GaN when compared to ITO. Light output power (LOP) between the two devices shows greater light emission from ZnO based devices. At 400 A/cm^2 ZnO CSL LEDs exhibit a 22% increase in LOP when compared with ITO.

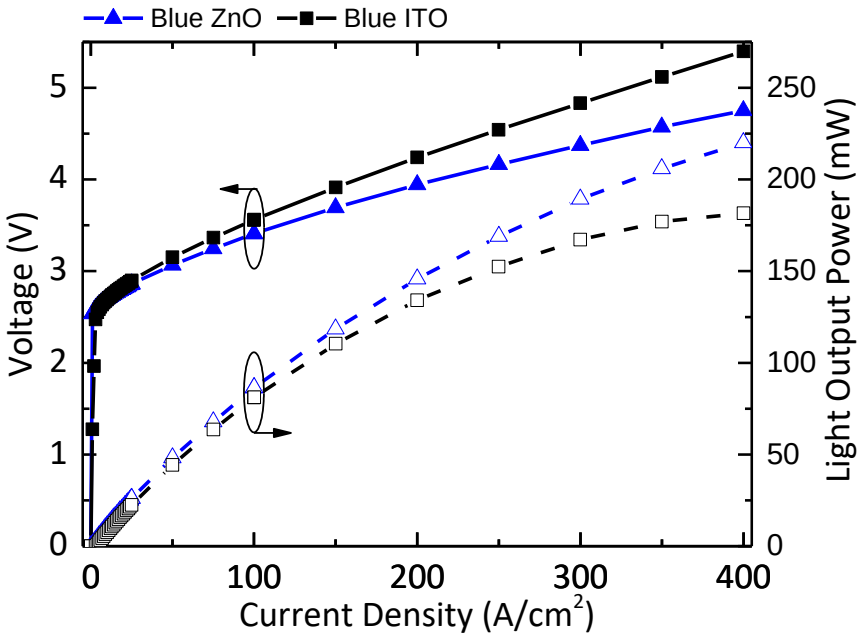

Figure 5.2 LIV characteristics of blue emitting ZnO and ITO LEDs

Efficiency droop due to high carrier densities [2] as well as high temperatures [3] can be seen at high current densities. **Figure 5.3** displays the shift in the peak wavelength of the two LED measured under increasing drive currents. The LEDs initially featured large blue-shifts upon increasing the forward current. This behavior results from screening of the piezoelectric field in the MQWs by the

injected carriers, and carriers filling up to a higher energy level upon increasing the current density. Emission wavelengths being to show red-shift behavior at 200 A/cm^2 and 300 A/cm^2 for ITO and ZnO respectively, with ITO LEDs showing significantly greater red-shifting behavior. This behavior is indicative of ohmic heating of the device resulting in a decrease of the active region's bandgap [4].

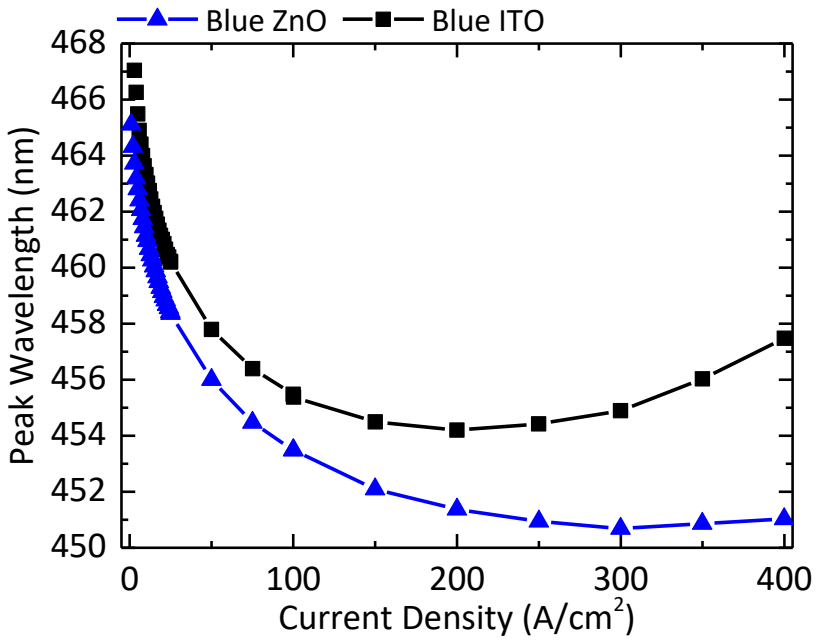

Figure 5.3 Peak emission wavelength shift with current density of blue emitting ZnO and ITO CSL LEDs

External quantum efficiency (EQE) and wall plug efficiency (WPE) values, displayed in **Figure 5.4**, further illustrated the improved performance of ZnO CSL based LEDs. Peak EQE of 42% and 33% were measured for ZnO and ITO based LEDs respectively with WPE values showing similar trends. Since EQE values do

not consider the operating voltage of the device, this gain can be attributed to lower current crowding and or enhanced light extraction. The combined effects of series resistance and EQE are represented by WPE values and show a correspondingly greater difference with peak values of 44%, and 31% for ZnO and ITO based LEDs respectively.

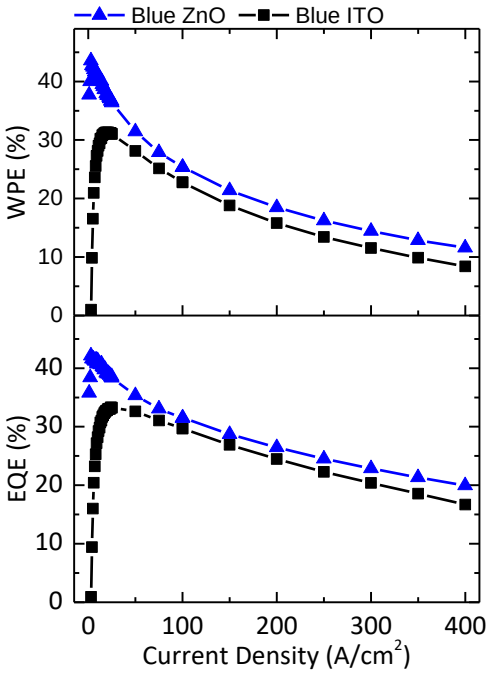

Figure 5.4 EQE and WPE characteristics of blue emitting ZnO and ITO CSL LEDs

The luminous flux and efficacy of white converted blue LEDs are shown in **Figure 5.5**. White converted ZnO based LEDs output greater luminous fluxes across all drive currents. Luminous efficacy increases greatly for ZnO based CSL with a peak value of 113 lm/W compared with 82 lm/W for ITO based CSL, a 37%

improvement. This can be attributed to the lower forward voltages achieved with ZnO in addition to possibly enhanced light extraction.

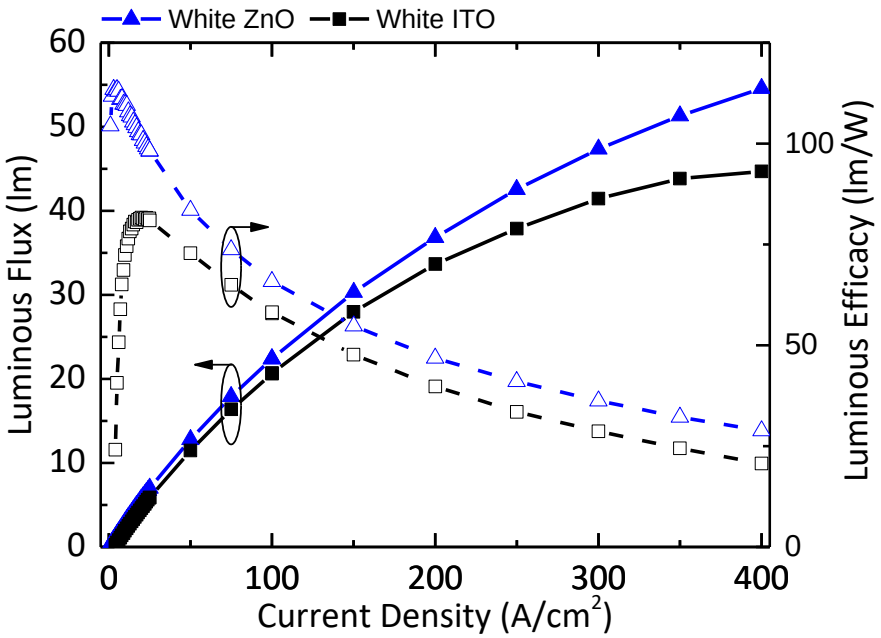

Figure 5.5 Luminous Flux and Efficacy of white light emission from ZnO and ITO CSL LEDs

In conclusion, we have shown improved device performance of GaN-based LEDs using Ga:ZnO current spreading layers with e-beam deposited seed layer when compared to conventional e-beam ITO. All metrics measured showed improved performance of ZnO based CSL compared with ITO. Lower forward voltages, in addition to greater light extraction, contribute to this enhancement.

All Hydrothermal ZnO

A two-step low temperatures solution based deposition technique was employed to grow thin film doped ZnO transparent contacts on 2" InGaN blue LEDs on patterned sapphire substrates. For the first step, a template seed layer is deposited using an aqueous solution of nitrate salts (i.e., $Zn(NO_3)_2$ and NH_4NO_3) and mineralizer (NH_4OH). Nucleation of these seed crystals occurs at 90 °C under ambient pressures. For the second step, a thicker epitaxial layer is grown, again using nitrates salts (i.e., $Zn(NO_3)_2$ and $Ga(NO_3)_3$), crystal growth modifier (Na-citrate), and a mineralizer (NH_4OH). This step also occurs at 90 °C. After each step, an anneal of the film is carried out using a rapid thermal annealer (RTA), first at 500 °C for the seed layer and 250 °C for the second epitaxial layer. These annealing steps improve electrical contact with the underlying p-GaN as well as ionize the Ga dopants. **Figure 5.6** shows typical morphologies for the seed and epitaxial layers grown using this process.

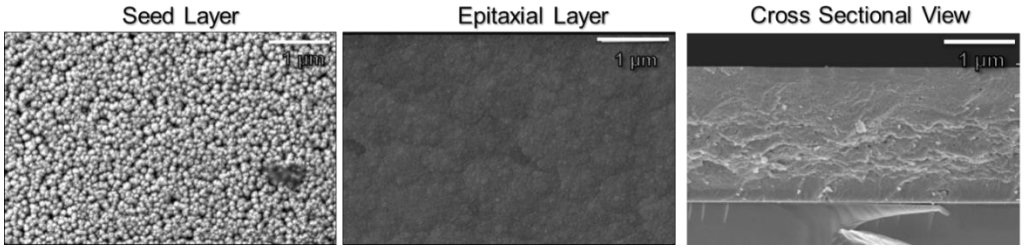

Figure 5.6 SEM micrographs of ZnO seed layer, epitaxial layer, and a cross-section of the final film

Several experiments have been carried out to evaluate solution-based deposition of doped ZnO transparent contacts. Doped ZnO has successfully been deposited on full 2-inch wafers, showing its scalability for commercial manufacture.

In addition, packaged LED devices have been produced with 2 microns of doped ZnO transparent contacts and compared to those using standard ITO. Ga doped solution deposited ZnO transparent contacts have been successfully grown on LED devices. As seen in **Figure 5.7** and **Table 5.1**, they show improved performance compared to ITO.

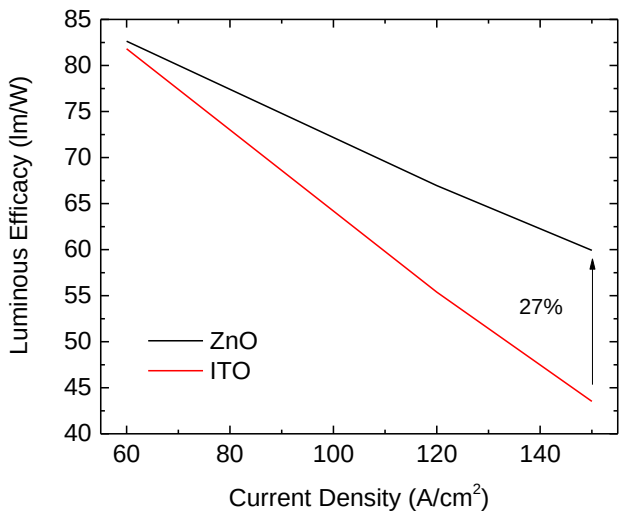

Figure 5.7 Efficacy vs. current density of packaged ITO and ZnO LEDs

Table 5.1 Comparison between Ga:ZnO and ITO at three current densities

@60mA	lm	CRI	Vf(V)	Power (W)	Efficacy (lm/W)
UCSB-ZnO(A)	15.47	85.44	3.12	0.1872	**82.64**
ES-9x20	17.07	82.17	3.33	0.1998	**85.44**
@120mA	**lm**	**CRI**	**Vf(V)**	**Power (W)**	**Efficacy (lm/W)**
UCSB-ZnO(A)	27.4	85.23	3.41	0.4092	**66.96**
ES-9x20	26.34	83.37	3.69	0.4428	**59.49**
@150mA	**lm**	**CCT**	**Vf(V)**	**Power (W)**	**Efficacy (lm/W)**
UCSB-ZnO(A)	30.92	85.55	3.44	0.5160	**59.92**
ES-9x20	28.02	84.87	3.79	0.5685	**49.29**

Due to the ease in which thick layers of ZnO (2 μm) can be grown, they have a significant advantage to thinner ITO films (200 nm) in terms of current spreading since it results in ZnO having much lower sheet resistances as compared to ITO. This is especially significant at higher current densities since it results in less droop in output power.

5.3. MBE n^+GaN vs. ITO

Experimental Details

Blue emitting InGaN LEDs utilizing MBE n-GaN TJ p-contacts were processed using five lithography masks to produce devices with top side n and p contacts. This processing includes a mesa etch, a seven-layer SiO2/Ta2O5 dielectric omnidirectional mirror, Al mirror n-contact, an n/p isolating dielectric, and a final Au metal pad. This was done so that the LED die can be bonded to a submount in

a flip chip configuration. The submount is composed of a SiC substrate with an 11-layer SiO2/Ta2O5 dielectric omnidirectional mirror, and Ti/Au patterned pads. Flip chip bonding allows for better current spreading through the p-GaN and enhanced light extraction since the light is emitted through the substrate while the p-GaN is exposed to the pad layer. A process follower for this device is provided in Appendix A. The Flip chip procedure was carried out using a Dexerials flip chip bonder. This process has successfully been performed on InGaN LEDs grown on patterned sapphire substrates (PSS) that have either 170 nm e-beam deposited ITO or 350 nm MBE deposited n-GaN.

Flip Chip LED Device Results

Figure 1 summarizes some of the initial results obtained for comparing ITO and n-GaN p-contacts on flip chipped PSS InGaN LEDs. **Figure 5.8**a shows the dimensions and structure of the LED die used in these experiments. The n-contact pad is the smaller of the two. The IV curves as illustrated in **Figure 5.8**b indicates that the n-GaN TJ contacts show higher turn-on voltage and similar series resistance when compared to ITO. Higher voltages are expected for the TJ contacts since the n-GaN is not degeneratively doped and required additional voltage to tunnel carry through when compared to ITO. EQE, **Figure 5.8**c, and WPE, **Figure 5.8**d, both show that the ITO sample exhibits better performance. The reasons for this is still

under investigation. In both cases, the samples show very low-efficiency droop, likely due to enhanced current spreading under the flip chip configuration.

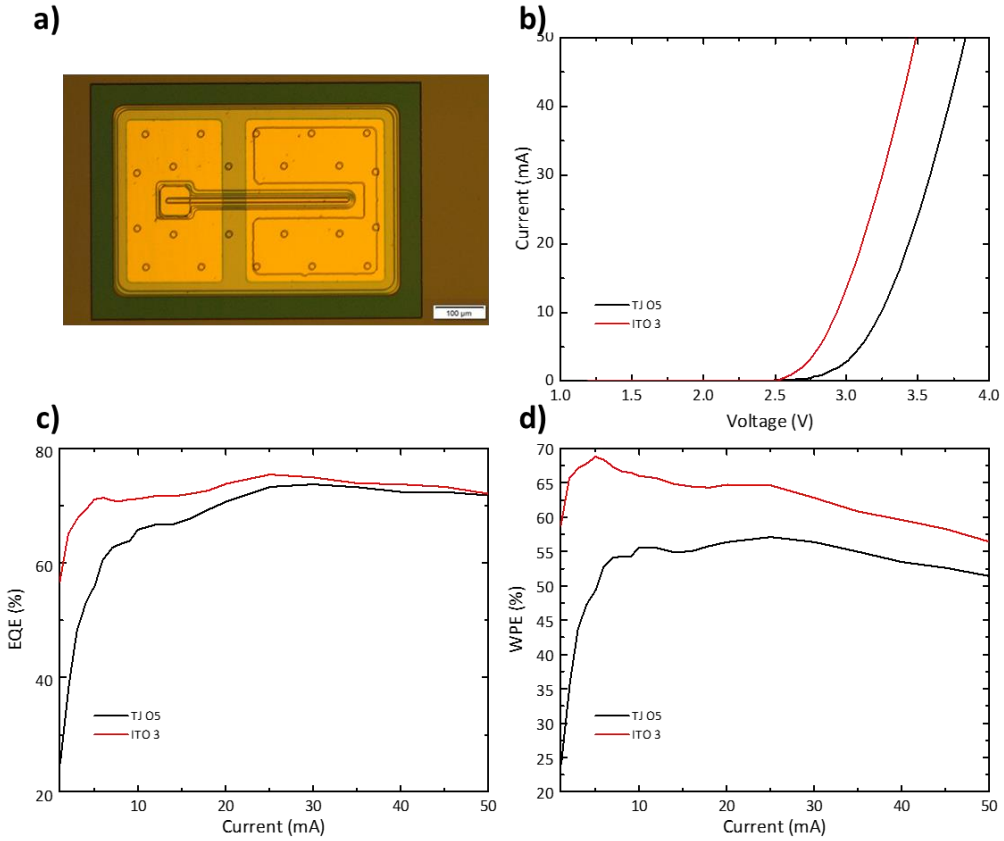

Figure 5.8 a) optical micrograph of flip chip PSS LED die, b) IV curves, c) EQE plots, and d) WPE plots for ITO and TJ LEDs.

5.4. MOCVD on Free-Standing GaN Substrates

Growth

MOCVD was employed to grow InGaN/GaN blue LEDs homoepitaxially on free-standing GaN substrates. We used a customized Tayo-Nippon Sanso MOCVD system with a two-flow growth chamber. Substrates were diced and cleaned using the procures outlines in Appendix B. **Figure 5.9** describes the basic structure of the LED epitaxial layers. The three major regions are displayed in blue, red, and green in this schematic. The first layers, shown in blue, are the template and n-GaN layers. It is important to have a smooth template so that subsequent structures can be properly grown.

p+ GaN:Mg	8.3	nm
p+ GaN:Mg	5.7	nm
p- GaN:Mg (In)	114	nm
AlGaN:Mg EBL	26	nm
HT GaN barrier (Δ 50C)	14	nm
LT GaN barrier	2.4	nm
InGaN well	3.1	nm
LT GaN barrier	2.4	nm
HT GaN barrier (Δ 50C)	14	nm
n- GaN	2.4	nm
n+ GaN	7.1	nm
n- InGaN:Si supperlattice	3.3	nm
n- GaN:Si superlattice	3.3	nm
n+ GaN:Si template	180	nm
n+ GaN:Si template	113	nm
n- GaN:Si template	675	nm
c-GaN substrate		

Figure 5.9 Schematic of epitaxial layers for blue GaN/InGaN LED

Defects in this layer can propagate through subsequent materials and short devices or lower performance. The first parameter when it comes to growth is the free-standing GaN substrate. Substrates tested included SIOCS (formally Hitachi Cable), Mitsubishi Chemical Corporation (MCC), Lumilog, and Nanowin. Substrates from Suzhou Nanowin Science and Technology Co., Ltd exhibited the best performance. Since GaN substrates bow due to internal stresses and are polished flat after dicing the boule, the miscut varies across the wafer. This can have a significant effect on the growth of the template layers. Regarding growth, proper growth temperatures and III/V ratio is critical for smooth morphologies.

AlGaN layers can also help create smooth templates. Once the template is formed, Si concentrations can be increased to lower the resistivity of the n-GaN side of the device. The GaN/InGaN superlattice shown in the blue region of **Figure 5.9** is used to reduce the built-in potential and help trap any threading dislocations formed in the template layer. The red region includes the quantum well and duels barrier layers which constitute the active region. The two barrier layers differ in the temperatures at which they are grown. This two-step barrier is helping improve the quality of the barrier (high-temperature growth) while protecting the quantum wells (low-temperature growth). The green region included the p-GaN layer and the p-AlGaN electron barrier layers. Growth temperature and Mg flows are the main growth parameters for these layers. It is flown into the reactor as a surfactant during p-GaN growth to improve surface mobility and achieve smoother films. The final layer includes a p+ layer which helps reduce contact resistivity. This p+ GaN layer can be replaced by p+InGaN to reduce contact resistivity further.

Further details regarding the MOCVD growth, including specific growth recipes, can be found in Appendix B.

Characterization

Characterization of the films was mainly carried out through In dot "quick test" optical microscopy, and photoluminescence (PL). The quick test provides relative information on light output power, emission wavelength, and forward voltage.

Optical microscopy provided information on surface morphology. In addition, AFM and secondary ion mass spectroscopy (SIMs) was carried out to obtain more detailed morphological and compositional analysis. Shown in **Figure 5.10**a is a typical optical micrograph of the LED film surface. Most growths exhibited this wavy surface. PL imaging, **Figure 5.10**b, revealed that the films exhibited fine variation in emission within the wavy morphology. This may be due to In fluctuation in the InGaN layers. AFM analysis also exhibited this wavy feature indicating that it represents a surface texture as well as compositional variation. The 50 by 50 μm scan has a root mean square (rms) roughness of 1.69 nm, **Figure 5.10**c. The 5 by 5 μm scan indicated an rms roughness of 0.46 nm, **Figure 5.10**d.

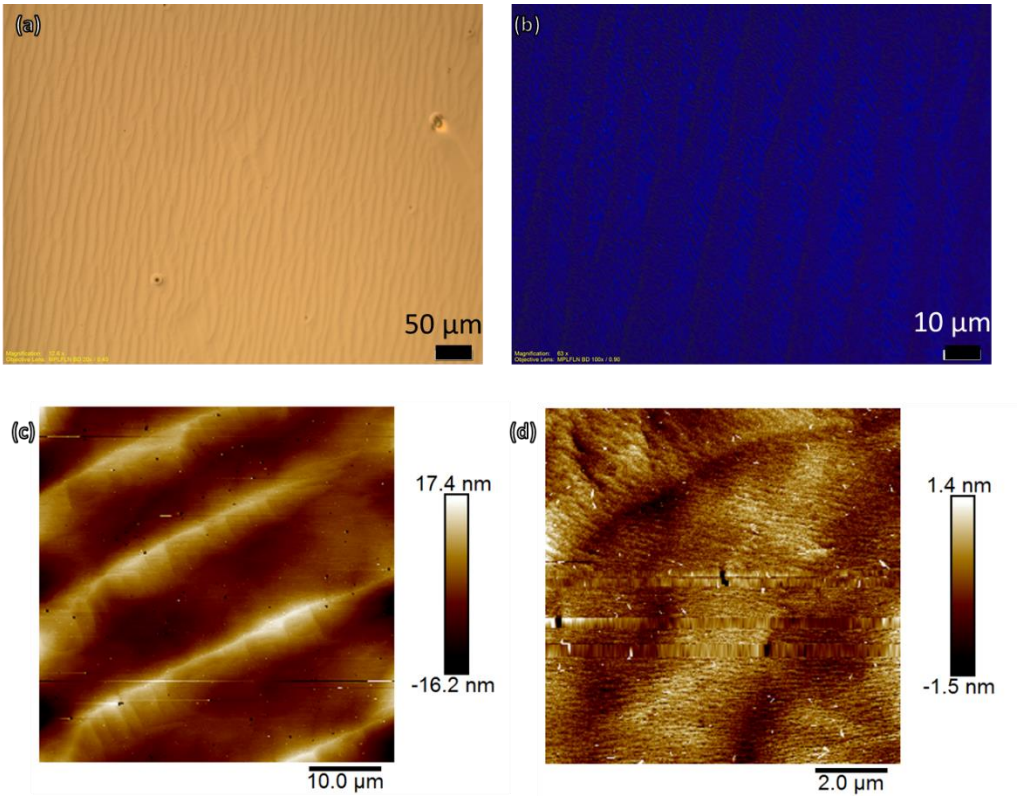

Figure 5.10 (a) optical micrograph of InGaN/GaN LED film on free-standing GaN substrates (b) photoalignment optical micrograph (c) 50x50 µm AFM micrograph and (d) 50x50 µm AFM micrograph

The full SIMS depth profile of the LED films is displayed in **Figure 5.11**a. Several notable aspects are present in this profile. For one, the initial AlGaN layer on top of the substrate contains many of the elements found in the subsequent layers. This is likely due to the presence of their respective precursors in the growth chamber during the time of growth. The solution to this would be to alternate growths with "baking" of trays to remove any residuals. Another interesting aspect is that Al is all throughout the template and superlattice layers. **Figure 5.11**b

displays a magnified view of the SIMs profile. Due to possible roughness or uneven etching during the SIMs scan, composition values may have smeared across the depth of the film. The tails in In, Al, and Mg may be due to measurement artifacts and not representative of the actual films.

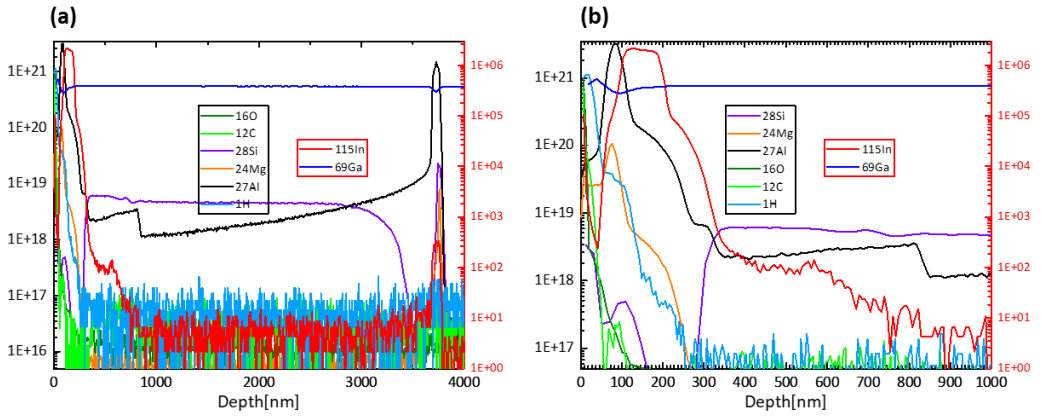

Figure 5.11 (a) Full SIMs depth profile and (b) magnified profile of a blue InGaN/GaN LED film on free-standing GaN substrates

5.5. Flip Chip LEDs on GaN Substrates

Experimental Details

Flip Chip LEDs using bulk substrates are currently being investigated. MBE n-GaN based tunnel junctions on InGaN LEDs on both semipolar 20-2-1 and c-plane 0001 freestanding GaN substrates are currently being processed. They utilize a triangular die to enhance light extraction and require additional steps after fabricating the dies to package. This includes grinding down the absorbing substrates, polishing, dicing, and roughening before flip chipping and finally

packaging. Details regarding the processing of these devices are outlined in Appendix A. A schematic cross-section of the device is shown in **Figure 5.12**. Since an MBE n-GaN TJ p-contact was employed, a common Al/Ni/Au contact was used for both the bottom and top n-GaN.

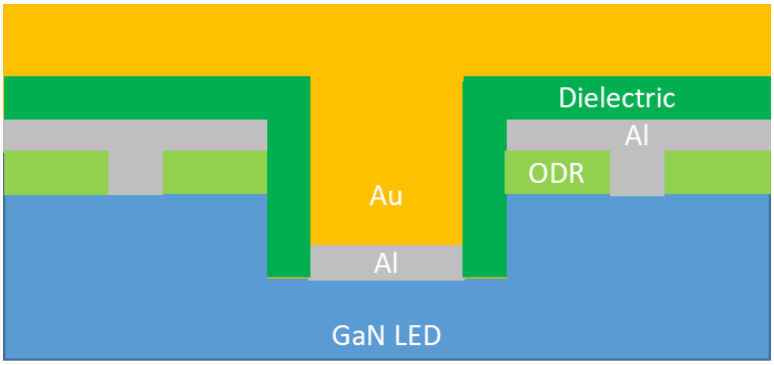

Figure 5.12 Schematic cross-section of a flip-chip LED

The top and bottom contacts were separated by a PECVD SiN dielectric layer which was deposited in two steps with a dip in DI water in between. This was done to ensure that there were not pin holes from which the device can short itself. A seven-layer ODR was deposited to enhance light reflectance once the device is flipped. The N-face of the GaN substrate was roughened using a dilute mixture of AZ MIF300 solution in water (1:1). Samples were submerged in a heated bath (60 ° C) of this solution of 10 min to achieve the proper level of roughening. The device side of the structure was protected by spinning on positive photoresist (SPR 220 3.0)

Flip Chip LED Device Results

Although InGaN/GaN blue LEDs were successfully grown on freestanding GaN substrates and processed into flip-chip triangular LEDs, their performance was much lower than expected based off 'quick test' results on the initial thin films. **Figure 5.13**a shows the dimensions and shape of these LED with **Figure 5.13**b showing one under 20 A/cm^2. The n and p contact pads were flip-chip bonded to submount pads using LEP epoxy which contain small spheres of Au/Sn solder that form vertical contacts between pads. A SEM micrograph of a flip chip LED is presented in **Figure 5.13**c. The roughened N-face of the GaN substrate is shown in the SEM micrograph in **Figure 5.13**d.

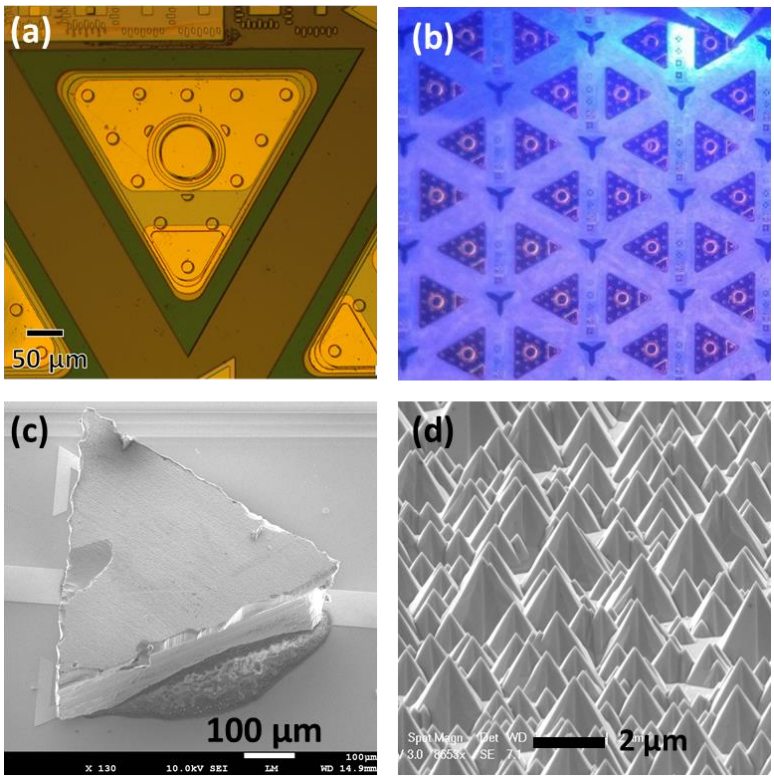

Figure 5.13 a) optical micrograph of triangular flip chip LED processed on freestanding c-GaN substrates b) same LEDs under bias

LIV results are presented in **Figure 5.14**a. At 20 A/cm^2 the forward voltage was 4.2V, and light output power was only 6 mW. This led to maximum EQE and WPE values of only 26% and 20% respectively, **Figure 5.13**b. This is even though the quick-test power of about 8 mW at the same current density. The cause for this is was not verified, but some issue with processing may have been the cause. In addition, quick-test powers varied greatly across the substrate making it difficult to find processed devices with high output powers.

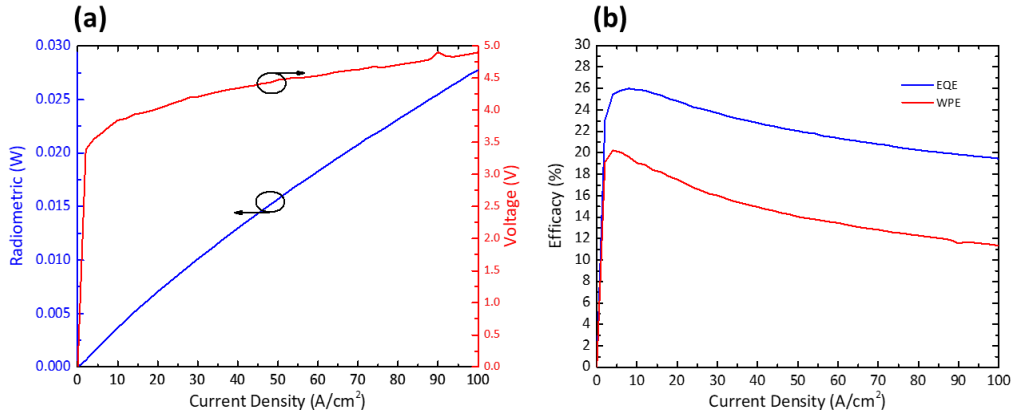

Figure 5.14 a) LIV curves for flip chip triangular LEDs and b) corresponding EQE and WPE values

5.6. Conclusions

In summary, ZnO CSL on InGaN blue LEDs shows a marked improvement in performance when compared to ITO. ZnO exhibits both lower operating forward voltages, as well as higher light output powers, over ITO based CSLs. This yield to improved efficiencies in terms of higher EQE and WPE. MBE deposited n-GaN CSL on InGaN blue flip chip LEDs did not show improved performance over ITO. Even though the ODR was optimized for GaN, the devices with ITO outperformed those with n-GaN. One of the highest reported EQE and WPE were those done on flip-chip devices containing MBE n-GaN contacts [5], so there may have been regrowth or processing issues with these experiments.

Although we were unable to achieve consistent performance on MOCVD InGaN blue LED on free-standing GaN substrates and the devices processed from these materials exhibited mediocre performance, this should be a promising

approach to creating high-efficiency devices. If issues with growth and processing can be resolved, then record-breaking performances can be possible.

The next chapter will conclude this dissertation with a brief summary and a discussion on future works.

5.7. References

[1] J. H. Kim, E.-M. Kim, D. Andeen, D. Thomson, S. P. DenBaars, and F. F. Lange, Adv. Funct. Mater. **17**, 463 (2007).

[2] J. Iveland, L. Martinelli, J. Peretti, J. S. Speck, and C. Weisbuch, Phys. Rev. Lett. **110**, 177406 (2013).

[3] Seoung-Hwan Park and Yong-Tae Moon, IEEE Photonics J. **6**, 1 (2014).

[4] H. Herr, V. Alex, and J. Weber, MRS Proc. **482**, 719 (1997).

[5] B. P. Yonkee, E. C. Young, S. P. DenBaars, S. Nakamura, and J. S. Speck, Appl. Phys. Lett. **109**, 191104 (2016).

Chapter 6. Conclusions & Future Work

6.1. Final Conclusions

Hydrothermal ZnO Transparent Current Spreading Layers

Group III impurity-doped ZnO thin films deposited on $MgAl_2O_3$ substrates using a simple low-temperature two-step deposition method involving atomic layer deposition and hydrothermal epitaxy. Films with varying concentrations of either Al, Ga, or In were evaluated for their optoelectronic properties. Inductively coupled plasma atomic emission spectroscopy was used to determine the concentration of dopants within the ZnO films. While Al and Ga doped films showed linear incorporation rates with the addition of precursors salts in the hydrothermal growth solution, In-doped films were shown to saturate at relatively low concentrations. It was found that Ga doped films showed the best performance regarding electrical resistivity and optical absorbance when compared to those doped with In or Al, with a resistivity as low as 1.9 mΩ cm and an optical absorption coefficient of 441 cm^{-1} at 450 nm.

Impurity doped heteroepitaxial thin films of (0001) ZnO onto (111) $MgAl_2O_4$spinel substrates through a combination of atomic layer deposition (ALD) and hydrothermal growth. The hydrothermal layer is doped with Al, Ga, and In through the addition of their respective nitrate salts. We evaluated the effect that

varying the concentrations of these dopants has on both the structural and optical properties of these films. It was found that the epitaxial ALD layer created a $<111>_{MgAl2O4} \parallel <0001>_{ZnO}$ out of plane orientation and a $<\bar{1}\bar{1}2>_{MgAl2O4} \parallel <01\bar{1}0>_{ZnO}$ in-plane orientation between the film and substrate. The rocking curve line widths ranged between 0.75 and 1.80° depending on dopant concentration. The optical bandgap determined through the Tauc method was between 3.28 to 3.39 eV and showed a Burstein-Moss shift with increasing dopant concentration.

The performance of LEDs with Ga-doped ZnO (Ga:ZnO) and Sn-doped In2O3 (ITO) current-spreading layers (CSLs) has been evaluated at high injection current densities. LEDs with electron beam-hydrothermally deposited Ga:ZnO transparent CSLs showed improved performance compared to electron beam deposited ITO at all current densities. External quantum efficiency and wall plug efficiency were both higher for blue emitting LEDs with ZnO. Luminous efficacy increased greatly for the ZnO-based CSL with a peak value of 113 lm/W compared to 82 lm/W for the ITO-based CSL, a 37% improvement.

MBE GaN Tunnel Junctions

Improved turn-on voltages and reduced series resistances have been realized by depositing highly doped Si-doped n-type GaN using MBE on polarization enhanced p-type InGaN contact layers grown using MOCVD. We compared the effects of different Si doping concentrations and the addition of p-type InGaN on the forward

voltages of p-n diodes and LEDs. It was found that increasing Si concentrations from $1.9x10^{20}$ to $4.6x10^{20}$ cm^{-3} and including a highly doped p-type InGaN at the junction both contribute to the narrowing of the depletion width, lowering series resistance from $4.2x10^{-3}$ to $3.4x10^{-3}$ Ω cm^2 and decreasing turn-on voltages of the diodes. Band structure simulations between ZnO and GaN TJ show that they exhibit similar depletion widths. The presence of additional defect states may account for the improved performance of ZnO current speading layers.

6.2. Future Work

Sputter Deposition

A low resistance tunnel junction on top of p-GaN would allow for current spreading in n-type GaN (n-GaN) on both sides of the device, as well as the use of low resistance n-type contacts on both sides of the device. A tunnel junction is a diode comprised of a very highly doped (n^+/p^+) interface that allows for electrons to tunnel between the valence band and conduction band. This was first demonstrated by Esaki [1] in highly-doped Ge homojunction diodes with very thin depletion regions. In principle, a highly doped Esaki-type homojunction diode should provide the lowest-loss tunnel junction. However, there have been many difficulties in achieving high-quality tunnel junctions in the GaN material system.

For example, GaN is a wide bandgap semiconductor, so the barrier for tunneling is high. Several approaches to reducing the tunneling barrier have been attempted,

including bandgap engineering via polarization (AlN interlayers) [2], reducing the bandgap with an InGaN interlayer [3], and introducing defect states via interfacial GdN nanoparticles [4]. However, these approaches are associated with losses, either regarding voltage or resistance increases, or optical losses in the final device performance. In another example, magnesium (Mg) doped p-GaN grown by metal-organic chemical vapor deposition (MOCVD) is compensated by hydrogen as grown, and it must be annealed after growth to remove the hydrogen. This anneal can only work if the p-GaN is not covered by n-GaN, as hydrogen cannot easily diffuse through n-GaN. This limits the effectiveness of tunnel junctions and prevents their widespread use.

To overcome the limitations described above, a sputter deposition method for III-nitride and ZnO may be used to deposit transparent current spreading contact layers to p-GaN effectively. By combining MOCVD grown light emitters or absorbers and ECR or magnetron sputter deposited tunnel junctions, the operating voltage of these devices could be reduced, and their efficiency could be increased. New types of device structures, including novel designs for light-emitting diodes (LEDs), vertical cavity surface emitting lasers (VCSELs), edge-emitting laser diodes (EELDs), and solar cells. For example, the tunnel junctions could be used to incorporate multiple active regions into a single device, which could increase the performance of EELDs and VCSELs by providing additional gain or reduce the droop in LEDs by achieving more light at the same current density. Also, n-type

GaN (n-GaN) can be used as a current spreading layer on both sides of the device, eliminating the need for a TCO layer or silver (Au) mirror. The use of low resistance n-contacts on both sides of the device would be especially useful for lasers where the main resistance comes from the p-contacts. In addition, since sputter deposition tools are commonly used in semiconductor processing on an industrial scale, this method of forming III-nitride tunnel junctions can be readily commercialized.

Sputter deposition is a type of physical vapor deposition (PVD) method used to form thin films of various materials and microstructures. This is achieved by bombarding a target material to ionized atoms of an inert gas, such as argon, or a reactive gas, such as oxygen or nitrogen. Because of this bombardment atoms of the target material are ejected and transported in the gas phase onto a substrate where they condense and form a thin film. The source of these ions is typically from a plasma which is formed by applying a large negative potential to a cathode (i.e., the target material) under high vacuum conditions [5]. The plasma is sustained in part due to the formation of secondary electrons produced during interactions between ions and the target surface. The ionization process can be enhanced using magnetic fields in magnetron sputtering systems. The plasma is typically generated using either a radio frequency (RF), direct current (DC), or pulsed DC power supply [6].

Although there exist several demonstrations of sputter deposited GaN thin films, they have yet to be shown to behave as tunnel junction contacts to p-GaN [7–9]. This is in part since p-GaN is quite sensitive to plasma damage since most sputtering techniques expose the surface of the substrate (i.e., p-GaN layer) to the same plasma that is used to bombard the target [10,11]. The solution to this issue is to either protect the p-GaN from this type of damage or minimize its exposure to the plasma. An alternative sputtering approach is to generate the plasma remotely to minimize its adverse effects on the p-GaN surface. One technique to achieve this is to use electron cyclotron resonance (ECR) plasma sources. In this case, microwave power is coupled to the plasma at the ECR frequency to produce high-energy electrons which ionize the neutral input gas to produce and maintain a dense, low-pressure plasma with a high degree of ionization [12], as seen in **Figure 6.1**.

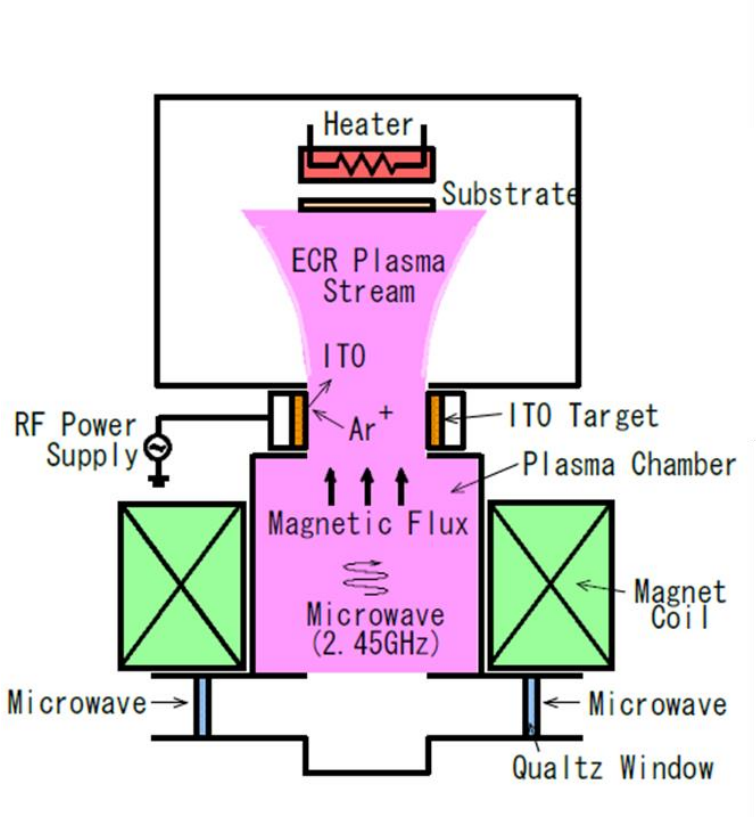

Figure 6.1 Schematic of ECR deposition system

This process produces low energy ions which mitigate plasma damage [13]. ECR plasmas are typically used to with gaseous precursors in chemical vapor deposition (CVD) systems. Solid source ECR plasma deposition methods also exist and have yielded high-quality epitaxial ITO [14] and AlN [15] thin films

By using ECR or magnetron plasma deposition to grow the n-GaN layer on top, the p-GaN remains activated while being buried beneath the n-GaN. This could allow for the regrowth of additional LED epitaxial layers by MOCVD on top of the first LED because the hydrogen cannot diffuse through the top n-GaN layer.

In addition to the tunnel junction LEDs described above, this technique can also be applied to VCSELs, which has a long history of prior art dating back to the 1970's [16]. III-nitride VCSELs represent a new class of VCSELs that represent a new set of unique challenges and device designs compared to conventional III-arsenide VCSELs [17]. Sputter deposition provides a regrowth technique for achieving high-quality III-nitride tunnel junction intracavity contacts in III-nitride VCSELs.

6.3. References

[1] L. Esaki, Phys. Rev. **109**, 603 (1958).

[2] J. Simon, V. Protasenko, C. Lian, H. Xing, and D. Jena, Science **327**, 60 (2010).

[3] S. Krishnamoorthy, F. Akyol, and S. Rajan, Appl. Phys. Lett. **105**, 141104 (2014).

[4] S. Krishnamoorthy, F. Akyol, P. S. Park, and S. Rajan, Appl. Phys. Lett. **102**, 113503 (2013).

[5] P. J. Kelly and R. D. Arnell, Vacuum **56**, 159 (1999).

[6] R. Keatch, Microelectronics J. **27**, 804 (1996).

[7] T. Kikuma, K. Tominaga, K. Furutani, K. Kusaka, T. Hanabusa, and T. Mukai, Vacuum **66**, 233 (2002).

[8] M. Junaid, C.-L. Hsiao, J. Palisaitis, J. Jensen, P. O. A. Persson, L. Hultman, and J. Birch, Appl. Phys. Lett. **98**, 141915 (2011).

[9] N. Elkashef, R. S. Srinivasa, S. Major, S. C. Sabharwal, and K. P. Muthe, Thin Solid Films **333**, 9 (1998).

[10] X. A. Cao, A. P. Zhang, G. T. Dang, F. Ren, and S. J. Pearton, J. Electron. Mater. **29**, 256 (2000).

[11] S. J. Chang, C. H. Lan, J. D. Hwang, Y. C. Cheng, W. J. Lin, J. C. Lin, and H. Z. Chen, J. Electrochem. Soc. **155**, H140 (2008).

[12] Z. Y. Ning, S. Y. Guo, and S. H. Cheng, Vacuum **52**, 219 (1999).

[13] K. Xie, J. R. Flemish, J. H. Zhao, W. R. Buchwald, and L. Casas, Appl. Phys. Lett. **67**, 368 (1995).

[14] S. Kaneko, H. Torii, M. Soga, K. Akiyama, M. Iwaya, M. Yoshimoto, and T. Amazawa, Jpn. J. Appl. Phys. **51**, 01AC02 (2012).

[15] S. Kaneko, T. Ito, M. Yasui, M. Kurouchi, H. Torii, T. Amazawa, T. Tikumasu, T. Nagano, L. Seughwan, S. Park, and H. Takikawa, 2013 IEEE 6th Int. Conf. Adv. Infocomm Technol. ICAIT 2013 **3**, 69 (2013).

[16] K. Iga, IEEE J. Sel. Top. QUANTUM Electron. **6**, (2000).

[17] D. F. Feezell, in edited by J.-I. Chyi, H. Fujioka, and H. Morkoç (International Society for Optics and Photonics, 2015), p. 93631G.

Appendix A. ZnO Growth and Device Processing

A.1. Introduction

This appendix provides the processing details for the 'standard LED' and 'Flip-Chip LED' processes used in this dissertation. The standard process was used on c-plane InGaN/GaN LEDs grown on patterned sapphire substrates with the various p-contact current spreading electrodes. The flip-chip process was used on c-plane and semipolar free-standing GaN substrates

A.2. Hydrothermal ZnO

Outlined in this section are the values, calculations, and measurements used in determining the molar concentrations of solutions used in the hydrothermal deposition of ZnO thin films. Table 2 summarizes the molar mass values for them to calculate the concentrations utilized in the hydrothermal grown of ZnO.

Table 2 Molar mass values for elements and compounds used in hydrothermal ZnO deposition

Compound	Chemical Formula	Molar Mass (g/mol)		
Hydrogen	H	1		
Oxygen	O	16		
Nitrogen	N	14		
Zinc	Zn	65.4		
Aluminum	Al	26.98		
Ga	Ga	69.72		
Indium	In	114.82		
Nitrate	NO3	62		
Water	H20	18		
Zinc Nitrate	Zn(NO3)2	189.4		
Zinc Nitrate Hexahydrate	Zn(NO3)2 * 6H2O	297.4		
Zinc Oxide	ZnO	81.4		
Aluminum Nitrate	Al(NO3)3	212.98		
Gallium Nitrate	Ga(NO3)3	255.72		
Indium Nitrate	In(NO3)3	300.82		
Aluminum Nitrate Nonahydrate	Al(NO3)3 * 9H2O	374.98		
Gallium Nitrate Nonahydrate	Ga(NO3)3 * 8H2O	399.72		
Gallium Oxide	Ga2O3	187.44		
Indium Nitrate Nonahydrate	In(NO3)3 * 3H2O	354.82		
Indium Oxide	In2O3	277.64		
Ammonium Nitrate	NH4(NO3)	80		
Sodium citrate tribasic dihydrate	HOC(COONa)(CH2COONa)2 · 2H2O	294.1		
Ammonium Hydroxide	NH4OH	35		
Aluminum Nitrate Nonahydrate	Al(NO3)3 * 9H2O	162		
Gallium Nitrate Octahydrate	Ga(NO3)3 * 8H2O	399.72		
Indium Nitrate Trihydrate	In(NO3)3 * 3H2O	354.82		
	wt% NH3	wt% NH4OH	M NH3	M NH4OH
29% NH4OH	29	56.6	15.35	14.53

The preparation of seed layer solutions is outlined in Table 3. It includes the volumes needed for the addition of dopants of a given concentration as well. Large quantities of stock solution can be prepared if used in a series of experiments. It may not be a good idea to store for an extended period since dissolved CO_2 in the

water can over time react with the salts in solution. Also listed is the amount of NH_4OH required to set the pH of the solution to 8 after it heats to 80 °C

Table 3 Solution concentrations per molar and mass basis for precursors used in hydrothermal seed layer deposition of ZnO for 25 ml run solutions and 1000 ml stock solutions

Seed Layer Growth Solution

	mol/L			
DI water		mL	25	1000
Zinc Nitrate Hexa-hydrate (Zn(NO3)2:6H2O)	**0.020**	g	0.149	5.948
Ammonium Nitrate (NH4NO3)	**0.350**	g	0.700	28.00
0.1 M Nitrate Dopant	**0.001**	ml	0.25	
0.1 M Nitrate Dopant	**0.002**	ml	0.5	
0.1 M Nitrate Dopant	**0.003**	ml	0.75	
0.1 M Nitrate Dopant	**0.004**	ml	1	
NH4OH after sample @ 90 °C pH ~ 8				
29% Ammonium Hydroxide (NH4OH)	14.53	mL	**0.13**	
0.1 M Nitrate Dopant Solutions	**mol/L**	mL	10	25
Al - Aluminum Nitrate Nonahydrate	**0.1**	g	0.162	0.405
Ga - Gallium Nitrate Octahydrate	**0.1**	g	0.400	0.999
In - Indium Nitrate Trihydrate	**0.1**	g	0.355	0.887

The preparation of second layer solutions is outlined in Table 4. It includes the volumes needed for the addition of dopants of a given concentration as well. Large quantities of stock solution can be prepared if used in a series of experiments. It may not be a good idea to store for an extended period since dissolved CO_2 in the water can over time react with the salts in solution.

Table 4 Solution concentrations per molar and mass basis for precursors used in hydrothermal second layer deposition of ZnO for 25 ml run solutions and 1000 ml stock solutions

Second Layer Growth Solution

DI water	mol/L	mL	25	250
Zinc Nitrate Hexa-hydrate (Zn(NO3)2:6H2O)	0.020	g	0.149	1.487
Trisodium Citrate (Na3C6H5O7)	0.005	g	0.037	0.368
0.1 M Nitrate Dopant	0.001	ml	0.25	
0.1 M Nitrate Dopant	0.002	ml	0.5	
0.1 M Nitrate Dopant	0.003	ml	0.75	
0.1 M Nitrate Dopant	0.004	ml	1	

NH4OH added prior to sample @ room temperature pH ~ 10.5				
29% Ammonium Hydroxide (NH4OH)	14.53	mL	1.3	

0.1 M Nitrate Dopant Solutions	mol/L	mL	10	25
Al - Aluminum Nitrate Nonahydrate	0.1	g	0.162	0.405
Ga - Gallium Nitrate Octahydrate	0.1	g	0.400	0.999
In - Indium Nitrate Trihydrate	0.1	g	0.355	0.887

A.3. Standard LED Process

This section outlines the fabrication process for the primary LED design used in this thesis. Table 5 is a sample process follower used during fabrication. It includes all steps after MOCVD growth of the epitaxial layers required to form an LED. The follower ends with devices on a wafer, which would need to be packaged before complete testing.

APPENDIX B. MOCVD Growth and CTLMs

Table 5 Process follower for the fabrication of 'standard' LEDs

Step	Equipment	Details	Comments
Activation, Quick Test, and Surface Clean			
Activate	MOCVD Lab Oven	600°C, 15min, air	DO NOT ACTIVATE WITH INDIUM ON SAMPLE
Qucik Test (Optional)	LED Test Station		
Indium Dot Removal	Acid Bench	Aqua Regia (HCl:HNO3 3:1), 2-3X, 10 mins, 80C (on thermometer)	set hotplate to ~130C, mix aqua regia (AR), put AR on hotplate and let sit for 5 mins before immersing samples, mix fresh AR after ~10 mins of etching and repeat
Clean	Solvent Bench	Acetone 3min, Isopropanol 3min, DI rinse 3min, N2 Dry	Sonicate
p-Electrode ITO Deposition			
ITO Deposition	E-Beam #2 w/ heater system	Thickness - 1.1 kÅ, 0.5-1.0 Å/s, O2 flow ~30 sccm	include Si reference substrate
		Substrate temperature: 250-350 C (Stage Temperature 650 C)	
		cool-down with ~30 sccm O2 flow	
Measure ITO thickness (optional)	Ellipsometry/dektak	Use Si reference, (dektak on masked area)	Woollam ITO model on Si model
Mesa Formation			
Mesa Photolithography	Spin Coat Bench	PR: **AZnLOF2020** @ 3k rpm for 30" Program 5	or 3k rpm 10k rpm/s 30s
		Soft Bake @ **110 C** for 60"	
	Contact Aligner	Expose for **11"**	**Negative Tone Mask**
	Spin Coat Bench	Hard Bake @ **110 C** for 60"	check that power is around 7.5 W/cm2
	Develop Bench	Develop in AZ300 MIF for 50"	
		Rinse in DI water and N2 Dry	
	Optical Microscope	Check PR mask	
UV Ozone Descum	PR-100	10min	
RIE#2 chamber preparation	RIE#2	O2 clean, 20 sccm, 125 mT, 500V, 30'	No sample in the chamber
		M/H/A coat, 4/20/10 sccm, 75 mT, 500V, 20'	M: Methane, H: Hydrogen, A: Argon
ITO dry etch	RIE#2	MHA dry etch, 4/20/10 sccm, 75 mT, 350V (~18 nm/min)	20% over etch
		O2 descum, 20 sccm, 125 mT, 300V, 5'	
	Optical Microscope	Check ITO Etch	
Measure ITO thickness (optional)	Dektak		
ICP Chamber Preparation	ICP Bench	Clean Si Carrier Wafer with ACE and IPA	
	ICP #1	ML27/CR#144: O2 40sccm, 5Pa, 900/0W, 5min/Cl2 coat 5 min	Use empty Si carrier wafer
Mesa Etch	ICP Bench	Add a crop of vaccuum oil to Si wafer on which to attach sample	
	ICP #1	ML4/#140: Cl2/N2 37.5/12.5sccm, 1.2Pa, 500/200W (~0.6-0.7 um/min)	etch rate depends on samples size larger = less
ICP Chamber Clean	ICP #1	ML3/#105 O2 clean, at least 5' or same as run time	Use Si Cleaning Wafer
	ICP Bench	Clean Si Carrier Wafer with ACE and IPA	
Strip PR	Solvent Bench	**AZ NMP** preheated 80°C, 3 min in heated bath	sonication
Check Etch Depth	Dektak		Drop stylus off of ITO/Mesa
n-Electrode Metal Deposition			
Clean	Solvent Bench	Acetone 3', Isopropanol 3', DI rinse 3'	No sonication
n-Electrode Photolithography	Spin Coat Bench	PR: **AZnLOF2020** @ 3k rpm for 30" Program 5	or 3k rpm 10k rpm/s 30s
		Soft Bake @ **110 C** for 60"	Positive Tone Mask
		Expose for **11"**	
	Contact Aligner	Hard Bake @ **110 C** for 60"	check that power is around 7.5 W/cm2
	Spin Coat Bench	Develop in AZ300 MIF for 60"	
	Develop Bench	Rinse in DI water for 60" and N2 Dry	
	Optical Microscope	Check PR mask	
UV Ozone Descum	PR-100	10'	
HCl Dip	Acid Bench	HCl:DI 1:3, 30sec; DI Rinse	
n-Electrode Metal Deposition	E-Beam #3/4	Ti/Al/Ni/Au, 200/1000/1000/1000Å	
Liftoff	Solvent Bench	**AZ NMP** preheated 80°C, 10-15 min in heated bath	
	Optical Microscope	Check final device	
n-Electrode Anneal (optional)	RTA	450°C, 3', N2, 5sccm	Check RTA Calibration First
p/n-Pad Metal Deposition			
Clean	Solvent Bench	Acetone 3', Isopropanol 3', DI rinse 3'	No sonication
n-Electrode Photolithography	Spin Coat Bench	PR: **AZnLOF2020** @ 3k rpm for 30" Program 5	or 3k rpm 10k rpm/s 30s
		Soft Bake @ **110 C** for 60"	Positive Tone Mask
		Expose for **11"**	
	Contact Aligner	Hard Bake @ **110 C** for 60"	check that power is around 7.5 W/cm2
	Spin Coat Bench	Develop in AZ300 MIF for 60"	
	Develop Bench	Rinse in DI water for 60" and N2 Dry	
	Optical Microscope	Check PR mask	
UV Ozone Descum	PR-100	10'	
HCl Dip	Acid Bench	HCl:DI 1:3, 30sec; DI Rinse	
p/n-Pad Metal Deposition	E-Beam #4	Cr/Ni/Au, 250/200/5000Å	
Liftoff	Solvent Bench	**AZ NMP** preheated 80°C, 10-15 min in heated bath,	
	Optical Microscope	Check final device	

A.4. Flip Chip LED Process

The process follower for flip-chip LEDs on freestanding GaN substrates with n-GaN TJ contacts is shown in Table 6. The process is a bit more involved since it involves the deposition of omnidirectional mirrors and separate mirror and pad metal depositions. A summary of the submount process and part of the packaging of the die is presented in Table 7.

APPENDIX B. MOCVD Growth and CTLMs

Table 6 Process follower for the fabrication of flip-chip LEDs on free-standing GaN substrates

Step	Equipment	Details	Comments
		Dicing Samples	
Dicing	Dicing Saw	epi side down (on tape)	dice samples to needed size
Release sample	UV Lamp	UV release 90s	
Clean	Solvent Bench	Acetone 3', Isopropanol 3' and DI rinse	sonicate ace and iso
		p-Electrode TJ Deposition	
Organics Clean	Acid Bench	1:1:5 HNH4OH:H2O2:H2O 5 mins	heat on hotplate at 120 C add H2O2 after heated
Dicing	Dicing Saw	Dice into needed sizes epi side down	UV release 90s
Solvent Clean	Solvent Bench	Acetone 3', Isopropanol 3' and DI rinse	sonicate ace and iso
Organics Clean	Acid Bench	1:1:5 HNH4OH:H2O2:H2O 10 mins	heat on hotplate at 120 C add H2O2 after heated
		Rinse in DI water and N2 Dry	
Surface Clean	HF Bench	1 min dip 49% HF	
Seal	Vacuum Sealer	Seal 98% Vacuum, 1.0 gas return	Program P4
Tunnel Junction	MBE	Regrow TJ by MBE	
		Activation, Quick Test, and Surface Clean	
Quick Test (Optional)	LED Test Station		
Indium Dot Removal	Acid Bench	Aqua Regia (HCl:HNO3 3:1), 2-3X, 10 mins, ~80C (on thermometer)	set hotplate to ~120C, mix aqua regia (AR) and let sit for 5 mins before immersing samples, mix fresh AR after ~10 mins of etching and repeat
Activate	MOCVD Lab Oven	600°C, 15min, air	DO NOT ACTIVATE WITH INDIUM ON SAMPLE
		Mesa Formation	
Mesa Photolithography	Spin Coat Bench	PR: **SPR220-3.0** @ 4k rpm for 30" (program 7)	or set 10,000 rpm/s ramp
		remove edge bead and clean backside with EBR 100	
		Soft Bake @ **115 C** for 90"	
	Contact Aligner	Expose for 60**"**	7.5 W/cm2 power on hard contact mode
		wait 10'	
		Hard Bake 1 @ **60 C** for 60"	
	Spin Coat Bench	Hard Bake 2 @ **115 C** for 60"	
	Develop Bench	Develop in AZ300 MIF for 60"	
		Rinse in DI water for 60" and N2 Dry	
	Optical Microscope	Check PR mask	develop more if necessary
UV Ozone Descum	PR-100	10min	(~6 ang/min)
Chamber and Wafer Preparation	RIE #5	recipe: Mughal05 - conditioning Cl2 BCl3 SiCl4	use empty carrier wafer
Mesa Etch	RIE #5	recipe: Mughal02 90' Cl2 110nm/min SiCl4 30 nm/min (1 um)	sample on carrier wafer
Post Etch	Beaker	dip samples in DI water after removing from reactor	
Liftoff	Solvent Bench	**AZ NMP** preheated 80°C, 10-15 min in heated bath, sonicate for 2'	Sonicate at low power/frequency < 3 if necessary
Acid Clean	HF bench	BOE 60" dip and DI rinse	
Check Etch Depth	Dektak		Drop stylus off of Mesa in at least two points
		HR Dielectric Deposition	
Clean	Solvent Bench	Acetone 3', Isopropanol 3' and DI rinse	No sonication
Dry	Spin Coat Bench	Dehydration bake 110 C 2' and let cool for 1'	
Dielectric Photolithography	Spin Coat Bench	PR: **AZnLOF2035** @ 3k rpm for 30" (program 5)	Negative Tone
		remove edge bead and clean backside with EBR 100	
		Soft Bake @ **110 C** for 90"	
	Contact Aligner	Expose "Mesa" for **10"**	check that power is around 7.5 W/cm2
	Spin Coat Bench	Hard Bake @ **110 C** for 60"	
	Develop Bench	Develop in AZ300 MIF for 60"	
		Rinse in DI water for 60" and N2 Dry	
	Optical Microscope	Check PR mask	
UV Ozone Descum	PR-100	10' - 20'	
IBD Coating	IBD	Calibrate Ta2O5, SiO2, and Al2O3 depositions	measure with ellipsometry
	Yonkee_7Layer	195.5nm SiO2 40 deg	(same as 304.1 nm normal incidence SiO2)
		121.4nm Ta2O5	
		355.7nm SiO2	
		59nm Ta2O5	
		89.8nm SiO2	
		53.5nm Ta2O5	
		59.5nm Al2O3	
Liftoff	Solvent Bench	**AZ NMP** preheated 80°C, 10-15 min in heated bath, sonicate for 2'	Sonicate at low power/frequency < 3 if necessary
	Optical Microscope	Check device	
		Metal Mirror Deposition	
Clean	Solvent Bench	Acetone 3', Isopropanol 3' and DI rinse	No sonication
Dry	Spin Coat Bench	Dehydration bake 110 C 2' and let cool for 1'	
Dielectric Photolithography	Spin Coat Bench	PR: **AZnLOF2035** @ 3k rpm for 30" (program 5)	Negative Tone
		remove edge bead and clean backside with EBR 100	
		Soft Bake @ **110 C** for 90"	
	Contact Aligner	Expose for "HR Coating" **10"**	check that power is around 7.5 W/cm2
	Spin Coat Bench	Hard Bake @ **110 C** for 60"	
	Develop Bench	Develop in AZ300 MIF for 60"	
		Rinse in DI water for 60" and N2 Dry	
	Optical Microscope	Check PR mask	
UV Ozone Descum	PR-100	10' - 20'	
Metal Mirror Deposition	E-Beam #4	Deposit Al/Ni 900nm/100nm	
Liftoff	Solvent Bench	**AZ NMP** preheated 80°C, 10-15 min in heated bath, sonicate for 2'	Sonicate at low power/frequency < 3 if necessary
	Optical Microscope	Check device	
		Dielectric Deposition	
Clean	Solvent Bench	Acetone 3', Isopropanol 3' and DI rinse	No sonication
Dry	Spin Coat Bench	Dehydration bake 110 C 2' and let cool for 1'	
Dielectric Photolithography	Spin Coat Bench	PR: **AZnLOF2035** @ 3k rpm for 30" (program 5)	Negative Tone
		remove edge bead and clean backside with EBR 100	
		Soft Bake @ **110 C** for 90"	
	Contact Aligner	Expose "Dielectric" for **10"**	check that power is around 7.5 W/cm2
	Spin Coat Bench	Hard Bake @ **110 C** for 60"	
	Develop Bench	Develop in AZ300 MIF for 60"	
		Rinse in DI water for 60" and N2 Dry	
	Optical Microscope	Check PR mask	
UV Ozone Descum	PR-100	10' - 20'	
IBD Coating	IBD	200nm Al2O3 40 deg	thickness does not need to be very accurate
Liftoff	Solvent Bench	**AZ NMP** preheated 80°C, 10-15 min in heated bath, sonicate for 2'	Sonicate at low power/frequency < 3 if necessary
	Optical Microscope	Check device	
		Pad Metal Deposition	
Clean	Solvent Bench	Acetone 3', Isopropanol 3' and DI rinse	No sonication
n/p Electrode Photolithography	Spin Coat Bench	PR: **AZnLOF2035** @ 3k rpm for 30" Program 5	Negative Tone
		Soft Bake @ **110 C** for 90"	
	Contact Aligner	Expose "Mirror" for **10"**	check that power is around 7.5 W/cm2
	Spin Coat Bench	Hard Bake @ **110 C** for 60"	
	Develop Bench	Develop in AZ300 MIF for 60"	
		Rinse in DI water for 60" and N2 Dry	
	Optical Microscope	Check PR mask	
UV Ozone Descum	PR-100	10' - 20'	
p/n-Pad Metal Deposition	E-Beam #3 or 4	Deposit Ni/Au 50nm/500nm	
Liftoff	Solvent Bench	**AZ NMP** preheated 80°C, 10-15 min in heated bath, sonicate for 2'	Sonicate at low power/frequency < 3 if necessary
	Optical Microscope	Check final device	

Table 7 Process follower for the fabrication of flip-chip submounts and packaging of flip-chip LEDs on free-standing GaN substrates

Submount			
Dicing	Dicing Saw	epi side down (on tape)	dice samples to needed size
Release sample	UV Lamp	UV release 90s	
Solvent Clean	Solvent Bench	Acetone 3', Isopropanol 3' and DI rinse	sonicate ace and iso
Organics Clean	Acid Bench	1:1:5 HNH4OH:H2O2:H2O 10 mins	heat on hotplate at 120 C add H2O2 after heated
Blanket Metal Deposition	E-Beam #3 or 4	Deposit Ti/Ni/Al 5nm/5nm/100nm	
IBD Coating	IBD	Calibrate Ta2O5 and SiO2depositions	measure with ellipsometry
	Yonkee_11Layer	64.6nm SiO2	
		54.6nm Ta2O5	
		92.4nm SiO2	
		59.5nm Ta2O5	
		175.5nm SiO2	
		67.3nm Ta2O5	
		116.7nm SiO2	
		97.6nm Ta2O5	
		109.2nm SiO2	
		112.1nm Ta2O5	
Submount Pads Photolithography	Spin Coat Bench	PR: **AZnLOF2035** @ 3k rpm for 30" Program 5	Negative Tone
		Soft Bake @ **110 C** for 90"	
	Contact Aligner	Expose for **10"**	check that power is around 7.5 W/cm2
	Spin Coat Bench	Hard Bake @ **110 C** for 60"	
	Develop Bench	Develop in AZ300 MIF for 60"	
		Rinse in DI water for 60" and N2 Dry	
	Optical Microscope	Check PR mask	
UV Ozone Descum	PR-100	10' - 20'	
Submount Metal Deposition	E-Beam #3 or 4	Deposit Ti/Ni/Au 30nm/50nm/1000nm	
Liftoff	Solvent Bench	**AZ NMP** preheated 80°C, 10-15 min in heated bath, sonicate for 2'	Sonicate at low power/frequency < 3 if necessary
	Optical Microscope	Check final device	
Substrate Thinning/polishing			
Mount	Hot plate	set to 140 °C and place samples device down with x'tal bond	press for 5 min on press stage
Thin/Polish	Lapping station	6 µm diamond plate to thin down to ~200 µm	check with micrometer
		3 µm diamond suspension polish for ~12 µm	
		20 nm silica suspension polish for ~6 µm	
Unmount	Hot plate	set to 140 °C and let mound heat for 10' then slide samples off	
Backside Roughening			
Clean	Solvent bench	Acetone 3', Isopropanol 3' and DI rinse	
PR Mask	Spin Coat Bench	PR: **SPR220-3.0** @ 4k rpm for 30" (program 7)	or set 10,000 rpm/s ramp
		Soft Bake @ **115 C** for 90"	~100 °C on hot plate
Roughen	HF bench	AZ MIF300: DI Water 1:2 dilution	
		heat to 60 °C	~100 °C on hot plate
		place sample in solution for 15 min	
		rinse with DI water	
Clean	Solvent Bench	Acetone 3', Isopropanol 3' and DI rinse	No sonication
Dicing			
Mount	Tape dispenser	set to 50 °C, set tape on platen and flip over, gently press sample onto tape	wait ~10 min
Dicing	Dicing Saw	blade: thermocarbon 2.050-4C-22RU-3	
		flange: 51mm	
		speed: 0.75 mm/s	
		shallow cut (~40 µm from top of sample	
		deep cut (~90 µm from bottom of stage)	
UV Release	UV station	2'	
Bonding			
Placing submount	Westbond pick and place	pick and place submount in proper orientation onto stage	
Placing LEP	Westbond pick and place	use syring needle to pick and place LEP material onto submount	
Placing LED	Westbond pick and place	pick and place LED device side down onto submount	
Bonding	Dexerials Bonder	place samples into bonding stage and press at 200 °C with proper pressure	need to press 3 samples at a time

A.5. LED Packaging

In addition to the fabrication steps done in the cleanroom, several more are required to have an LED ready for testing. This part of the procedure is known as packaging. It involves testing the LEDs on the wafer, singulating the fabricated dies from each other through dicing or scribing, mounting the die on an Ag header, Au wirebonding, encapsulating in silicone or epoxy, and finally testing in an integrating sphere. Outlined in this section are some details for each of those steps.

A.5.1. Quick Testing

"Quick testing" of LEDs is conducted prior to packaging. This step ensures that the processed devices function as intended and is a way to test individual die quickly prior to investing time on subsequent steps. LED die typically do not need a high current 'burn-in,' but depending on the material and fabrication conditions this step can help lower operating voltages. LIV and spectrum data can be collected for die across a wafer to determine yield and performance variations.

A.5.2. Die Singulation

Die singulation can be done one of two ways. They can either be diced or scribed, with both methods having benefits and drawbacks. Dicing is carried out on an ADT 7100 dicing saw. Samples can be thinned prior to dicing to allow blades to wear less quickly. When dicing the key metrics to note are the blade type, blade exposure, cut depth, and cut rate. All these parameters determine the quality and width of the cuts. For our studies, we used Thermocarbon blades which contain embedded diamond particles. Thicker blades with large particle sizes are more robust and can be used longer than thinner blades with smaller particle sizes. The roughness around the cut, known as kerf, can vary depending on particle size and cut speed. Smaller particles and slower cut speeds give smoother cuts. Including a shallow cut, in which the top 20-50 μm of the sample is cut, can also help with reducing roughness.

The alternative is to singulating die is to scribe using a diamond scriber. For some of the work in this dissertation, a Tecdia diamond scriber was used during singulation. Samples must be thinned and polished to around 150 to 200 μm prior to scribing. Scribe depths and load must be determined per sample to ensure that the scriber cleaves samples without cracking.

A.5.3. Mounting and Wirebonding

Singulated LEDs are mounted on silvered headers, and their n/p bonding pads are wire bonded to posts on the headers. LEDs are mounted using a small amount of epoxy or silicone. Ensure that the samples lay flat on the header as it will make wire bonding easier. Wiring bonding is carried out on a stage heated to 80 °C, a ball bond is formed on the pads, and a wedge bond is made on the posts. Sonication power and time can be adjusted if there are difficulties with bonding. After this step, it is a good idea to test the devices by attaching the leads of the header to a power source that can supply 20 mA.

A.5.4. Encapsulation

The last step to packaging is encapsulation. This step involved surrounding the die in either epoxy or silicone to enhance light extraction. The encapsulant is typically shaped into a dome, but for our studies, we used a truncated inverted cone. A negative mold of the shape is used, the silvered header is placed within

the mold, and silicone is poured in. The silicone is set using an oven placed at the appropriate temperature.

A.5.5. Testing

The ultimate step of this whole procedure is to test the packaged LED in an integrating sphere. It may be a good idea to test the LEDs prior to encapsulation in case they do not survive that step. The integrating sphere allows one to measure the spectrum and intensity of the light being emitted. From this efficiency values such as EQE and WPE can be determined. If a phosphor is used to convert to white light, luminous efficacy can be measured as well.

Appendix B. MOCVD Growth and CTLMs

B.1. Blue InGaN LED on Patterned Sapphire Substrate Recipe

Patterned sapphire substrates used in our experiments were sourced from precision Micro-optics 2inch c-plane with a 0.2 ° m-plane miscut and a thickness of 0.43 mm.

																MO Carry		Sub Flow	
Layer	Loop	Time	TC Temp	Gas Carry	NH_3	SiH_4	TMGa	TEGa	TMIn1	TMIn2	TMAl1	TMAl2	Cp_2Mg1	Cp_2Mg1	Gas Carry	H_2	N_2	H_2	N_2
1		60	15	N2	0.5	5	1	30	60	0.02	0.99	1	20	25	1.9	2.5	1.9	5	5
2		8.3	500	H2/N2	0.5	5	3	30	60	0.02	0.99	1	20	25	1.9	1.9	0	5	5
3		3.3	700	H2/N2	0.5	5	3	30	60	0.02	0.99	1	20	25	1.9	1.9	0	5	5
4		3.3	900	H2/N2	0.5	5	3	30	60	0.02	0.99	1	20	25	1.9	1.9	0	5	5
5		3.3	1100	H2/N2	0.5	5	3	30	60	0.02	0.99	1	20	25	1.9	1.9	0	5	5
6		10	1100	H2/N2	0.5	5	3	30	60	0.02	0.99	1	20	25	1.9	1.9	0	10	10
7		3.3	900	H2/N2	0.5	5	3	30	60	0.02	0.99	1	20	25	1.9	1.9	0	10	10
8		3.3	700	H2/N2	3.2	5	3	30	60	0.02	0.99	1	20	25	1.9	1.9	0	10	10
9		100	570	H2/N2	3.2	5	3	45	60	0.02	0.99	1	20	25	1.9	1.9	0	10	10
10		5	570	H2/N2	3.2	9.5	3	45	60	0.02	0.99	1	20	25	1.9	1.9	0	10	30
11		100	570	H2/N2	3.2	9.5	3	45	60	0.02	0.99	1	20	25	1.9	1.9	0	10	30
12		45	700	H2/N2	3.2	9.5	15	45	60	0.02	0.99	1	20	25	1.9	1.9	0	10	30
13		2	900	H2/N2	3.2	9.5	15	45	60	0.02	0.99	1	20	25	1.9	1.9	0	10	30
14		4	1200	H2/N2	3.2	9.5	15	45	60	0.02	0.99	1	20	25	1.9	1.9	0	10	30
15		20	1200	H2/N2	3.2	5	15	45	60	0.02	0.99	1	20	25	1.9	1.9	0	10	30
16		60	1200	H2/N2	3.2	5	15	45	60	0.02	0.99	1	20	25	1.9	1.9	0	10	30
17		5	970	N2	3.2	1.1	3.0▼	50	40	0.04	0.99	1	20	50	1.9	0	1.9	10	30
18		2	970	N2	3.2	1.1	3	35	40	0.04	0.99	1	20	50	1.9	0	1.9	10	30
19		20	970	H2/N2	5	1	3.5	24	4	0.02	0.99	1	20	5.7	1.9	1.9	0	10	30
20		1	970	H2/N2	5	1	3.5	35	60	0.02	0.99	1	20	26	1.9	1.9	0	10	30
21		1	970	H2/N2	6	1	3.5	35	60	0.02	0.99	1	20	26	1.9	1.9	0	10	30
22		1	970	H2/N2	6	1	3.5	35	60	0.02	0.99	1	20	26	1.9	1.9	0	10	30
23		2	860	N2	3.2	1	1	30	90	0.09	1	1	20	50	1.9	0	1.9	15	15
24		26	860	N2	3.2	1	1	30	90	0.09	1	1	20	50	1.9	0	1.9	15	15
25		5	650	N2	5	1	3.5	30	60	0.02	0.99	1	20	25	1.9	0	1.9	0	20
26	END	5	15	N2	1	1	3.5	30	60	0.02	0.99	1	20	25	1.5	0	1	0	5

	temp (C)	**time** (min)	**time** (sec)	**thick** (nm)	**rate** (A/s)	**NH3** (SLM)	**TMGa** (sccm)	**TEGa** (sccm)	**V/III**	**Si** (sccm)	**Mg** (sccm)	**In** (sccm)	**Al** (sccm)
p+ GaN:Mg	1000	1.0	60.0	8.167	1.361	6		35	30,491		26		
p+ GaN:Mg	1000	1.0	60.0	8.167	1.361	6		35	30,491		26		5.7
p- GaN:Mg (In)	970	20.0	1200.0	112.000	0.933	5		24	37,054		5.7	4	
AlGaN:Mg EBL	970	4.6	275.0	25.667	0.933	4		24	29,644		50		1
HT GaN barrier (Δ 50C)	915	2.0	118.0	13.767	1.167	3.2		30	18,972				
LT GaN barrier	865	0.3	20.0	2.333	1.167	3.2		30	18,972				
InGaN well	865	0.4	26.0	3.033	1.167	3.2		30	18,972			90	
LT GaN barrier	865	0.3	20.0	2.333	1.167	3.2		30	18,972				
HT GaN barrier (Δ 50C)	915	2.0	118.0	13.767	1.167	3.2		30	18,972				
n+ GaN	915	1.0	60.0	7.000	1.167	3.2		30	18,972	0.7			
n- InGaN:Si superlattice	930	0.4	24.0	3.267	1.361	3.2		35	16,262	0.7		40	
n- GaN:Si superlattice	930	0.4	24.0	3.267	1.361	3.2		35	16,262	0.7			
n+ GaN:Si template	930	8.0	480.0	107.429	2.238	3.2	3		12,094	1			
n+ GaN:Si template	930	5.0	300.0	67.143	2.238	3.2	3		12,094	1			
n- GaN:Si template	1220	60.0	3600.0	2685.714	7.460	3.2	10		3,628	1			
n- GaN:Si template	1220	20.0	1200.0	1342.857	11.190	3.2	15						
Seed layer	570	1.7	100.0	22.381	2.238	3.2	3						
PSS substrate													

B.2. GaN Substrates Cleaning Procedure

GaN substrates are typically shipped at 2-inch wafers. To maximize the number of growth experiments that can be conducted, samples were diced into 8 mm by 7 mm pieces epi face down on tape. A slightly rectangular shape was chosen to differentiate the crystal orientations such as the m- and a-planes.

Before growth, the samples were thoroughly cleaned to prevent any residual contaminants or particles from disrupting the growth of subsequent epitaxial layers. Substrates were initially solvent cleaned in sonicated acetone and isopropanol for 3 min each then rinsed in DI water and dried under a nitrogen stream. This is done to ensure most of the residuals from the tape used during dicing are removed. A type of "RCA" clean is then performed on the samples. The first is a solution of standard sulfuric acid and hydrogen peroxide (H_2SO_4: H_2O_2 3:1 /vol) set at 80 °C (~130 °C on a hot plate). Samples are submerged in this solution for 30 min. This is followed by a second 30 min submersion in an 80 °C solution of standard ammonium hydroxide, hydrogen peroxide and DI water (NH_3OH: H_2O_2: H_2O_2 1:1:5 /vol). Add the hydrogen peroxide after the solution has come to temperature. The second solution will roughen the N-face of the GaN substrate.

APPENDIX B. MOCVD Growth and CTLMs

B.1. Blue InGaN LED on GaN Substrates Recipe

																MO Carry		Sub Flow	
Layer	Loop	Time	TC Temp	Gas Carry	NH_3	SiH_4	TMGa	TEGa	TMIn1	TMIn2	TMA1	TMAl2	Cp_2Mg1	Cp_1Mg1	Gas Carry	H_2	N_2	H_2	N_2
1		60	15	N2	0.5	5	6	25	200	0.01	0.99	1	10	10	2	2.5	3	5	5
2		8.3	516	N2	4	0.5	6	25	200	0.01	0.99	1	10	10	2	1	3	5	5
3		3.3	716	N2	4	0.5	6	25	200	0.01	0.99	1	10	10	2	1	3	5	5
4		3.3	916	N2	4	0.5	6	25	200	0.01	0.99	1	10	10	2	1	3	10	10
5		2	1150	N2	4	0.5	6	25	200	0.01	0.99	1	10	10	2	1	1.5	10	10
6		5	1150	N2	4	0.5	6	25	200	0.01	0.99	1	10	10	2	1	1.5	15	15
7		3	1150	H2/N2	4	2.0▲	6	25	200	0.2	0.65	1	10	8	1.5	1	1.5	15	15
8		45	1150	H2/N2	4	5	15	50	40	0.04	0.99	1	20	25	1.5	1	1.5	15	15
9		5	930	N2	4	1.5▼	6.0▼	50	40	0.04	0.99	1	20	25	1.5	0	1.5	10	30
10		10	930	N2	4	1.5	6	35	40	0.04	0.99	1	20	25	1.5	0	1.5	10	30
11	LS19	24	930	N2	4	0.6	1	35	40	0.04	0.99	1	20	25	1.5	0	1.5	15	15
12		2	930	N2	4	0.6	1	35	40	0.04	0.99	1	20	25	1.5	0	1.5	15	15
13		24	930	N2	4	0.6	1	35	40	0.04	0.99	1	20	25	1.5	0	1.5	15	15
14	LE	2	930	N2	4	0.3	1	35	40	0.04	0.99	1	20	50	1.5	0	1.5	15	15
15		1	910	N2	4	0.3	1	27	100	0.1	0.99	1	20	50	1.5	0	1.5	15	15
16		20	910	N2	4	0.3	1	27	100	0.1	0.99	1	20	50	1.5	0	1.5	15	15
17	LS7	60	910	N2	4	0.3	1	27	100	0.1	1	1	20	50	1.5	0	1.5	15	15
18		4	860	N2	4	0.3	1	27	100	0.1	1	1	20	25	1.5	0	1.5	15	15
19		40	860	N2	4	0.3	1	27	100	0.1	1	1	20	25	1.5	0	1.5	15	15
20		30	860	N2	4	0.3	1	27	100	0.1	1	1	20	25	1.5	0	1.5	15	15
21		40	860	N2	4	0.3	1	27	100	0.1	1	1	20	25	1.5	0	1.5	15	15
22	LE	1	910	N2	4	0.3	1	27	100	0.1	1	1	20	25	1.5	0	1.5	15	15
23		40	910	N2	4	1	1	27	40	0.04	0.99	1	20	25	1.5	0	1.5	15	15
24		20	950	N2	4	1	3.5	27	40	0.04	0.99	1	20	25	1.5	0	1.5	10	30
25		275	970	N2	4	1	1	24	40	0.04	1	1	20	25	1.5	0	1.5	15	15
26		5	970	H2/N2	5	1	3.5	24	40	0.04	0.99	1	20	6	1.5	1.5	0	10	30
27		20	970	H2/N2	5	1	3.5	24	40	0.04	0.99	1	20	6	1.5	1.5	0	10	30
28		1	970	H2/N2	5	1	3.5	35	60	0.04	0.99	1	20	26	1.5	1.5	0	10	30
29		30	970	H2/N2	6	1	3.5	35	60	0.04	0.99	1	20	26	1.5	1.5	0	10	30
30		30	970	H2/N2	6	1	3.5	35	60	0.04	0.99	1	20	26	1.5	1.5	0	10	30
31		4	830	N2	6	1	3.5	20	60	0.1	0.99	1	20	30	1.5	0	1.5	10	30
32		26	830	N2	4	1	1	20	90	0.1	1	1	20	30	1.5	0	1.5	15	15
33		5	700	N2	6	1	3.5	35	60	0.02	0.99	1	20	26	1.5	0	1.5	10	30
34		5	650	N2	5	1	3.5	30	60	0.02	0.99	1	20	25	1.5	0	1.5	0	20
35	END	5	15	N2	1	1	3.5	30	60	0.02	0.99	1	20	25	1.5	0	1	0	5

	temp (C)	time (min)	thick (nm)	NH3 (SLM)	TMGa (sccm)	TEGa (sccm)	V/III	Si (sccm)	Si/Ga	Mg (sccm)	In (sccm)	Al (sccm)
p+ InGaN:Mg	850	0.43	1.92	4		20	35,572			26		
p+ GaN:Mg	1000	2	10.66	6		24	44,465			26		5.7
p- GaN:Mg (In)	970	18	95.9	5		24	37,054			5.7	4	
AlGaN:Mg EBL	970	4.58	24.42	4		24	29,644			50		1
p GaN:Mg	915	1.47	7.81	4		24	29,644			50		
HT GaN barrier (Δ 50C)	915	1	5.99	4		27	26,350					
LT GaN barrier	865	0.67	4	4		27	26,350	0.25				
InGaN well	865	0.5	3	4		27	26,350				90	
LT GaN barrier	865	0.67	4	4		27	26,350	0.25				
HT GaN barrier (Δ 50C)	915	1	5.99	4		27	26,350	0.25				
n- GaN	915	0.33	2	4		27	26,350	0.25				
n+ GaN	915	1	5.99	4		27	26,350	0.7	0.03			
n- InGaN:Si supperlattice	930	0.4	3.11	4		35	20,327	0.7	0.02		40	
n- GaN:Si superlattice	930	0.4	3.11	4		35	20,327	0.7	0.02			
n+ GaN:Si template	930	10	270	4	6		7,559	1	0.17			
n+ GaN:Si template	930	5	135	4	6		7,559	1	0.17			
n- GaN:Si template	1150	45	3038	4	15		3,023	5	0.33			
AlGaN Buffer	1100	3	81	4	6		7,559					
c-GaN substrate												

B.2. CTLM MATLAB Code

Shown below is the MATLAB code used to determine the sheet resistance, transfer length, and contact resistance of the materials discussed in this work. Text files containing the current-voltage data are imported using this program. From these data sets, resistances are determined and set as a function of gap spacing, to which the full expression for CTLM is fitted, and relevant parameters are found.

```
%%% Asad_Full_CTLM - Script to import and analyze CTLM data

%% Description of Script
% Data must be saved as .txt and have certain qualities:
%
%    - naming: each file must have 'r###g##' in it (i.e.'r100g05').
%
%    - data points: if and dv
%
% Entire sets of data can be selected and analyzed together.  They are
% identified and grouped according to the naming scheme above.
%
% External functions utilized: publish_plot
%
%% Initial clear
clear
%% Setup
t = 10; % thickness of layer measured in nanometers (nm)
ISCALE = 'A'; % set the scale for current; options: {'A'|'mA'|'\muA'}
% File Specifications
nPts = 101; nCol = 4; % # of points/ # of columns. hard coded size of data collection... has to match file
Icol = 2; Vcol = 1; % location of I and V columns. hard coded size of data collection... has to match file
Ilab = ['Current (',ISCALE,')'];
Imult = 1;
if strcmp(ISCALE,'mA'), Imult = 1e3;
elseif strcmp(ISCALE,'\muA'), Imult = 1e6;
end
%% Get files and data
[filename, pathname,~] = uigetfile('\\samba.engr.ucsb.edu\gan_devices\LED_Group\LED
Users\Asad\Characterization\IV\IV Mishra Lab\Raw Data\.txt',... %CHANGED
   'Choose Your CTLM Files','MultiSelect','on');
% cleanup files selected
if ~iscell(filename), filename = {filename}; end
validFileMap = strfind(filename,'r');
validFileMap = ~cellfun(@isempty,validFileMap);
filename(~validFileMap) = [];
validFileMap = strfind(filename,'g');
```

```
validFileMap = ~cellfun(@isempty,validFileMap);
filename(~validFileMap) = [];
assert(~isempty(filename),...
   'Filenames must contain "r###" and "g###" representing the radius and gap width.')
nFiles = length(filename);
% get data
data = zeros([nPts nCol nFiles]);
radii = zeros([nFiles 1]);
gaps = zeros([nFiles 1]);
for i = 1:nFiles
   thisFile = filename{i};
   data(:,:,i) = dlmread(fullfile(pathname,thisFile),'\t',8,0); % Reads Data after row 8
   charPos = strfind(thisFile,'r');
   radii(i) = str2double(thisFile(charPos(end)+1:charPos(end)+3)); %extract inner radius
   charPos = strfind(thisFile,'g');
   gaps(i) = str2double(thisFile(charPos(end)+1:charPos(end)+3)); %extract gap spacings
end
% cleanup
fclose('all');
clear i validFileMap
%% Parse data
I = squeeze(data(:,Icol,:));
V = squeeze(data(:,Vcol,:));
%V = moving_average(V,8,1); %to smooth out data
%% Get slope and offset
p = zeros(size(I,2),2);
for i = 1:size(I,2)
   p(i,:) = polyfit(I(:,i),V(:,i),1);
   %p(i,:) = fit(I(:,i),V(:,i),'poly1', 'Exclude', I>=0); %limit data
   %range does not work
   R(i,1) = p(i,1); %slope = resistance
   Vfit(:,i)= R(i,1)*I(:,i)+p(i,2);
end
figure(1)
plot(I*Imult,V, 'o', I*Imult, Vfit, '-','LineWidth',2)
xlabel(Ilab)
ylabel('Voltage (V)')
legend('Location', 'NorthWest')
legend('off')
grid on
%% Fit: Full CTLM Equation
g = gaps; %gap spacing
r0 = radii; %inner radius
r1 = r0 + g; %outer radius
[xData, yData] = prepareCurveData( g, R );
figure(2)
plot(g,R,'o')
% Set up fittype and options. ((((NEED TO SET R0)))
%ft = fittype(
'(Rsh./(2*pi))*(log((50+g)./50)+(Lt./50)*(besseli(0,50./Lt)./besseli(1,50./Lt))+(Lt./(50+g))*(besselk(0,(50+g
)./Lt)./besselk(1,(50+g)./Lt))', 'independent', 'g', 'dependent', 'Rt' );
%ft = fittype( '(Rsh./(2*pi)).*(g+2*Lt).*(50./g)*log(1+g./50)', 'independent', 'g', 'dependent', 'Rt' );
```

```
%ft = fittype( '(Rsh./(2*pi)).*((Lt./50)+(Lt./(50+g))+log(1+g./50))', 'independent', 'g', 'dependent', 'Rt' );
ft = fittype( '(Rsh./(2*pi)).*(log((50+g)./50)+Lt.^2*(1/50+1./(50+g)))', 'independent', 'g', 'dependent', 'Rt' );
%Ben's thesis
opts = fitoptions( 'Method', 'NonlinearLeastSquares' );
opts.Display = 'Off';
opts.Lower = [0.155 0];
opts.Robust = 'Bisquare';
opts.StartPoint = [0.485375648722841 0.546881519204984];
% Fit model to data.
[fitresult, gof] = fit( xData, yData, ft, opts );
%% Plot fit with data
figure( 'Name', 'CTLM FIT' );
h = plot( fitresult, xData, yData,'bl o');
xlim([4 56])
set(gca, 'LineWidth',2);
legend( h, 'Measured Resistance vs. Gap Spacing', 'Full CTLM Equation', 'Location', 'SouthEast' );
% Label axes
xlabel('Gap Spacing (\mum)','LineWidth',2,'FontSize',18);
ylabel('R (\Omega)','LineWidth',2,'FontSize',18);
grid on
%% Calculations and Final Summary
coeffval = coeffvalues(fitresult); % extract coefficients Lt and Rsh from fitted curves
Lt = coeffval(1); % Transfer Length [um]
Rsh = coeffval(2); % Sheet Resistance [Ohm]
ci = confint (fitresult); % extract confidence interval 95% of results
Ltci = Lt - ci(1); % 95% confidence interval for Lt
Rshci = Rsh - ci(3); % 95% confidence interval for Lt
rho = Rsh*t*1e-7; % Resistivity [Ohm cm]
rho_c = Rsh*Lt^2*1e-8; % Specific contact resistivity [Ohm cm^2]
fprintf(1, ' Thickness = %g nm\n Transfer length = %g +/- %g um\n Sheet Resistance = %g +/- %g
Ohm/Sq\n Resistivity = %g Ohm cm\n Specific Contact Resistivity = %g
Ohm*cm^2\n',t,Lt,Ltci,Rsh,Rshci,rho,rho_c)
```